

Physics of the cosmic microwave background anisotropy*

Martin Bucher

Laboratoire APC, Université Paris 7/CNRS

Bâtiment Condorcet, Case 7020

75205 Paris Cedex 13, France

bucher@apc.univ-paris7.fr and

Astrophysics and Cosmology Research Unit

School of Mathematics, Statistics and Computer Science

University of KwaZulu-Natal

Durban 4041, South Africa

March 1, 2024

Abstract

Observations of the cosmic microwave background (CMB), especially of its frequency spectrum and its anisotropies, both in temperature and in polarization, have played a key role in the development of modern cosmology and our understanding of the very early universe. We review the underlying physics of the CMB and how the primordial temperature and polarization anisotropies were imprinted. Possibilities for distinguishing competing cosmological models are emphasized. The current status of CMB experiments and experimental techniques with an emphasis toward future observations, particularly in polarization, is reviewed. The physics of foreground emissions, especially of polarized dust, is discussed in detail, since this area is likely to become crucial for measurements of the B modes of the CMB polarization at ever greater sensitivity.

¹This article is to be published also in the book “One Hundred Years of General Relativity: From Genesis and Empirical Foundations to Gravitational Waves, Cosmology and Quantum Gravity,” edited by Wei-Tou Ni (World Scientific, Singapore, 2015) as well as in Int. J. Mod. Phys. D (in press).

Contents

1	Observing the microwave sky: a short history and observational overview	1
2	Brief thermal history of the universe	13
3	Cosmological perturbation theory: describing a nearly perfect universe using general relativity	17
4	Characterizing the primordial power spectrum	19
5	Recombination, the blackbody spectrum, and spectral distortions	20
6	Sachs-Wolfe formula and more exact anisotropy calculations	21
7	What can we learn from the CMB temperature and polarization anisotropies?	25
7.1	Character of primordial perturbations: adiabatic growing mode versus field ordering	25
7.2	Boltzmann hierarchy evolution	27
7.3	Angular diameter distance	31
7.4	Integrated Sachs-Wolfe effect	33
7.5	Reionization	34
7.6	What we have not mentioned	38
8	Gravitational lensing of the CMB	38
9	CMB statistics	40
9.1	Gaussianity, non-Gaussianity, and all that	40
9.2	Non-Gaussian alternatives	45
10	Bispectral non-Gaussianity	46
11	B modes: a new probe of inflation	47
11.1	Suborbital searches for primordial B modes	48
11.2	Space based searches for primordial B modes	49
12	CMB anomalies	49
13	Sunyaev-Zeldovich effects	51
14	Experimental aspects of CMB observations	52
14.1	Intrinsic photon counting noise: ideal detector behavior	54
14.2	CMB detector technology	56
14.3	Special techniques for polarization	58
15	CMB statistics revisited: dealing with realistic observations	61
16	Galactic synchrotron emission	63

17 Free-free emission	64
18 Thermal dust emission	65
19 Dust polarization and grain alignment	66
19.1 Why do dust grains spin?	68
19.2 About which axis do dust grains spin?	68
19.3 A stochastic differential equation for $\mathbf{L}(t)$	69
19.4 Suprathermal rotation	69
19.5 Dust grain dynamics and the galactic magnetic field	70
19.5.1 Origin of a magnetic moment along \mathbf{L}	71
19.6 Magnetic precession	72
19.6.1 Barnett dissipation	72
19.7 Davis-Greenstein magnetic dissipation	74
19.8 Alignment along \mathbf{B} without Davis-Greenstein dissipation	75
19.9 Radiative torques	76
19.10 Small dust grains and anomalous microwave emission (AME)	79
20 Compact sources	80
20.1 Radio galaxies	81
20.2 Infrared galaxies	81
21 Other effects	81
21.1 Patchy reionization	81
21.2 Molecular lines	82
21.3 Zodiacal emission	82
22 Extracting the primordial CMB anisotropies	82
23 Concluding remarks	83
References	86

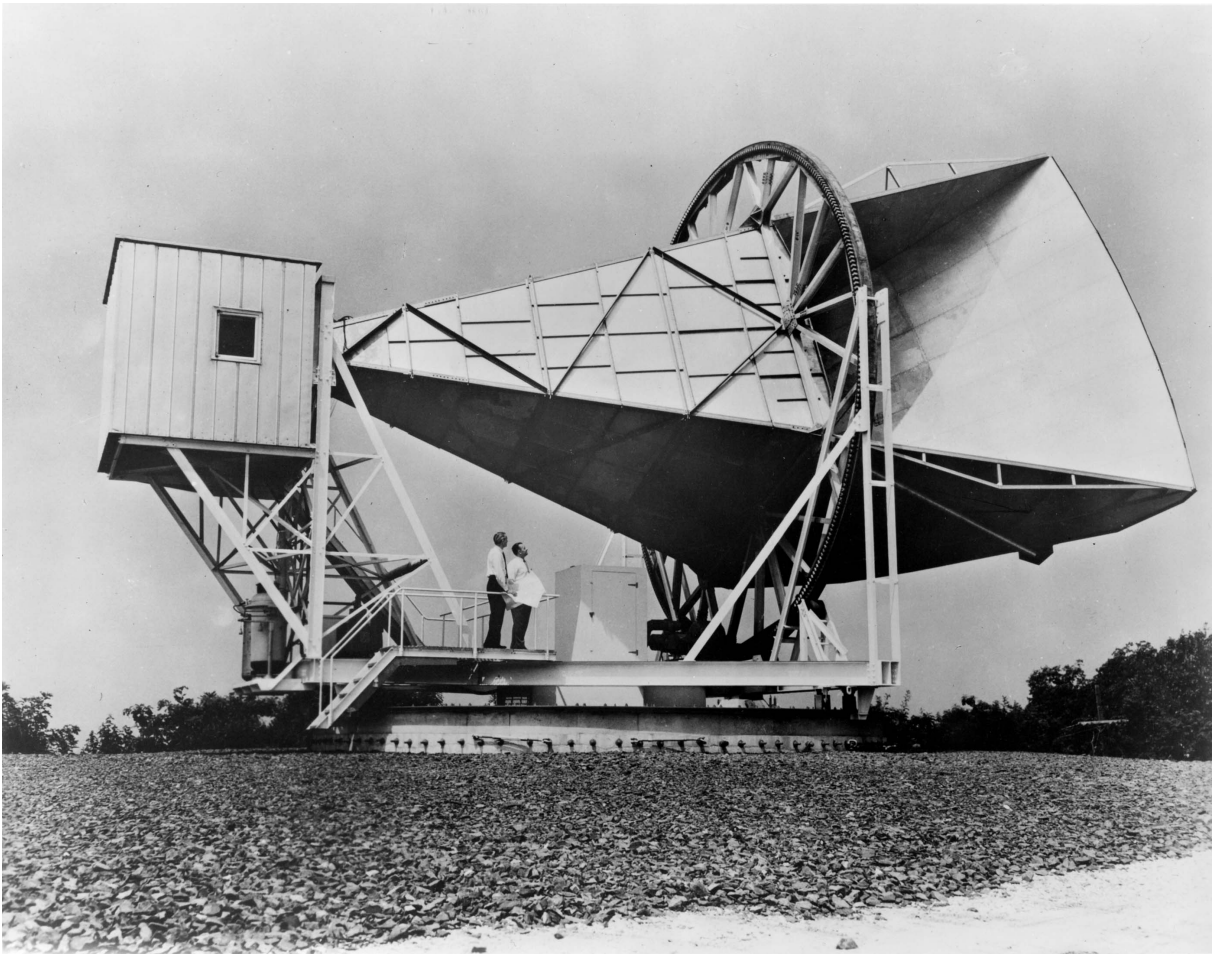


Figure 1: **Horn antenna used in 1964 by Penzias and Wilson to discover the CMB.**
(*Credit: NASA image*)

1 Observing the Microwave Sky: A Short History and Observational Overview

In their 1965 landmark paper A. Penzias and R. Wilson [157], who were investigating the origin of radio interference at what at the time were considered high frequencies, reported a 3.5 K signal from the sky at 4 GHz that was “isotropic, unpolarized, and free from seasonal variations” within the limits of their observations. Their apparatus was a 20 foot horn directed at the zenith coupled to a maser amplifier and a radiometer (see Fig. 1). The maser amplifier and radiometer were switched between the sky and a liquid helium cooled reference source used for comparison. Alternative explanations such as ground pick-up from the sidelobes of their antenna were ruled out in their analysis, and they noted that known radio sources would contribute negligibly at this frequency because their apparent temperature falls rapidly with frequency.

In a companion paper published in the same issue of the *Astrophysical Journal*, Dicke *et al.* [46] proposed the explanation that the isotropic sky signal seen by Penzias and Wilson was in fact emanating from a hot big bang, as had been suggested in the 1948 paper of Alpher

et al. [7] suggesting the presence of the photon blackbody component having a temperature of approximately a few K. Their prediction was based on considering the conditions required for successful nucleosynthesis in an expanding universe—that is, to create an appreciable fraction of primordial helium from the neutrons that are decaying as the universe is expanding.

The importance of this discovery became almost immediately apparent, and others set out to better characterize this excess emission, which later would become known as the Cosmic Microwave Background (CMB), or sometimes in the older literature the Cosmic Microwave Background Radiation (CMBR). The two principal questions were: (i) To what extent is this background isotropic? (ii) How close is the spectrum to a perfect Planckian blackbody spectrum?

The main obstacle to answering these questions was the lack of adequate instrumentation, and this was the main reason why the first detection of the CMB anisotropy had to wait until 1992, when the COBE team announced their observation of a statistically significant anisotropy of primordial origin after the dipole due to our motion with respect to the CMB had been subtracted [211] (see Figs. 2 and 3). The COBE satellite, in a low-Earth orbit, carried three instruments: the differential microwave radiometer (DMR) [210], the far infrared absolute spectrophotometer (FIRAS) [136], and the diffuse infrared background experiment (DIRBE). By today’s standards, the measurement of the cosmic microwave background anisotropy was crude. The angular resolution was low—the width of the beam was 7° (FWHM), and the sky map used for the analysis was smoothed to 10° to suppress beam artefacts. The contribution from instrument noise was large by contemporary standards. The COBE noise was 43, 16, and 22 mK Hz $^{-1/2}$ for the 31, 53, and 90 GHz channels, respectively [21].^a Nevertheless, COBE did provide a convincing first detection of the CMB anisotropy, and most importantly established the overall level of the primordial cosmological density perturbations, which played a crucial role in determining the viability of the cosmological models in vogue at that time, which were much more numerous and varied than today.

The COBE detection was followed by an intense effort to characterize the CMB anisotropy at greater sensitivity and on smaller angular scales. There were numerous experiments from the ground at locations where the column density of water in the atmosphere is particularly low, such as Saskatoon, the Atacama Desert in Chile, the South Pole, and the Canary Islands, as well as from stratospheric balloons. Figure 4 shows the state of play about four years after COBE, with two competing theoretical models plotted together with the data points available at that time. In Sec. 6 we shall present the physics of the CMB systematically, but jumping ahead a bit, we give here a few words of explanation for understanding this plot. In most theoretical models, the CMB is generated by an isotropic Gaussian stochastic process, in which case all the available information concerning the underlying theoretical model can be extracted by measuring the angular power spectrum of the CMB anisotropies. Because of isotropy, one may expand the map in spherical harmonics to extract its angular power spectrum, defined as

$$C_\ell^{TT,\text{obs}} = \frac{1}{(2\ell + 1)} \sum_{m=-\ell}^{+\ell} |a_{\ell m}^T|^2. \quad (1)$$

It is customary to plot the quantity $\ell(\ell + 1)C_\ell/(2\pi)$, which would be constant for a scale

^aBy comparison, for WMAP the detector sensitivities were 0.7, 0.7, 0.9, 1.1, and 1.5 mK · Hz $^{-1/2}$ for the K, Ka, Q, V, and W bands, respectively [96].

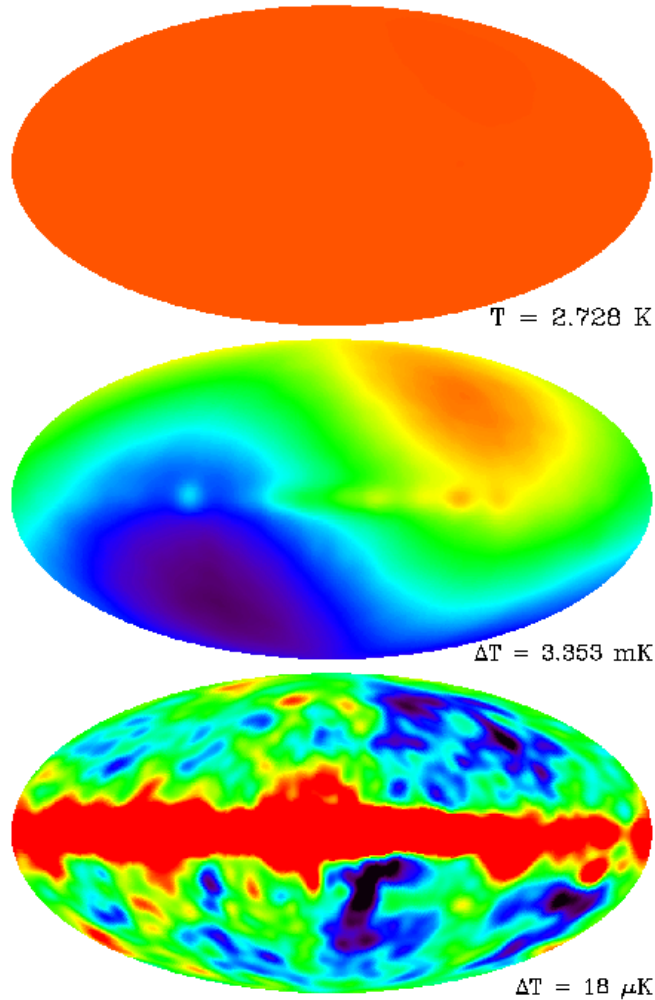


Figure 2: **The microwave sky as seen by the COBE DMR (differential microwave radiometer) instrument.** The top panel shows the microwave sky as seen on a linear temperature scale including zero. No anisotropies are visible in this image, because the CMB monopole at 2.725 K dominates. In the middle panel, the monopole component has been subtracted. Apart from some slight contamination from the galaxy near the equator (corresponding to the plane of our Galaxy), one sees only a nearly perfect dipole pattern, owing to our peculiar motion with respect to the rest frame defined by the CMB. In the bottom panel, both the monopole and dipole components have been removed. Except for the galactic contamination around the equator, one sees the cosmic microwave background anisotropy along with some noise. (*Credit: NASA/COBE Science Team*)

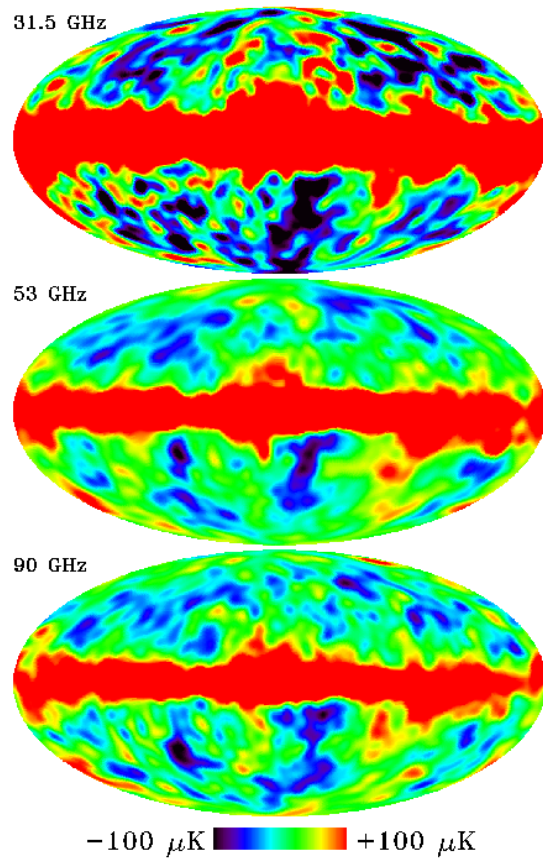


Figure 3: **COBE DMR individual frequency maps (with monopole and dipole components removed)**. Taking data at several frequencies is key to proving the primordial origin of the signal and removing galactic contaminants. Here are the three frequency maps from the COBE DMR observations. (*Credit: NASA/COBE Science Team*)

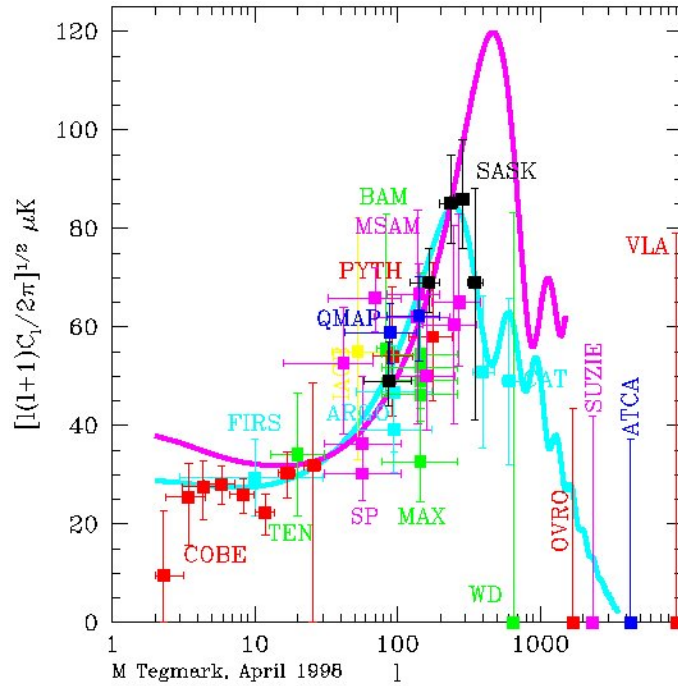


Figure 4: **State of CMB observations in 1998.** After the COBE DMR detection at very large angular scales at the so-called Sachs-Wolfe plateau, numerous groups sought to discover the acoustic peaks, or to find their absence. This compilation from 1998 shows the state of play at that time. While an unmistakable rise toward the first acoustic peak is apparent, it is not so apparent what happens toward higher ℓ . Two theories broadly compatible with the data at that time are plotted, one with $\Omega_k = 0$ and another with $\Omega_k \approx 0.7$, which predicts a higher amplitude of the primordial perturbations and an acoustic peak shifted to smaller angular scales, as explained in Sec. 7.3. (*Credit: Max Tegmark*)

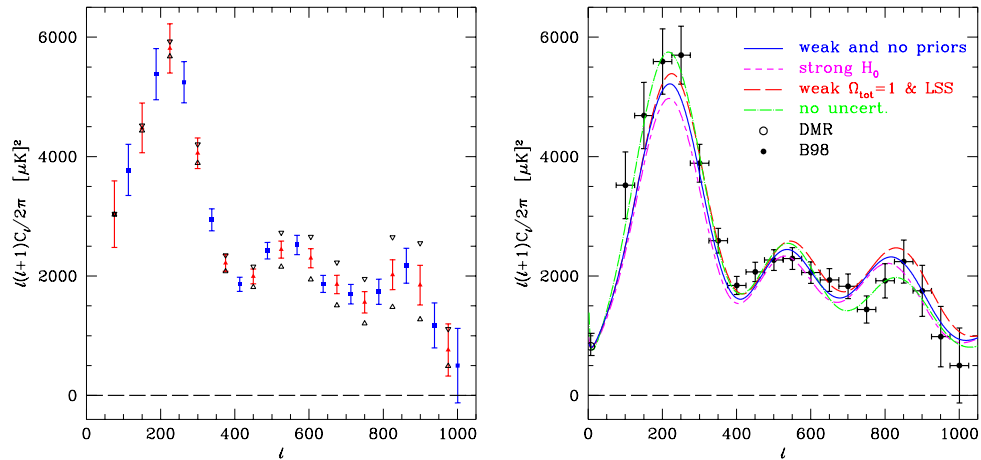


Figure 5: **Boomerang observation of acoustic oscillations.** The C_ℓ^{TT} power spectrum as measured by Boomerang is shown on the left without a fit to a theoretical model and on the right with the theoretical predictions for a spatially flat cosmological model with an exactly scale invariant primordial power spectrum for the adiabatic growing mode. (*Credit: Boomerang Collaboration*)

invariant pattern on the sky.^b This is the quantity plotted in Fig. 4, where the question posed at the time was whether there is a rise to a first acoustic peak followed by several decaying secondary acoustic peaks, as indicated by the solid theoretical curves. This structure is a prediction of simple inflationary models—or more precisely, of models where only the adiabatic growing mode is excited with an approximately scale invariant primordial spectrum. In this plot, one sees fairly convincing evidence for a rise in the angular power, but the continuation of the curve is unclear.

Several experiments contributed to providing the first clear detection of the acoustic oscillations, namely TOCO [138], MAXIMA[79], and Boomerang [143, 15]. Figure 5 shows the power spectrum as measured by one of these experiments, namely Boomerang, where a series of well defined acoustic oscillations is clearly visible.

In the meantime, parallel efforts were underway in Europe and in the United States to prepare for another CMB space mission to follow on COBE at higher sensitivity and angular resolution. The COBE beam, which was 7° FWHM, did not use a telescope but rather microwave feed horns pointed directly at the sky. While not allowing for a high angular resolution, the feed horns had the advantage of producing well defined beams with rapidly falling sidelobes. The US NASA WMAP satellite, launched in 2001, delivered its one-year data release in 2003 (including TT and TE) [235]–[243], and its first polarization data (including also EE) in 2006 [244]–[247] (see Figs. 6 and 7). WMAP continued taking data for nine years, and released installments of papers based on the five-, seven-, and nine-year data releases, in which the results were further refined benefitting from longer integration time (which nominally would shrink error bars in proportion to $1/\sqrt{t_{\text{obs}}}$) as well as improved instrument modeling

^bStrictly speaking, scale invariance on the sky can be defined only asymptotically in the $\ell \rightarrow \infty$ limit, because the curvature of the celestial sphere breaks scale invariance. The use of $\ell(\ell + 1)$ rather than ℓ^2 here is an historical convention.

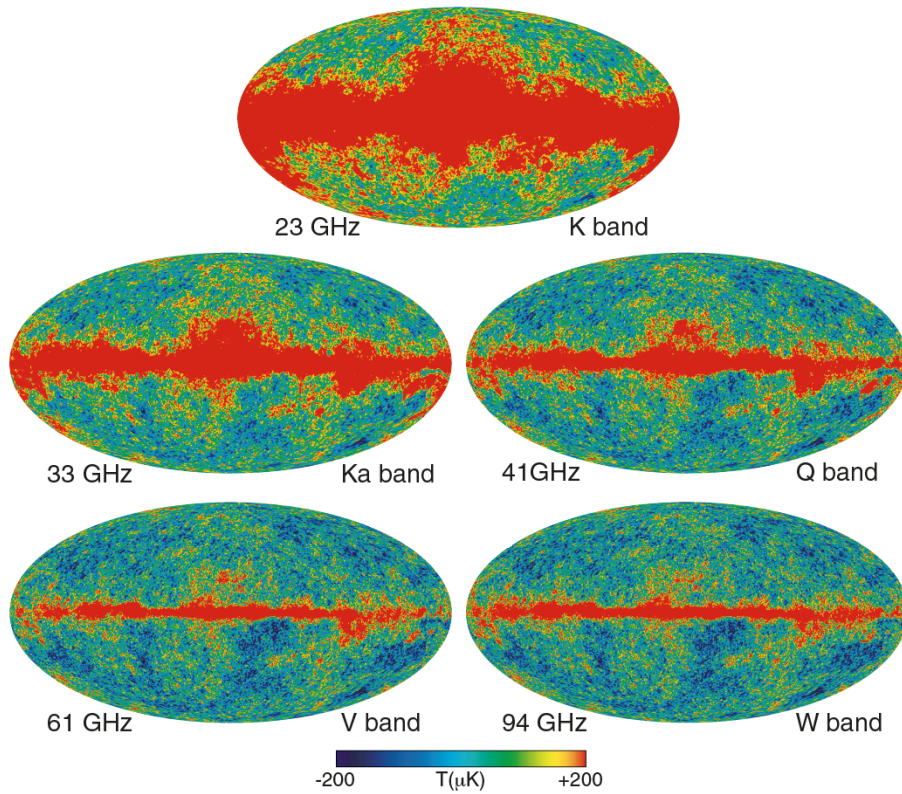


Figure 6: **WMAP single temperature frequency maps.** WMAP observed in five frequency bands. (*Credit: NASA/WMAP Science Team*)

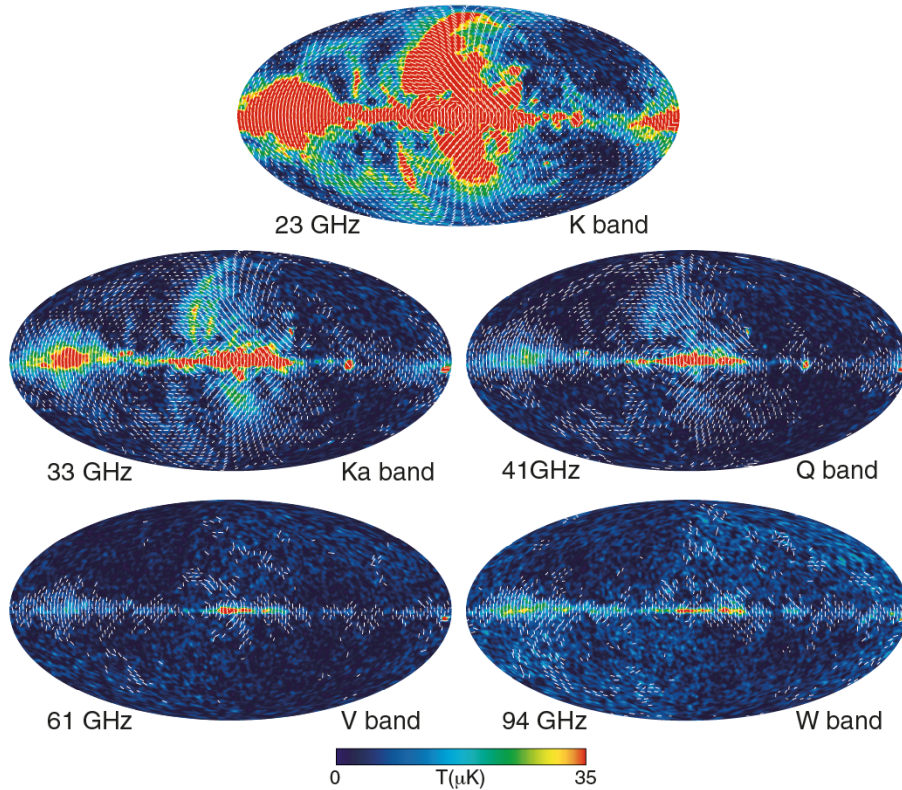


Figure 7: **WMAP single frequency polarization maps.** The lines (which may be thought of as double-headed vectors) show the amplitude and orientation of the linear polarization of the measured CMB anisotropy in the indicated bands. The amplitude $P = \sqrt{Q^2 + U^2}$ is also shown using the indicated color scale. (*Credit: NASA/WMAP Science Team*)

[249]–[260]. WMAP used horns pointed at a $1.4 \text{ m} \times 1.6 \text{ m}$ off-axis Gregorian mirror to obtain diffraction limited beams (although the mirror was under-illuminated somewhat to reduce far sidelobes). The 20 detectors were based on coherent amplification using HEMTs (high electron mobility transistors)—the state of the art in coherent low-noise amplification at the time. The coherent detection technology used by WMAP had the advantage that the electronics could be passively cooled. The competing incoherent bolometric detection technology permits superior sensitivity, which operates almost at the quantum noise limit of the incident photons, but requires cooling to approximately 100 mK. The cryogenic system required was judged to present substantial risk for a space mission at the time, and this was likely one of the reasons why WMAP was selected over one of its competitor missions, which was similar to the European Planck HFI proposal.

The successor to WMAP was the European Space Agency (ESA) Planck satellite, which was launched in May 2009 [159]–[185]. Planck consisted of two instruments: (i) a low-frequency instrument with three channels (at 30, 44 and 70 GHz) using a coherent detection technology, and (ii) a high-frequency instrument using cryogenically-cooled bolometric detectors observing in six bands (100, 143, 217, 353, 545 and 857 GHz). All bands except the highest two bands were polarization sensitive and had a diffraction limited angular resolution, starting at 33 arcmin for the 30 GHz channel and going down to 5.5 arcmin for the 217 GHz channel. (The top three channels have an angular resolution of approximately 5’.) Planck HFI took data from August 2009 to January 2012, when the coolant for its high-frequency instrument ran out. The Planck Collaboration reported its first results for cosmology in March 2013 based on its temperature anisotropy data. The first results for cosmology using the polarization data collected by Planck are expected in late 2014.

Figure 8 shows the Planck full-sky maps of the intensity of the microwave emission in nine frequency bands ranging from 30 GHz to 857 GHz. Figure 9 shows a cleaned full-sky map where a linear combination of the single band maps has been taken in order to isolate the primordial cosmic microwave background signal. While the fluctuations in the cleaned map in Fig. 9 do not appear to single out any particular direction in the sky and appear consistent with an isotropic Gaussian random process, the maps in Fig. 8 show a clear excess in the galactic plane. These full-sky maps use a Mollweide projection in galactic coordinates, with the galactic center at the center of the projection. Even though the galactic contamination depends largely on the angle to the galactic plane, with a lesser tendency to increase toward the galactic center, considerable structure can be seen in the galactic emission over a broad range of angular scales. The central bands include the least amount of galactic contamination, which visibly is much larger for the lowest and the highest frequencies shown.

The CMB dipole amplitude is $\Delta T = 3.365 \pm 0.027$ mK and directed toward $(l, b) = (264.4^\circ \pm 0.3^\circ, 48.4 \pm 0.5^\circ)$ in galactic coordinates [104]. The maps have been processed to remove the 2.725 K CMB monopole component as well as the smaller CMB dipole having a peak-to-peak amplitude of approximately 6.73 mK, so that only the spherical harmonic multipoles with $\ell \geq 2$ are included. CMB angular power is typically expressed in terms of $\mathcal{D}_\ell = \ell(\ell + 1)C_\ell/2\pi$, which in the flat sky approximation corresponds to rms power (in μK^2) per unit logarithmic interval in the spatial frequency. A scale invariant temperature spectrum on the celestial sphere would correspond to $\ell^2 C_\ell$ being constant. For comparison we give here a few ballpark numbers characterizing the strength of the primordial CMB temperature anisotropy. Figure 10 plots the CMB power spectrum as observed by Planck together with the predictions of the fit to a six-parameter theoretical model, which we will discuss further below. The magnitude at low ℓ , before the rise to the first acoustic, or Doppler, peak at $\ell \approx 220$, is $\mathcal{D}_\ell \approx 10^3 \mu K^2$, which would correspond to an rms temperature in the neighborhood of $30 \mu K$. The rise to the first acoustic peak increases the power by about a factor of six, and then after approximately five oscillations, damping effects take over, making the oscillations less apparent and causing the spectrum to suffer a quasi-exponential decay.

Although the detectors (to the extent that their response is ideal or linear) measure the intensity expressed as the “spectral radiance” or “specific intensity” I_ν (having units of $\text{erg s}^{-1} \text{cm}^{-2} \text{Hz}^{-1} \text{str}^{-1}$) averaged over a frequency band defined by the detector, it is convenient to re-express these intensities in terms of an effective temperature. There are two types of effective temperature: the Rayleigh-Jeans (R-J) temperature and the thermodynamic temperature. It is important to keep in mind the distinction, especially at high frequencies [in

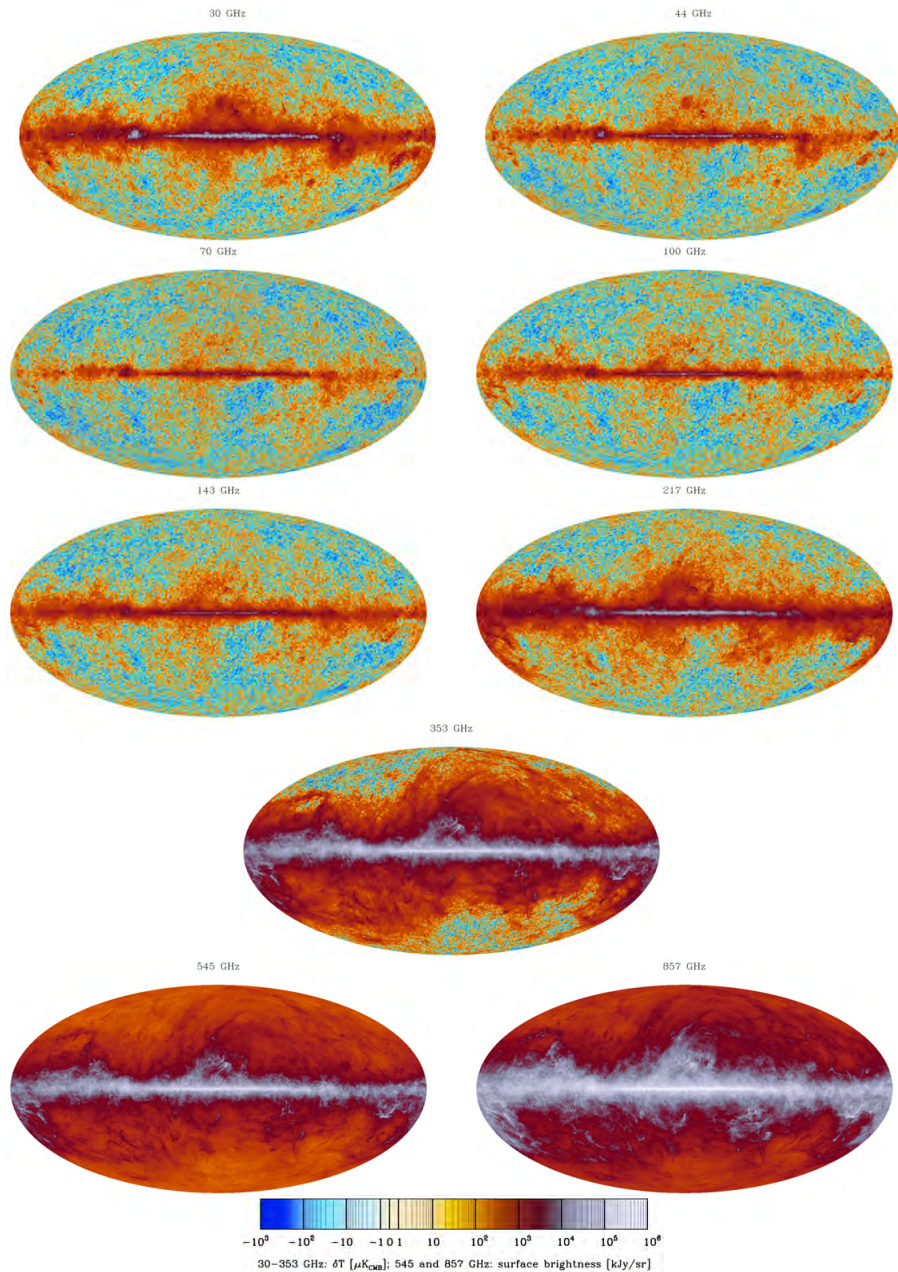


Figure 8: **Planck single frequency temperature maps.** The ESA Planck satellite surveyed the sky in nine broad [i.e. $(\Delta\nu)/\nu \approx 0.3$] frequency bands, centered at 30, 44, 70, 100, 143, 217, 353, 545, and 857 GHz, shown in galactic coordinates. The units are CMB thermodynamic temperature [see Eq. (3)]. The nonlinear scale avoids saturation in regions of high galactic emission. (*Credit: ESA/Planck Collaboration*)

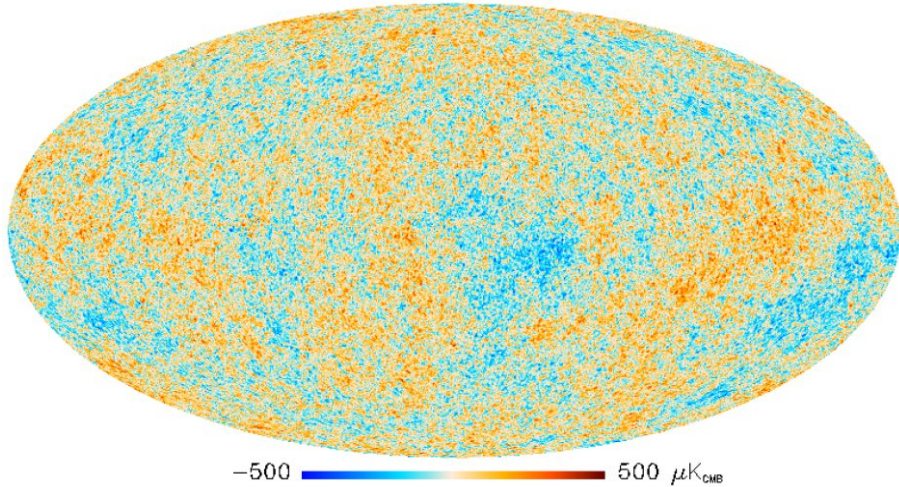


Figure 9: **Planck internal linear combination map.** A linear combination of the Planck single frequency maps (shown in Fig. 8) is taken. This linear combination is optimized to filter out any unwanted contaminants based on their differing frequency dependence. The success of this procedure to remove the galactic contaminants is evident from the disappearance of excess power along the equator corresponding to the galactic plane. (For more details, see Ref. 161.) (*Credit: ESA/Planck Collaboration*)

this context $\nu \gtrsim \nu_{\text{CMB}} = h^{-1}(k_{\text{B}}T_{\text{CMB}}) = 57 \text{ GHz}$] where the factor relating the two becomes large.

In the R-J limit, where $(h\nu/k_{\text{B}}T) \ll 1$, the blackbody spectral radiance may be approximated as $I_{\nu} = B_{\nu}(T) \approx 2(\nu/c)^2(k_{\text{B}}T)$, as one would obtain classically from the density of states of the radiation field and assigning an energy $(k_{\text{B}}T)$ to each harmonic oscillator degree of freedom. If we invert, assuming the R-J limit above (regardless of whether this limit is valid), we obtain the following definition for the R-J temperature

$$T_{R-J}(\nu) = \frac{1}{2} \frac{1}{k_{\text{B}}} \left(\frac{c}{\nu} \right)^2 I_{\nu}. \quad (2)$$

The “thermodynamic” temperature corresponding to a specific intensity I_{ν} at a certain frequency, on the other hand, is obtained by inverting the unapproximated blackbody expression $I_{\nu} = B_{\nu}(T) = (2h\nu^3/c^2)[\exp(h\nu/k_{\text{B}}T) - 1]^{-1}$. For the CMB, where the variations about the average CMB temperature are small (i.e., $\Delta T/T \approx 10^{-5}$), linearized perturbation theory is valid and one can invert this equation, obtaining

$$\delta T_{\text{CMB}} = \frac{(e^x - 1)^2}{x^2 e^x} \delta T_{R-J}, \quad (3)$$

where $x = h\nu/k_{\text{B}}T$. This factor is approximately one for $x \lesssim 1$, but rises exponentially for $x \gtrsim 1$.

It should be remembered that for adding optically thin emissions, it is the intensities, and not the thermodynamic temperatures, that add. Moreover, foreground emission power laws know nothing about T_{CMB} and thus are naturally expressed using either the specific intensity, or equivalently the R-J temperature.

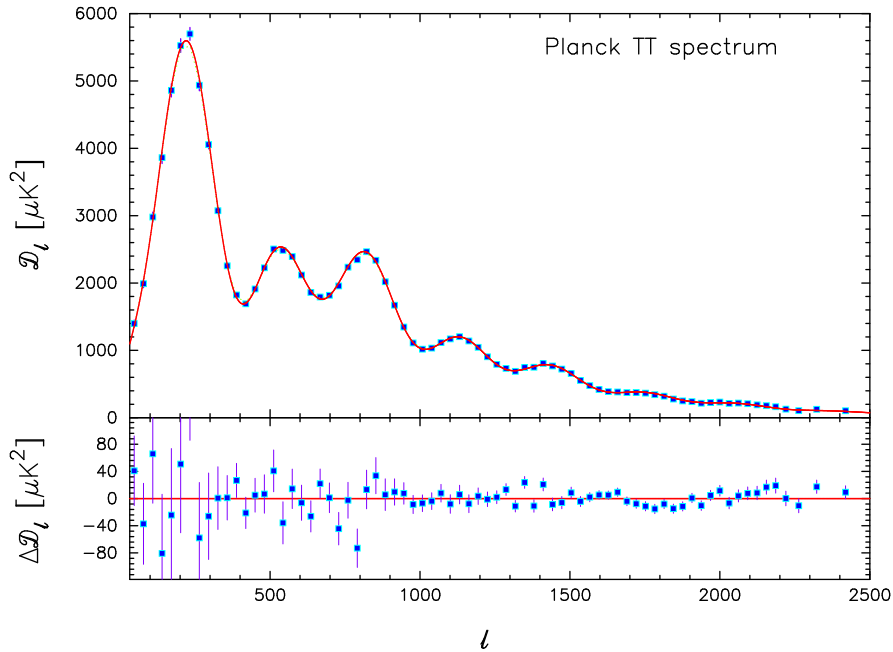


Figure 10: **CMB angular power spectrum as measured by Planck.** The binned C_ℓ^{TT} power spectrum as given in the Planck 2013 release is plotted with error bars that combine uncertainties from cosmic variance (dominant at low ℓ) and instrumental noise (dominant at high ℓ). The solid curve indicates the theoretical predictions of the six-parameter concordance model with the 1σ cosmic variance for the adopted binning scheme. The lower panel shows the residuals. For more details, see Ref. [170]. The exquisite fit, seen here up to about $\ell \approx 2200$, into the damping tail, has been shown to extend to smaller angular scales by ACT [58] and SPT [102]. (*Credit: ESA/Planck Collaboration*)

Other important milestones of CMB observation include the DASI discovery of the polarization of the CMB in 2002 [110] and the observations at small angular scales carried out by the ACT and SPT teams, which at the time of writing constitute the best measurements of the microwave anisotropies on large patches of the sky at high angular resolution, measuring the power spectrum up to $\ell \approx 10,000$. The DASI experiment was carried out using several feed horns pointed directly at the sky. Correlations were taken of the signals from pairs of horns, thus measuring the sky signal interferometrically. The 6 m diameter Atacama Cosmology Telescope (ACT) situated in the Atacama desert in Chile [109, 58] and the 10 m SPT (South Pole Telescope) located at the Amundsen-Scott South Pole Station in Antarctica [102, 199, 194] probe the microwave sky on very small angular scales, beyond the angular resolution of Planck. CMB observations are almost always diffraction limited, so that the angular resolution is inversely proportional to the telescope diameter. Ground based instruments, despite all their handicaps (i.e., atmospheric interference, lack of stability over long timescales, ground pickup from far sidelobes) will always outperform space based experiments in angular resolution. There are dozens of other suborbital experiments not mentioned here but which paved the road for contemporary CMB observation. These experiments were important not only because of their observations, but also because of their role in technology development and in the development of new data analysis techniques. More information on these experiments can be found in other earlier reviews.^c

2 Brief Thermal History of the Universe

The big bang model of the universe is an unfinished story. Certain aspects of the big bang model are well established observationally, while other aspects are more provisional and represent our present best bet speculation. In the account below, we endeavor to distinguish what is relatively certain and what is more speculative.

If we assume: (i) the correctness of general relativity, (ii) that the universe is homogeneous and isotropic on large scales (at least up to the size of that part of the universe presently observable to us), and (iii) that for calculating the behavior of the universe, small-scale anisotropies can be averaged over, we obtain the Friedmann-Lemaître-Robertson Walker (FLRW) solutions to the Einstein field equations, which we now describe. The metric for this family of solutions takes the following form:

$$ds^2 = -dt^2 + a^2(t)\gamma_{ij}dx^i dx^j, \quad (4)$$

where $(i, j = 1, 2, 3)$ and the line element $d\ell^2 = \gamma_{ij}dx^i dx^j$ describes a maximally symmetric three-dimensional space that may be Euclidean (flat), hyperbolic, or spherical.^d For the flat

^cSee http://lambda.gsfc.nasa.gov/links/experimental_sites.cfm for an extensive compilation of CMB experiments with links to their websites. The book [150] provides an insightful account emphasizing the early history of CMB observations with contributions from many of the major participants.

^dMore generally, the three-dimensional line element

$$ds^2 = \gamma_{ij}dx^i dx^j = \frac{dx_1^2 + dx_2^2 + dx_3^2}{\left(1 + \left(\frac{k}{4}\right)(x_1^2 + x_2^2 + x_3^2)\right)^2},$$

where $k = +1, 0$, or -1 corresponds to spherical, flat (Euclidean), or hyperbolic three-dimensional geometry, respectively. Apart from an overall change of scale, these are the only geometries satisfying the hypotheses of spatial homogeneity and isotropy. By substituting $\tan(\chi/2) = r/2$ or $\tanh(\chi/2) = r/2$ for the cases $k = +1$ or

case, which is the most important and most often discussed, Eq. (4) takes the form

$$ds^2 = -dt^2 + a^2(t)[dx_1^2 + dx_2^2 + dx_3^2]. \quad (5)$$

Here $a(t)$ represents the *scale factor* of the universe. Under the assumption of homogeneity and isotropy, the stress-energy tensor (expressed as a mixed tensor with one contravariant and one covariant index) must take the form

$$T_{\mu}{}^{\nu} = \begin{pmatrix} \rho(t) & 0 & 0 & 0 \\ 0 & p(t) & 0 & 0 \\ 0 & 0 & p(t) & 0 \\ 0 & 0 & 0 & p(t) \end{pmatrix}. \quad (6)$$

The Einstein field equations $G_{\mu\nu} = R_{\mu\nu} - (1/2)g_{\mu\nu}R = (8\pi G)T_{\mu\nu}$ may be reduced to the two equations

$$H^2(t) \equiv \frac{\dot{a}^2(t)}{a^2(t)} = \frac{8\pi G_N}{3}\rho(t) - \frac{k}{a^2(t)} \quad (7)$$

and

$$\frac{\ddot{a}(t)}{a(t)} = -\frac{4\pi G}{3}(\rho + 3p). \quad (8)$$

(For more details, see for example the discussion in the books by Weinberg [230] or Wald [227].)

The above discussion, which included only general relativity, is incomplete because no details concerning the dynamics of $\rho(t)$ and $p(t)$ have been given. The only constraint imposed by general relativity is stress-energy conservation, which in the most general case is expressed as $T_{\mu\nu}{}^{;\nu} = 0$, but in the special case above takes the form

$$\frac{d\rho(t)}{dt} = -3H(t)[\rho(t) + p(t)]. \quad (9)$$

The relationship between ρ and p is known as the equation of state, and for the special case of a perfect fluid p depends only on ρ and on no other variables. Two special cases are of particular interest: a nonrelativistic fluid, for which $p/\rho = 0$, and an ultrarelativistic fluid, for which $p/\rho = 1/3$. Until the mid-90s it was commonly believed that except at the very beginning of the universe, a two-component fluid consisting of a radiation component and matter component suffices to account for the stress-energy filling the universe. In such a model

$$\rho(t) = \rho_{m,0} \left(\frac{a_0}{a(t)} \right)^3 + \rho_{r,0} \left(\frac{a_0}{a(t)} \right)^4. \quad (10)$$

Here the subscript 0 refers to the present time. For the radiation component, there is obviously the contribution from the CMB photons, whose discovery was recounted above in Sec. 1. If we assume that the universe started as a plasma at some very large redshift with a certain baryon

$k = -1$, we may obtain the more familiar representations $ds^2 = d\chi^2 + \sin^2 \chi d\Omega_{(2)}^2$ or $ds^2 = d\chi^2 + \sinh^2 \chi d\Omega_{(2)}^2$, respectively, where $d\Omega_{(2)}^2 = d\theta^2 + \sin^2 \theta d\phi^2$.

number density, most conveniently parametrized as a baryon-to-photon or baryon-to-entropy ratio, we would conclude that there was statistical equilibrium early on between the various species, and from this assumption we can calculate the neutrino density today. It turns out that the neutrinos are colder than the photons because the neutrinos fell out of statistical equilibrium before the electrons and positrons annihilated. The e^+e^- annihilation had the effect of heating the photons relative to the neutrinos, because all the entropy that was in the electrons and positrons was dumped into the photons. Consequently, assuming a minimal neutrino sector, we can calculate the number of effective bosonic degrees of freedom due to the cosmic neutrino background, which according to big bang theory must be present but has never been detected. Measuring the number of baryons in the universe today is more difficult, and is the subject of an extensive literature. The realization of a need for some additional nonbaryonic “dark” matter dates back to Fritz Zwicky’s study of the Coma cluster in 1933 and is a long story that we do not have time to go into. Today “cold dark matter” is part of the concordance model, where the name simply means that whatever the details of this extra component may be (the lightest supersymmetric partner of the ordinary particles in the Standard electroweak model, the axion, or yet something else), for analyzing structure formation in the universe, we can treat this component as nonrelativistic (cold) particles that can be idealized as interacting only through gravitation.

In the mid-1990s it was realized that a model where the stress-energy included only matter and radiation components could not account for the observations. A crucial observation for many researchers was the measurement of the apparent luminosities of Type Ia supernovae as a function of redshift [158, 196], although at that time there were already several other discordant observations indicating that the universe with only matter and radiation could not account for the observations.^e To reconcile the observations with theory, another component having a large negative pressure, such as would arise from a cosmological constant, was required.

A cosmological constant makes a contribution to the stress-energy $T_{\mu\nu}$ proportional to the metric tensor $g_{\mu\nu}$ meaning that $p = -\rho$ exactly. This relation inserted into the right-hand side of Eq. (9) implies that any expansion (or contraction) does not change the contribution to the density from the cosmological constant.

With a cosmological constant, the density of the universe scales in the following manner:

$$\rho(t) = \rho_{\Lambda,0} \left(\frac{a_0}{a(t)} \right)^0 + \rho_{m,0} \left(\frac{a_0}{a(t)} \right)^3 + \rho_{r,0} \left(\frac{a_0}{a(t)} \right)^4. \quad (11)$$

The cosmological constant is most important at late times, when its density rapidly comes to dominate over the contribution from nonrelativistic matter (consisting according to our best current understanding of baryons and a so-called cold dark matter component). It is customary to express the contributions of each component as a fraction of the critical density $\rho_{\text{crit}} = 3H^2/8\pi G$, which would equal the total density if the universe were exactly spatially flat. For the i th component, we define $\Omega_i = (\rho_i/\rho_{\text{crit}})$.

From the present data, we do not know whether the new component (or components) with a large negative pressure is a cosmological constant, although current observations indicate that $w = p/\rho$ for this component must lie somewhere near $w = -1$. A key question of many of the major initiatives of contemporary observational cosmology is to measure w (and its evolution in time) in order to detect a deviation of the behavior of the dark energy from that predicted by a cosmological constant.

^eSee for example some of the contributions in Ref. [222] and references therein.

The earliest probe of the hot big bang model arises from comparing the primordial light element abundances as inferred from observations to the theory of primordial nucleosynthesis. In a hot big bang scenario, there is only one free parameter the baryon-to-photon ratio η_B , or equivalently, the baryon-to-entropy ratio η_S , which is related to the former by a constant factor. As discussed above, in the hot big bang theory at early times, in the limit as $a(t) \rightarrow 0$, we have $\rho \rightarrow \infty$, and $T \rightarrow \infty$. For calculating the primordial light element abundances, we do not need to extrapolate all the way back to the initial singularity, where these quantities diverge. Rather it suffices to begin the calculation at a temperature sufficiently low so that all the baryon number of the universe is concentrated in nucleons (rather than in free quarks), but high enough so that there are only protons and neutrons rather than bound nuclei consisting of several nucleons, and so that the reaction



(as well as related reactions) proceeds at a rate faster than the expansion rate of the universe H . Under this assumption, the ratio of protons to neutrons is determined by an equilibrium condition expressed in terms of chemical potentials

$$\mu(p) + \mu(e^-) = \mu(n) + \mu(\nu_e) + \Delta M, \quad (13)$$

where

$$\Delta M = M_N - M_P - M_e = 939.56 \text{ MeV} - 938.27 \text{ MeV} - 511 \text{ KeV} = 0.78 \text{ MeV}. \quad (14)$$

At first, when $T \gg (\Delta M)$, the protons and neutrons have almost precisely equal abundances, but then, as the universe cools down and expands, the neutrons become less abundant than the protons owing to the neutron's slightly greater mass. Then the reactions (12) freeze out—that is, their rate becomes small compared to H —and the neutron-proton ratio becomes frozen in. Subsequently protons and neutrons fuse to form deuterium, almost all of which combines to form ^4He , either directly from a pair of deuterons or through first forming ^3He , which subsequently fuses with a free neutron. Almost all the neutrons that do not decay end up in the form ^4He , because of its large binding energy relative to other low A nuclei, but trace amounts of other light elements are also produced. Even though other heavier nuclei have a larger binding energy per nucleon and their production would be favored by equilibrium considerations, the rates for their production are too small, principally because of the large Coulomb barrier that must be overcome.

In primordial big bang nucleosynthesis (BBN) the only free parameter is η_B . Since nucleosynthesis takes place far into the epoch of radiation domination, the density as a function of temperature is determined by the equation $\rho(T) = (\pi^2/30)N_{\text{rel}}T^4$ where N_{rel} is the effective number of bosonic degrees of freedom. The expansion rate then is important because it determines for example how many neutrons are able to be integrated into nuclei heavier than hydrogen before decaying. Based on the particles known to us that are ultrarelativistic during nucleosynthesis, the photon, electron, positron, neutrinos, and antineutrinos, we think that we know what value N_{rel} should have. But nucleosynthesis can be used to test for the presence of extra relativistic degrees of freedom. We shall see later that the CMB can also be used to constrain N_{rel} . For a review with more details about primordial nucleosynthesis, see Ref. [228].

3 Cosmological Perturbation Theory: Describing a Nearly Perfect Universe Using General Relativity

The broad brush account of the history of the universe presented in the previous section tells an average story, where spatial homogeneity and isotropy have been assumed. As we shall see, early on, at large z , this story is not far from the truth, especially on large scales. But a universe that is exactly homogeneous and isotropic would be quite unlike our own, in that there would be no clustering of matter, observed very concretely in the form of galaxies, clusters of galaxies, and so forth. In this section, we present a brief sketch of the theory of cosmological perturbations. For excellent reviews with a thorough discussion of the theory of cosmological perturbations in the framework of general relativity, see Refs. [103] and [142].

For the “scalar” perturbations,^f we may write the line element for the metric with its linearized perturbations $\Phi(\mathbf{x}, \eta)$ and $\Psi(\mathbf{x}, \eta)$ in the following form:

$$ds^2 = a^2(\eta)[-(1 + 2\Phi)d\eta^2 + (1 - 2\Psi)d\mathbf{x}^2]. \quad (15)$$

The functions $\Psi(\mathbf{x}, \eta)$ and $\Phi(\mathbf{x}, \eta)$ are the Newtonian gravitational potentials. At low velocities $\Psi(\mathbf{x}, \eta)$ is most relevant, but $\Phi(\mathbf{x}, \eta)$ can be probed observationally using light or some other type of ultrarelativistic particles. When there are no anisotropic stresses (i.e., all the partial pressures of the stress-energy tensor are equal), $\Phi = \Psi$.

For a universe filled with a perfect fluid with an equation of state $p = p(\rho)$, the evolution of the Newtonian gravitational potential $\Phi(\mathbf{x}, \eta)$ is governed by the equation (see Ref. [142] for a derivation and more details)

$$\Phi'' + 3\mathcal{H}(1 + c_s^2)\Phi' - c_s^2\nabla^2\Phi + [2\mathcal{H}' + (1 + 3c_s^2)\mathcal{H}^2]\Phi = 0, \quad (16)$$

where $c_s^2 = dp/d\rho$, $\mathcal{H} = a'/a$, and $' = d/d\eta$. Here η is the conformal time, related to the more physical proper time by the relation $dt = a(\eta)d\eta$.

If the spatial derivative term (i.e., $\nabla^2\Phi$) is neglected, which is an approximation valid on superhorizon scales, then the derived quantity [10, 128]

$$\zeta = \Phi + \frac{2}{3} \frac{(\Phi + \mathcal{H}^{-1}\Phi')}{(1 + w)}, \quad (17)$$

(where $w = p/\rho$) is conserved on superhorizon scales. This approximate invariant, which can be related to the spatial curvature of the surfaces of constant density, is invaluable for relating perturbations at the end of inflation (or some other very early noninflationary epoch) to the later times of interest in this chapter. This property is particularly useful given our ignorance of the intervening epoch, the period of “reheating” or “entropy generation,” the details of which are unknown and highly model dependent.

To understand the qualitative behavior of the above equation, it is important to focus on the role of the Hubble parameter $H(t) = \dot{a}(t)/a(t)$, which at time t defines the dividing

^fIn the theory of cosmological perturbations, the terms “scalar,” “vector,” and “tensor” are given a special meaning. A tensor of any rank that can be constructed using derivatives acting on a scalar function and the Kronecker delta is regarded as a “scalar”. A quantity that is not a “scalar” but can be constructed in the same way from a 3-vector field is regarded as “vector,” and a “tensor” is a second-rank tensor with its “scalar” and “vector” components removed. Under these definitions, the linearized perturbation equations reduce to a block diagonal form in which the “scalar,” “vector,” and “tensor” sectors do not talk to each other.

line between superhorizon modes [for which $|\mathbf{k}_{\text{phys}}| \lesssim H(t)$] and subhorizon modes [for which $|\mathbf{k}_{\text{phys}}| \gtrsim H(t)$].⁸ This distinction relates to the relevance of the spatial gradient terms in the evolution equations for the cosmological perturbations. This same distinction may be re-expressed in terms of the conformal time η and the co-moving wavenumber \mathbf{k} , where $\mathcal{H} = a'/a$ takes the place of $H = \dot{a}/a$, with superhorizon meaning $|\mathbf{k}| \lesssim \mathcal{H}(t)$ and subhorizon meaning $|\mathbf{k}| \gtrsim \mathcal{H}(t)$. Here dots denote derivatives with respect to proper time whereas the primes denote derivatives with respect to conformal time. It turns out that for calculations, working with conformal time and co-moving wavenumbers is much more convenient than working with physical variables.

What happens to the perturbations as the universe expands depends crucially on whether the co-moving horizon size is expanding or contracting. During inflation, or more generally when $w < -1/3$, the co-moving horizon size is contracting. This means that the dynamics of Fourier modes, which initially hardly felt the expansion of the universe, become more and more affected by the expansion of the universe. Terms proportional to H and H^2 in the evolution equations are becoming increasingly relevant whereas the spatial gradient terms are becoming increasingly irrelevant as the mode “exits” the horizon, finally to become completely “frozen in” on superhorizon scales. During inflation a mode starts far within the horizon and crosses the horizon at some moment during inflation. At the end of inflation, all the modes of interest lie frozen in, far outside the horizon.

During inflation, $w = p/\rho$ was slightly more positive than -1 . Formally inflation ends when w crosses the milestone $w = -1/3$, which is when the co-moving horizon stops shrinking and starts to expand. This moment roughly corresponds to the onset of “reheating” or “entropy generation,” when the vacuum energy of the inflaton field gets converted into radiation, or equivalently ultrarelativistic particles, which afterward presumably constitute the dominant contribution to the stress-energy T_{μ}^{ν} , so that $w \approx 1/3$. During the radiation epoch following “entropy generation,” modes successively re-enter the horizon again becoming dynamical. The degrees of freedom describing the modes are not the same as previously during inflation. This is at present our best-bet story of what likely happened in the very early universe. In this chapter, we shall be interested in the later history of the universe, when modes are re-entering the horizon.

We shall not enter into the details of how the primordial perturbations are generated from quantum fluctuations of the vacuum during inflation, instead referring the reader to the chapter by K. Sato and J. Yokoyama on *Cosmic Inflation* for this early part of the story. Nor shall we discuss alternatives to inflation. The original papers in which the scalar perturbations generated from inflation were first calculated include Mukhanov [140, 141, 139], Hawking [83], Guth [76], Starobinsky [218], and Bardeen *et al.* [11]. For early discussion of the generation of gravity waves during inflation and their subsequent imprint on the CMB, see Refs. [62, 197, 216, 3], and [217]. A more pedagogical account may be found for example in the books by Liddle and Lyth [125] and by Peacock [149], as well as in several review articles, including for example [129].

We emphasize the simplest type of cosmological perturbations, known as primordial “adiabatic” perturbations. The fact that the perturbations are primordial means that at the late times of interest to us, only the growing adiabatic mode is present, because whatever the amplitude of the decaying mode may initially have been, sufficient time has passed for its

⁸Here “horizon” means “apparent horizon,” which depends only on the instantaneous expansion rate, unlike the “causal horizon,” which depends on the entire previous expansion history.

amplitude to decay away and thus become irrelevant. The term “adiabatic” deserves some explanation because its customary meaning in thermodynamics does not precisely correspond to how it is used in the context of cosmological perturbations. In a universe with only adiabatic perturbations, at early times all the components initially shared a common equation of state and common velocity field, and moreover on surfaces of constant total density, the partial densities of the components are also spatially constant. This is the state of affairs initially, on superhorizon scales, but subsequently after the modes enter the horizon, the different components can and do separate.

Adiabatic modes are the simplest possibility for the primordial cosmological perturbations, but they are not the only possibility. Isocurvature perturbations where the equation of state varies spatially are also possible, as discussed in detail for example in Refs. [22], [28] and [98] references therein. For isocurvature perturbations, the ratios of components vary on a constant density surface, on which the spatial curvature is constant as well. However the ratios between the components are allowed to vary. As the universe expands, these variations in the equation of state eventually also generate curvature perturbations. It might be argued that the isocurvature modes should generically be expected to have been excited with some nonvanishing amplitude in multi-field models of inflation. For recent constraints on isocurvature perturbations from the CMB, see Planck Inflation 2013 [175] and the extensive list of references therein.

4 Characterizing the primordial power spectrum

In the previous section, we defined the dimensionless invariant $\zeta(\mathbf{x})$, conserved on superhorizon scales, which can be used to characterize the primordial cosmological perturbations at some convenient moment in the early universe when all the relevant scales of interest lie far outside the horizon. Because this quantity is conserved on superhorizon scales, the precise moment chosen is arbitrary within a certain range. The existence of a quantity conserved on superhorizon scales allows us to make precise predictions despite our nearly complete ignorance of the details of reheating.

Assuming a spatially flat universe, we may expand $\zeta(\mathbf{x})$ into Fourier modes, so that

$$\zeta(\mathbf{x}) = \int \frac{d^3k}{(2\pi)^3} \zeta(\mathbf{k}) \exp[i\mathbf{k} \cdot \mathbf{x}]. \quad (18)$$

If spatial homogeneity and isotropy are assumed, the correlation function of the Fourier coefficients must take the form

$$\langle \zeta(\mathbf{k}) \zeta(\mathbf{k}') \rangle = (2\pi)^3 k^{-3} \mathcal{P}(k) \delta^3(\mathbf{k} - \mathbf{k}'), \quad (19)$$

which also serves as the definition of the function $\mathcal{P}(k)$ known as the primordial power spectrum. The k^{-3} factor is present so that $\mathcal{P}(k)$ is likewise dimensionless. An exactly *scale invariant* power spectrum corresponds to $\mathcal{P}(k) \sim k^0$. The meaning of scale invariance can be understood by writing the mean square fluctuation at a point as the following integral over wavenumber:

$$\langle \zeta^2(\mathbf{x} = 0) \rangle = \int_{-\infty}^{+\infty} d[\ln(k)] \mathcal{P}(k). \quad (20)$$

Changes of scale correspond to rigid translations in $\ln(k)$, and the only choice for $\mathcal{P}(k)$ that does not single out a particular scale is $\mathcal{P}(k) = (\text{constant})$.

5 Recombination, the Blackbody Spectrum, and Spectral Distortions

It is sometimes said that the CMB is the best blackbody in the universe. This is not true. Observationally the only way to test how close the CMB is from a perfect blackbody is to construct a possibly better artificial blackbody and perform a differential measurement between the emission from the sky and this artificial blackbody as a function of frequency.

In our discussion of the CMB, we stressed that theory predicted a frequency spectrum having a blackbody form to a very high accuracy. This indeed was one of the striking predictions of the big bang theory, and the lack of any measurable deviation from the perfect blackbody spectral shape over a broad range of frequencies was probably one of the most important observational facts that led to the demise of the alternative steady state cosmological model. To date, the best measurements of the frequency spectrum of the CMB are still those made by the COBE FIRAS instrument [134, 135, 66]. FIRAS [136] made differential measurements comparing the CMB frequency spectrum on the sky to an artificial blackbody. Despite the many years that have gone by since COBE and the importance of measuring the absolute spectrum of the CMB, no better measurement has been carried out because improving on FIRAS would require going to space in order to avoid the spectral imprint of the Earth's atmosphere. However a space mission concept called PIXIE has been proposed that would essentially redo FIRAS but with over two orders of magnitude better sensitivity and with polarization sensitivity included [105]. While differences in temperature between different directions in the sky, particularly on small angular scales, can be measured from the ground, albeit with great difficulty, the same is not possible for measurements of the absolute spectrum.

From a theoretical point of view, even in the simplest minimal cosmological model with no new physics, deviations from a perfect blackbody spectrum are predicted that could be measured with improved observations of the absolute spectrum having a sensitivity significantly beyond that of FIRAS. It is often believed that when we look at the CMB, we are probing conditions in the universe at around last scattering—that is, around $z \approx 1100$ —and that the CMB photons are unaffected by what happened during significantly earlier epochs. This is not true. Although when $z \gtrsim 1100$, photons are frequently scattered by electrons randomizing their direction, causing them to move diffusively, this frequent scattering is inefficient at equilibrating the kinetic temperature of the electrons to the energy spectrum of the photons and vice versa owing to the smallness of the dimensionless parameter E_γ/m_e , where E_γ is a typical photon energy. This ratio gives the order of magnitude of the fractional energy exchange due to electron recoil for a typical collision. Given that in this limit the approach to a blackbody spectrum is a diffusive process, we would estimate that $(E_\gamma/m_e)^2$ collisions correspond to one decay time of the deviation of the photon energy spectrum from the equilibrium spectrum. Plugging in $E_\gamma \approx k_B T_{z=1100} \approx 0.3 \text{ eV}$, we get $(E_\gamma/m_e)^2 \approx 4 \times 10^{10}$! Thomson scattering, however, cannot equilibrate the photon number density with the available energy density, so with Thomson scattering alone, an initially out of equilibrium photon energy distribution, for example as the result of some sort of energy injection, would generically settle down to a photon phase space distribution having a positive chemical potential. Processes such as Bremsstrahlung and its inverse or double Compton scattering are required to make the chemical potential decay to zero, and these processes freeze out at $z \approx 10^6$ [95]. Therefore any energy injection between $z \approx 10^6$ and $z \approx 10^3$ will leave its mark on the absolute spectrum

of the CMB photons, either in the form of a so-called μ distortion, or for energy injected at later times, in the form of a more complicated energy dependence.

A broad range of interesting early universe science can be explored by searching for deviations from a perfect blackbody spectrum. Some of the spectral distortions are nearly certain to be present, while others are of a more speculative nature. On the one hand, y -distortions in the field (that is, away from galaxy clusters where the y -distortion is compact and particularly large) constitute a nearly certain signal, as do the spectral lines from cosmological recombination. But sources like decaying dark matter [31] may or may not be present. Another interesting source of energy injection arise from Silk damping [207, 89] of the primordial power spectrum on small scales, beyond the range of scales where the primordial power spectrum can be probed by other means. If a space-based instrument is deployed with the requisite sensitivity, a formidable challenge will be to distinguish these signals from each other, and also from the more mundane galactic and extragalactic backgrounds. From this discussion one might conclude, borrowing terminology from stellar astrophysics, that the CMB “photosphere” extends back to around $z \approx 10^6$.

6 Sachs-Wolfe Formula and More Exact Anisotropy Calculations

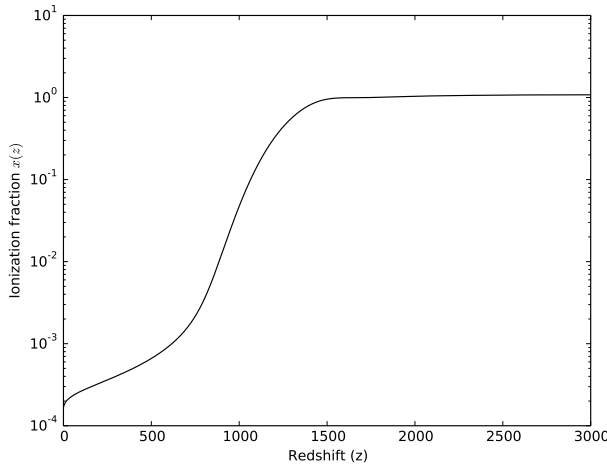


Figure 11: **Ionization fraction as function of redshift with effect of late-time ionizing radiation ignored.** Calculated using the code *Cosmo Rec* by Jens Chluba (for details see Ref. [213]).

as “recombination” (despite the fact that the universe had never previously been neutral), the photons cease to rescatter and free stream toward us today [152]. This last statement is only 90% accurate, because the late-time reionization starting at about $z \approx 6-7$ causes about 10%

At early times ($z \lesssim 1100$) the universe is almost completely ionized and the photons scatter frequently with free charged particles, primarily with electrons because the proton–photon scattering cross-section is suppressed by a factor of (m_e/m_p) . During this period the plasma consisting of baryons, leptons, and photons may be regarded as a single tightly-coupled fluid component, almost inviscid but with a viscosity relevant on the shortest scales of interest for the calculation of the CMB temperature and polarization anisotropies. Later, as the universe cools the electrons and protons (and other nuclei) combine to form neutral atoms whose size greatly exceeds the thermal wavelength of the photons, rendering the universe almost transparent. During this process, known

of the CMB photons to be rescattered. The effect of this rescattering on the CMB anisotropies will be discussed in detail in Sec. 7.5. It is during this transitional epoch, situated around $z \approx 1100$, that the CMB temperature and polarization anisotropies were imprinted. Thus when we observe the microwave anisotropies on the sky today, we are probing the physical conditions on a sphere approximately 47 billion light years in radius today,^h or more precisely the intersection of our past light cone at the surface of constant cosmic time at $z \approx 1100$. This sphere is known as the surface of last scatter or the last scattering surface.

The transition from a universe that is completely opaque to the blackbody photons, in which the tight-coupling approximation holds for the baryon-lepton plasma because the photon mean free path is negligible, to a universe that is virtually transparent is not instantaneous. This fact implies that the last scattering surface (LSS) is not infinitely thin, rather having a finite width that must be taken into account for calculating the small angle CMB anisotropies, because this profile of finite thickness smears out the small-scale three-dimensional inhomogeneities as they are projected onto the two-dimensional celestial sphere. Figure 11 shows a plot of the ionization history of the universe (not taking into account the late-time reionization at $z \gtrsim 6$ mentioned above). (For a more detailed discussion of the early ionization history of the universe and the physics by which it is determined, see for example Refs. [85, 202, 203, 220] and [30]).

The first calculation of the CMB temperature anisotropies predicted in a universe with linearized cosmological perturbations was given by Sachs and Wolfe in their classic 1967 paper [200] (see also Ref. [154]). In their treatment, the LSS surface is idealized as the surface of a three-dimensional sphere—in other words, the transition from tight-coupling to transparency is idealized to be instantaneous. Locally, on this surface the photon-baryon fluid is subject to two kinds of perturbations: (i) perturbations in density $\delta_{\gamma-b}$ and (ii) velocity perturbations \mathbf{v}_b . The former translate into fluctuations in the photon blackbody temperature T_γ , in “intrinsic” temperature fluctuations at the last scattering surface with $\delta T_\gamma / \bar{T}_\gamma$ and the second translate into a Doppler shift of the CMB temperature. If there were no metric perturbations, we would simply have

$$\frac{\delta T_f(\hat{\Omega})}{\bar{T}_f} = \frac{\delta T_i(\hat{\Omega})}{\bar{T}_i} - \frac{1}{c} \delta \mathbf{v}_\gamma \cdot \hat{\Omega}, \quad (21)$$

where $\hat{\Omega}$ is the unit outward normal on the last scattering surface. But there are also additional terms due to the metric perturbations, and careful calculations along the perturbed geodesics yield the following modification to the above equation:

$$\frac{\delta T_f(\hat{\Omega})}{\bar{T}_f} = \frac{\delta T_i(\hat{\Omega})}{\bar{T}_i} - \frac{1}{c} \delta \mathbf{v}_\gamma \cdot \hat{\Omega} + \Phi + \int_{\eta_i}^{\eta_f} d\eta (\Phi' + \dot{\Psi}'), \quad (22)$$

where the metric perturbations are parametrized as in Eq. (15) using conformal Newtonian gauge.ⁱ This equation is known as the Sachs-Wolfe formula. Because of the approximations involved, the Sachs-Wolfe formula is not used for accurate calculations (especially on small

^hThe radius of this sphere in terms of today’s comoving units is larger than the age of the universe (approximately 13.8 Gyr) converted into a distance owing to the expansion of the universe.

ⁱThe Sachs-Wolfe formula as given here only includes the “scalar” perturbations. The formula can be generalized to include “vector” and “tensor” contributions, for which the only contributions are from the Doppler and ISW (integrated Sachs-Wolfe) terms.

angular scales). However, it offers a good approximation to the CMB anisotropies on large angular scales and provides invaluable intuition that is lacking in the more precise treatments.

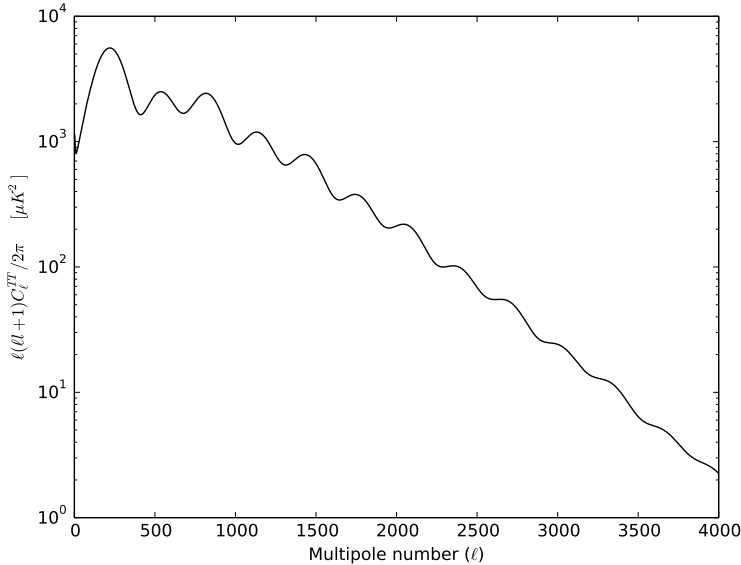


Figure 12: **Theoretical CMB spectrum.** CMB temperature power spectrum predicted for a model with only the adiabatic growing mode excited, as in the standard concordance cosmological model, is shown. The theoretical model here assumes the best-fit cosmological parameters taken from the Planck 2013 Results for Cosmology [170].

nian gauge. It is believed that this gauge choice is somehow more “physical” because at least to linear order, the gauge conditions lead to a unique choice of gauge. It is certainly nice to have a gauge condition leading to a unique choice of coordinates, but this uniqueness comes at a price. The Newtonian gauge condition is “nonlocal” because of its reliance on the decomposition of $h_{\mu\nu}$ into “scalar,” “vector,” and “tensor” components, which requires information extending all the way out to spatial infinity. But no one has ever seen all the way out to spatial infinity. For this reason, the Newtonian potentials Ψ and Φ are unphysical because they cannot be measured. Their determination would require information extending beyond our horizon.

We may further simplify Eq. (22) assuming that only the adiabatic growing mode has been excited. Using the fact that δT_i and \mathbf{v} are not independent of Φ , we obtain the often cited

^j“Gauge dependence” here means invariance under general coordinate transformations, which consistent with the linear approximation above may be truncated at linear order.

A few words about gauge dependence,^j an issue that renders linearized perturbation theory within the framework of general relativity somewhat messy. While the final observed anisotropy $\delta T_f(\hat{\Omega})/\bar{T}_f$ is the same in all coordinate systems (except for the monopole and dipole terms), the attribution of the total anisotropy among the various terms (i.e., intrinsic temperature fluctuation, Doppler, gravitational redshift, integrated Sachs-Wolfe) depends on the choice of coordinates. We may for example choose coordinates so that the photon temperature serves as the time coordinate, making the first term disappear, or alternatively, we may make the Doppler term disappear by making our co-moving observers move with the local photon rest frame.

Students of cosmology are sometimes misled into believing the solution to these ambiguities is to use conformal Newtonian gauge, or equivalently the “gauge invariant” formalism, which is equivalent to transforming to conformal Newtonian gauge.

result

$$\frac{\delta T}{T} = -\frac{\Phi}{3} - \mathbf{v} \cdot \hat{\Omega} + \int d\eta(\Phi' + \Psi'), \quad (23)$$

although the $-1/3$ factor is not quite right because a matter-dominated evolution for $a(t)$ is assumed rather than a more careful treatment taking into account matter-radiation equality occurring at around $z_{eq} \approx 3280$. (For a discussion see Ref. [233].)

Using this result and ignoring the integrated Sachs-Wolfe term, we obtain

$$\frac{\delta T}{T}(\hat{\Omega}) = -\frac{\Phi}{3} - \mathbf{v} \cdot \hat{\Omega}. \quad (24)$$

On large angular scales—that is, large compared to the angle subtended by the horizon on the last scattering surface—the first term dominates. The modes labeled by \mathbf{k} obey an oscillatory system of coupled ODEs, and at the putative big bang each mode starts with a definite sharp phase corresponding to the part of the cycle where $\mathbf{v} = 0$. It is only at horizon crossing that the phase has evolved sufficiently for the velocity term to contribute appreciably to the CMB anisotropy. Figure 12 shows the calculated form of the CMB temperature power spectrum. For $\ell \lesssim 100$, $\Delta T/T \approx -\Phi/3$ provides an adequate explanation for this leftmost plateau of the curve, but at higher ℓ a rise to a first acoustic peak, situated at about $\ell \approx 220$, is observed followed by a series of decaying secondary oscillations.

A more accurate integration of the evolution of the adiabatic mode up to last scattering can be obtained in the fluid approximation. This approximation assumes that the stress-energy content of the universe can be described by a fluid description consisting of two components coupled to each other only by gravity [205]. However more accurate calculations must go beyond the fluid approximation using a Boltzmann formalism that includes higher order moments.

However, before describing the Boltzmann formalism, capable of describing this intermediate regime for the photons, we note one final shortcoming of the approximation with tight-coupling and instantaneous recombination—namely, the treatment of polarization. We present here an approximate, heuristic treatment in order to provide intuition.

The scattering of photons by electrons is polarization dependent, and this effect leads to a polarization of the CMB anisotropy when the fact that recombination does not occur instantaneously is taken into account. The Thomson scattering cross-section of a photon off an electron is given by

$$\frac{d\sigma}{d\Omega} = \left(\frac{e^2}{mc^2}\right)^2 (\hat{\epsilon}_i \cdot \hat{\epsilon}_f)^2, \quad (25)$$

where $\hat{\epsilon}_i$ and $\hat{\epsilon}_f$ are the initial and final polarization vectors, respectively.

To see qualitatively how polarization of the CMB comes about, let us for the moment assume that the photons coming from next-to-last scattering are unpolarized and calculate the polarization introduced at last scattering, as indicated in Fig. 13. Measuring photons with one linear polarization selects photons that propagated from next-to-last to last scattering at a small angle to the axis of linear polarization, while photons with the other linear polarization tend to come from a direction from next-to-last to last scattering with a small angle with the other axis. Consequently, measuring the polarization amounts to measuring the temperature

quadrupole as seen by the electron of last scattering. If we make the simplifying assumption that the radiation emanating from next-to-last scattering is unpolarized, we obtain the following expression for the Stokes parameters from the linear polarization,

$$\begin{aligned} \begin{pmatrix} Q \\ U \end{pmatrix}_{l.s.} &= \int_{\rho=0}^{\rho=\rho_{\max}} d(-\exp[-\tau(r_{l.s.} + \rho)]) \int d\hat{\Omega} \sin^2 \theta \begin{pmatrix} \cos \phi \\ \sin \phi \end{pmatrix} \\ &\times T(\rho \sin \theta \cos \phi, \rho \sin \theta \sin \phi, r_{l.s.} + \rho \cos \theta). \end{aligned} \quad (26)$$

Here we assume that the line of sight is along the z direction. The expression gives two of the five components of quadrupole moment of the temperature as seen by the electron at last scattering, and after integration along the line of sight would give the total linear polarization with the polarization at next-to-last scattering neglected.

7 What Can We Learn From the CMB Temperature and Polarization Anisotropies?

The previous Section showed how starting from Gaussian isotropic and homogeneous initial conditions on superhorizon scales, the predicted CMB temperature and polarization anisotropies are calculated, describing in detail all the relevant physical processes at play. In this Section, we turn to the question of what we can learn about the universe from these observations. We focus on how to exploit the temperature and polarization two-point functions, which under the assumption of Gaussianity would summarize all the available information characterizing the underlying stochastic process. Gaussianity is a hypothesis to be tested using the data, as discussed separately in Sec. 9.

7.1 Character of primordial perturbations: adiabatic growing mode versus field ordering

In the aftermath of the COBE/DMR announcement of the detection of the CMB temperature anisotropy, two paradigms offered competing explanations for the origin of structure in the early universe. On the one hand, there was cosmic inflation, which in its simplest incarnations predicts homogeneous and isotropic Gaussian initial perturbations where only the adiabatic growing mode is excited. On the other hand, there was also another class of models in which the universe is postulated initially to have been perfectly homogeneous and isotropic. However, subsequently a symmetry breaking phase transition takes place, with the order parameter field taking uncorrelated values in causally disconnected regions of spacetime. Then, as the universe expands and the co-moving size of the horizon grows, the field aligns itself over domains of increasingly large co-moving size, generally in a self-similar way. In many of these models, topological defects of varying co-dimension—such as monopoles, cosmic strings, and domain walls—arise after the phase transition, but textures where the spatial gradient energy is more diffusely distributed are also possible.^k In these models the contribution of the field ordering sector to the total energy is always subdominant, and cosmological perturbations are generated in a continuous manner extending to the present time. The stress-energy

^kFor the physics of topological defects, see Ref. [188] and for a comprehensive account emphasizing the connection to cosmology, see Ref. [226].

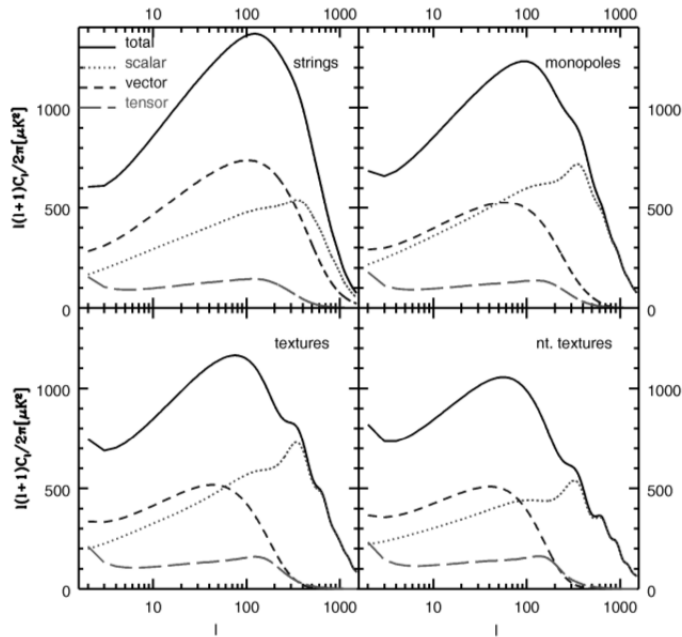


Figure 14: **Structure of acoustic oscillations: field ordering predictions.** These acoustic oscillation predictions from four field-ordering models are to be contrasted with the sharp, well-defined peaks in Fig. 12 as predicted by inflation. (Reprinted with permission from Ref. [155].) (*Credit: Pen, Seljak and Turok*)

$\Theta_{\mu\nu}$ from this sector sources perturbations in the metric perturbation $h_{\mu\nu}$. These metric perturbations in turn generate perturbations in the dominant components contributing to the stress-energy: the baryons, photons, neutrinos, and cold dark matter. In these models, the cosmological perturbations are not primordial, but rather are continuously generated so that the perturbations on the scale \mathbf{k} are generated primarily as the mode \mathbf{k} enters the apparent horizon [156]. This property implies that the decaying mode as well as the growing mode of the adiabatic perturbations is excited, and this fact has a spectacular effect on the shape of the predicted CMB power spectrum. While inflationary models, which excite only the growing mode, predict a series of sharp, well-defined acoustic oscillations, field ordering models predict broad, washed out oscillations or no oscillations at all in the angular CMB spectrum [5, 36, 155]. Heuristically one can understand this behavior by arguing that the positions of the peaks reflect the phase of the oscillations. Therefore, if both the growing and decaying modes are present in exactly equal proportion, there should be no oscillations in the angular spectrum. However, precise predictions require difficult numerical simulations and depend on the precise model for the topological defect or field ordering sector. Figure 14 shows the shape of the predicted CMB TT power spectrum for some field ordering models, to be compared with the predictions for minimal inflation shown in Fig. 12.

After COBE, a big question was whether improved degree-scale CMB observations would unveil the first Doppler peak followed by a succession of decaying secondary peaks at smaller angular scales, as predicted by an approximately scale invariant primordial power spectrum for the growing adiabatic mode, or whether some other shape would be observed, perhaps the one predicted by a field ordering model.

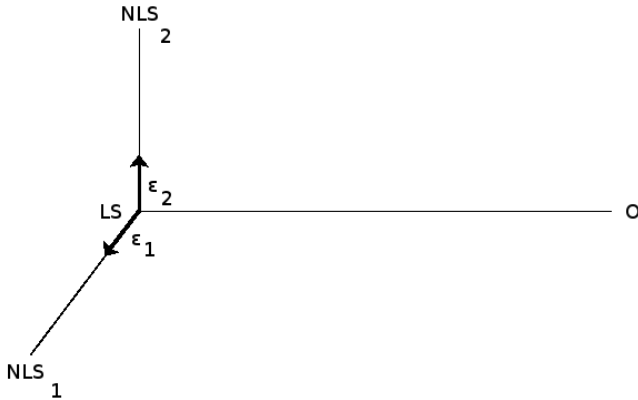


Figure 13: **Anisotropy of polarized Thomson scattering and origin of the CMB polarization.** We show two examples of photon scattering from (NLS) (next-to-last scattering) to (LS) (last scattering) and finally to the observer (at O .) The three segments in the diagram have been chosen mutually at right angles in order to maximize the effect, and for simplicity we assume that the radiation emanating from (NLS)₁ and (NLS)₂ is unpolarized. All the radiation that scatters coming from (NLS)₁ to (LS) and then towards O is completely linearly polarized in the $\hat{\epsilon}_2$ direction, because the other polarization is parallel to $(LS)O$ and thus cannot be scattered in that direction. Likewise, the scattered photons emanating from (NLS)₂ are completely linearly polarized in the orthogonal direction for the same reason. Consequently if there were only two sources as above, measuring the Stokes parameter Q at O amounts to measuring the difference in intensity between these two sources.

the free-streaming regime, must be modeled more realistically. This requires going beyond the fluid approximation, where the photon gas can be described by its first few moments. Modeling this transition faithfully requires a formalism with an infinite number of moments—that is, a formalism in which the fundamental dynamical variable is the photon phase space distribution function $f(\mathbf{x}, t, \nu, \hat{\mathbf{n}}, \hat{\epsilon})$ where ν is the photon frequency, and the unit vectors $\hat{\mathbf{n}}$ and $\hat{\epsilon}$ denote the photon propagation direction and electric field polarization, respectively. The perturbations about a perfect blackbody spectrum are small, so truncating at linear order provides an adequate approximation. Moreover, Thomson scattering is independent of frequency, and thus (to linear order) does not alter the blackbody character of the spectrum. Consequently, a description in terms of a perturbation of the blackbody temperature that depends on spacetime position, propagation direction, and polarization direction can be used in

We already presented (in Sec. 1) the experimental results for the first observations of the acoustic oscillations and their subsequent precise mapping (see in particular Figs. 5, 4 and 10.) The data clearly favor simple models of inflation producing adiabatic growing mode perturbations with an approximately scale invariant power spectrum and exclude scenarios where topological defects serve as the primary source for the initial density perturbations. However, models including a small admixture of defect induced perturbations cannot be ruled out [178].

7.2 Boltzmann hierarchy evolution

In the previous section, we derived the Sachs-Wolfe formula, which provides an intuitive understanding of how the CMB anisotropies are imprinted. The Sachs-Wolfe treatment provides an approximate calculation of the CMB temperature anisotropies, correctly capturing their qualitative features. However to calculate predictions accurate at the sub-percent level, as is required for confronting current observations to theoretical models, the transition from the tight-coupling regime to transparency, or

place of the full six-dimensional phase space density, thus reducing the number of dimensions of the phase space by one.¹ For a calculation correct to second order, a description in terms of a perturbed temperature would not suffice.

As before we consider a single “scalar” Fourier mode \mathbf{k} of flat three-dimensional space, so that an $\exp[i\mathbf{k} \cdot \mathbf{x}]$ spatial dependence is implied. A complication in describing polarization arises in specifying a basis, which preferably is accomplished using only scalar quantities. We describe the polarization using the unit vectors $\hat{\mathbf{n}}$ and $\hat{\mathbf{k}}$ to define the unit vectors

$$\hat{\boldsymbol{\theta}} = \frac{\hat{\mathbf{k}} - \hat{\mathbf{n}}(\hat{\mathbf{n}} \cdot \hat{\mathbf{k}})}{\|\hat{\mathbf{k}} - \hat{\mathbf{n}}(\hat{\mathbf{n}} \cdot \hat{\mathbf{k}})\|}, \quad \hat{\boldsymbol{\phi}} = \frac{\hat{\mathbf{n}} \times \hat{\mathbf{k}}}{\|\hat{\mathbf{n}} \times \hat{\mathbf{k}}\|}, \quad (27)$$

which together with photon propagation direction $\hat{\mathbf{n}}$ form an orthonormal basis. We thus describe the Stokes parameters of the radiation propagating along $\hat{\mathbf{n}}$ as follows:

$$\langle \mathcal{E}_a(\hat{\mathbf{n}}, \nu) \mathcal{E}_b(\hat{\mathbf{n}}, \nu) \rangle = I(\hat{\mathbf{n}}, \nu; \hat{\mathbf{k}}) \delta_{ab} + Q(\hat{\mathbf{n}}, \nu; \hat{\mathbf{k}}) [\hat{\boldsymbol{\theta}} \otimes \hat{\boldsymbol{\theta}} - \hat{\boldsymbol{\phi}} \otimes \hat{\boldsymbol{\phi}}]_{ab}. \quad (28)$$

For the “scalar” mode, the Stokes parameters U and V vanish in this basis.

The Thomson scattering cross-section does not vary with frequency, a property that provides substantial simplification. Suppose that at some initial time the photon distribution function has a blackbody dependence on frequency, with a blackbody temperature suffering only small linearized perturbations about an average temperature, and that these temperature perturbations depend on the spacetime position, propagation direction, and linear polarization direction. The frequency independence of Thomson scattering ensures that a photon distribution function initially having this special form will retain this special form during its subsequent time evolution. Initially, when tight-coupling is an excellent approximation, any deviation in the frequency dependence from a perfect blackbody spectrum decays rapidly. Moreover, any initial polarization is erased by the frequent scattering. Therefore a blackbody form described by a perturbation in the spectral radiance of the form

$$\delta I_\nu(\hat{\mathbf{n}}, \hat{\boldsymbol{\epsilon}}, \mathbf{x}, t) = \bar{T}_\gamma \frac{\partial B_\nu(T)}{\partial T} \Delta_{ab}(\hat{\mathbf{n}}, \mathbf{x}, t) \hat{\epsilon}^a \hat{\epsilon}^b \quad (29)$$

is well motivated. Here

$$B_\nu(T) = \left(\frac{2h\nu^3}{c^2} \right) \left(\exp \left[\frac{h\nu}{k_B T} \right] - 1 \right)^{-1} \quad (30)$$

is the spectral radiance for a blackbody at temperature T . The unperturbed spectral radiance is $I_{\nu,0}(\hat{\mathbf{n}}, \hat{\boldsymbol{\epsilon}}, \mathbf{x}, t) = B_\nu(T_\gamma(t))$, where $T_\gamma(t)$ is the photon temperature at cosmic time t in the unperturbed background expanding FLRW spacetime. (In Sec. 5, however, we discuss some interesting possible caveats to this assumption.) For the “scalar” mode of wavenumber \mathbf{k} , we may decompose

$$\Delta_{ab}(\hat{\mathbf{n}}, \mathbf{x}, t) = \Delta_T^{(\text{scl})}(\hat{\mathbf{n}}, \mathbf{x}, t) \delta_{ab} + \Delta_P^{(\text{scl})}(\hat{\mathbf{n}}, \mathbf{x}, t) (\hat{\theta}_a \hat{\theta}_b - \hat{\phi}_a \hat{\phi}_b). \quad (31)$$

¹Although written as a continuum variable. $\hat{\boldsymbol{\epsilon}}$ is in reality a discrete variable corresponding to the Stokes parameters (E, Q and U).

We now turn to the evolution of the variables $\Delta_T^{(\text{scl})}(\hat{\mathbf{n}}, t)$ and $\Delta_P^{(\text{scl})}(\hat{\mathbf{n}}, t)$. It is convenient, exploiting the symmetry under rotations about $\hat{\mathbf{k}}$, to expand

$$\begin{aligned}\Delta_T^{(\text{scl})}(\hat{\mathbf{n}}, t; \mathbf{k}) &= \sum_{\ell=0}^{\infty} \Delta_{T,\ell}^{(\text{scl})}(t; \mathbf{k}) (-i)^\ell (2\ell+1) P_\ell(\hat{\mathbf{k}} \cdot \hat{\mathbf{n}}), \\ \Delta_P^{(\text{scl})}(\hat{\mathbf{n}}, t; \mathbf{k}) &= \sum_{\ell=0}^{\infty} \Delta_{P,\ell}^{(\text{scl})}(t; \mathbf{k}) (-i)^\ell (2\ell+1) P_\ell(\hat{\mathbf{k}} \cdot \hat{\mathbf{n}}).\end{aligned}\tag{32}$$

The evolution of $\Delta_{T,\ell}^{(\text{scl})}$ and $\Delta_{P,\ell}^{(\text{scl})}$ is governed by the following infinite system of equations [130]:

$$\begin{aligned}\Delta_{T0}^{(\text{scl})} &= -k\Delta_{T1}^{(\text{scl})} + \phi', \\ \Delta_{T1}^{(\text{scl})} &= \frac{k}{3}(\Delta_{T0}^{(\text{scl})} - 2\Delta_{T2}^{(\text{scl})} + \psi) + a(t)n_e(t)\sigma_T \left(\frac{v_b}{3} - \Delta_{T1}^{(\text{scl})} \right), \\ \Delta_{T2}^{(\text{scl})} &= \frac{k}{5}(2\Delta_{T1}^{(\text{scl})} - 3\Delta_{T3}^{(\text{scl})}) + a(t)n_e(t)\sigma_T \left(\frac{\Pi}{10} + \Delta_{T2}^{(\text{scl})} \right), \\ \Delta_{T\ell}^{(\text{scl})} &= \frac{k}{(2\ell+1)} \{ \ell\Delta_{T(\ell-1)}^{(\text{scl})} - (\ell+1)\Delta_{T(\ell+1)}^{(\text{scl})} \} - a(t)n_e(t)\sigma_T \Delta_{T\ell}^{(\text{scl})}, \quad \text{for } \ell \geq 3, \\ \Delta_{P\ell}^{(\text{scl})} &= \frac{k}{(2\ell+1)} \{ \ell\Delta_{P(\ell-1)}^{(\text{scl})} - (\ell+1)\Delta_{P(\ell+1)}^{(\text{scl})} \} - a(t)n_e(t)\sigma_T \Delta_{P\ell}^{(\text{scl})} \\ &+ \frac{1}{2}a(t)n_e(t)\sigma_T \Pi \left(\delta_{\ell,0} + \frac{1}{5}\delta_{\ell,2} \right), \quad \text{for } \ell \geq 0,\end{aligned}\tag{33}$$

where

$$\Pi = \Delta_{T0}^{(\text{scl})} + \Delta_{P0}^{(\text{scl})} + \Delta_{P2}^{(\text{scl})}.\tag{34}$$

These equations are known as the *Boltzmann hierarchy* for the photon phase space distribution function. In the last line of Eq. (33) δ_{ab} denotes the Kronecker delta function. For practical numerical calculations, this infinite set of coupled equations must be truncated at some ℓ_{max} .

In principle, ignoring questions of computational efficiency, we could truncate the system of equations in (33) at some large ℓ_{max} , sufficiently above the maximum multipole number of interest today, and integrate the coupled system from some sufficiently early initial time to the present time t_0 to find the ‘‘scalar’’ temperature and polarization anisotropies today, which would be given by the following integrals over plane wave modes:

$$\begin{aligned}\Delta_T^{(\text{scl})}(\hat{\mathbf{n}}, t_0) &= \int d^3k \Delta_T^{(\text{scl})}(\hat{\mathbf{n}}, t_0; \mathbf{k}), \\ \Delta_P^{(\text{scl})}(\hat{\mathbf{n}}, t_0) &= \int d^3k \Delta_P^{(\text{scl})}(\hat{\mathbf{n}}, t_0; \mathbf{k}).\end{aligned}\tag{35}$$

This was the approach used in the COSMICS code [16], one of the first codes providing accurate computations of the CMB angular power spectrum. However in this approach much computational effort is expended at late times when there is virtually no scattering.

A computationally simpler but mathematically completely equivalent approach known as the line of sight formalism was introduced in Ref. [206]. The crucial idea is to express the

anisotropies today (at $\mathbf{x} = 0$ and $\eta = \eta - 0$) in terms of a line of sight integral, so that

$$\Delta_T^{(S)}(\hat{\mathbf{n}}) = \int_0^{\eta_0} d\eta \exp[-\tau(\eta)] \exp[ik(\eta - \eta_0)] \quad (36)$$

$$\times \left[\left(-\frac{d\tau}{d\eta} \right) \left(\Delta_{T0} + i\mu v_B + \frac{1}{2} P_2(\mu) \Pi \right) + (\phi' - ik\mu\psi) \right] \quad (37)$$

and

$$\Delta_P^{(S)}(\hat{\mathbf{n}}) = \int_0^{\eta_0} d\eta \exp[-\tau(\eta)] \exp[ik(\eta - \eta_0)] \left(-\frac{d\tau}{d\eta} \right) (1 - P_2(\mu)) \Pi \quad (38)$$

where $\Pi = \Delta_{T2}^{(S)} + \Delta_{P2}^{(S)} + \Delta_{P0}^{(S)}$. We may think of $\exp[-\tau(\eta)](-d\tau/d\eta)d\eta = \mathcal{V}(\eta)d\eta$ as a measure along the line of sight weighted according to where last scattering takes place. We shall call $\mathcal{V}(\eta)$ the visibility function. In Eq. (37), the first term represents the nonpolarized contribution at last scatter and the second term represents the contribution from the integrated Sachs-Wolfe effect. In Eq. (38) for the polarized anisotropy, the only contribution is from last scatter. It is convenient to rewrite the above integrals using integration by parts so that all spatial derivatives along the line of sight and occurrences of μ are eliminated, and in the process we also omit the monopole surface term at the endpoint corresponding to the observer as this contribution is not measurable. After this integration by parts, the integrals above take the form

$$\Delta_{T,P}^{(S)}(\hat{\mathbf{n}}) = \int_0^{\eta_0} d\eta \exp[ik\mu(\eta_0 - \eta)] \mathcal{S}_{T,P}^{(S)}((\eta_0 - \eta)\hat{\mathbf{n}}, \eta), \quad (39)$$

where the scalar source functions are

$$\begin{aligned} \mathcal{S}_T^{(S)} &= \exp[-\tau(\eta)](\phi' + \psi') + \mathcal{V} \left(\Delta_{T0} + \psi + \frac{v'_b}{k} + \frac{3\Pi'}{4k^2} \right) \\ &\quad + \mathcal{V}' \left(\frac{v_b}{k} + \frac{3\Pi'}{4k^2} \right) + \mathcal{V}'' \frac{3\Pi}{4k^2}, \\ \mathcal{S}_P^{(S)} &= \frac{3}{4k^2} (\mathcal{V}(k^2\Pi + \Pi'') + 2\mathcal{V}'\Pi' + \mathcal{V}''\Pi), \end{aligned} \quad (40)$$

and the primes denote derivatives with respect to conformal time η . Now that the spatial derivatives have been eliminated, it is no longer necessary to use the plane waves $\exp[ik\mu(\eta_0 - \eta)]$ as the eigenfunctions of the Laplacian operator with eigenvalue $-k^2$. It is convenient instead to use a spherical wave expansion with $j_\ell(k(\eta - \eta_0))$

$$\Delta_{\ell;A}^{(S)} = \int_0^{\eta_0} d\eta j_\ell(k(\eta_0 - \eta)) \mathcal{S}_A^{(S)}((\eta_0 - \eta)\hat{\mathbf{n}}, \eta), \quad (41)$$

where $A = T, P$.

The line of sight formulation results in a significant reduction of the computational effort required for computing the high ℓ coefficients for two reasons. First, the Boltzmann hierarchy can be truncated at low ℓ , because only moments up to $\ell = 2$ appear in the integral. Second, when the universe has become transparent, there is no longer any contribution from the Thomson scattering.

We express the initial state for the growing adiabatic mode at some early reference time whose exact value must be chosen after the epoch of entropy generation following inflation but before any of the relevant modes re-entered the horizon. We use the variable $\zeta(\mathbf{x})$, whose value is conserved on superhorizon scales, to characterize the primordial perturbations in the adiabatic growing mode. We may expand, either using plane wave Fourier modes or a spherical wave expansion, so that

$$\zeta(\mathbf{x}) = \int d^3k \zeta(\mathbf{k}) \exp[i\mathbf{k} \cdot \mathbf{x}] \quad (42)$$

or

$$\zeta(\mathbf{x}) = \sum_{\ell=0}^{\infty} \sum_{m=-\ell}^{+\ell} \int_0^{\infty} dk \zeta_{\ell,m}(k) j_{\ell}(kr) Y_{\ell m}(\theta, \phi). \quad (43)$$

We characterize the homogeneous and isotropic Gaussian statistical ensemble for $\zeta(\mathbf{x})$ by means of a power spectrum $\mathcal{P}(k)$, which suffices to completely define the statistical process generating $\zeta(\mathbf{x})$. We define $\mathcal{P}(k)$ according to the following expectation values:

$$\langle \zeta(\mathbf{k}) \zeta(\mathbf{k}') \rangle = (2\pi)^3 \delta^3(\mathbf{k} - \mathbf{k}') \mathcal{P}(k), \quad (44)$$

or equivalently

$$\langle \zeta_{\ell m}(k) \zeta_{\ell' m'}(k') \rangle = \delta_{\ell, \ell'} \delta_{m, m'} \delta(k - k') \mathcal{P}(k). \quad (45)$$

It follows that

$$a_{\ell m}^{(S),T} = \int_0^{\infty} dk \int_0^{\eta_0} d\eta j_{\ell}(k(\eta_0 - \eta)) \mathcal{S}_T^{(S)}(\eta, k) \zeta_{\ell m}(k), \quad (46)$$

so that

$$C_{\ell}^{(S),TT} = \langle [a_{\ell m}^{(S),T}]^* a_{\ell m}^{(S),T} \rangle = \int_0^{\infty} dk \mathcal{P}(k) \Delta_{\ell}^{(S),T}(k) \Delta_{\ell}^{(S),T}(k), \quad (47)$$

where

$$\Delta_{\ell}^{(S),T}(k) = \int_0^{\eta_0} d\eta j_{\ell}(k(\eta_0 - \eta)) \mathcal{S}_T^{(S)}(\eta, k). \quad (48)$$

The above approach was first implemented in the publicly available code CMBFAST [206] and later in the code CAMB [122].^m More details about the computational issues may be found in these papers.

7.3 Angular diameter distance

The radius of the last scattering surface expressed in terms of co-moving units today (for example in light-years or Mpc) is given by the integral

$$x_{ls} = H_0^{-1} \int_{a_{ls}}^1 \frac{da}{a^2} \frac{1}{\sqrt{\Omega_r a^{-4} + \Omega_m a^{-3} + \Omega_{\Lambda}}} \quad (49)$$

^mFor a download and information on CAMB, see www.camb.info.

for a universe whose stress-energy content includes radiation, matter, and a cosmological constant. Here the scale factor is given by $a_{l_s} = (z_{l_s} + 1)^{-1}$. For other equations of state the argument of the square root above is modified accordingly. A physical scale d at last scattering is converted to a co-moving scale today x according to $x = (z_{l_s} + 1)d$, and under the assumption of a flat spatial geometry, the angle in radians subtended by an arc of length d on the last scattering sphere is $\theta = (d/d_{l_s})$.

Except for the integrated Sachs-Wolfe effect (discussed below in Sec. 7.4), which is very hard to measure because the S/N is negligible but for the very first multipoles, the projection effect described above is the only way in which late-time physics enters into determining the angular power spectrum. Possible spatial curvature, parametrized through Ω_k , the details of a possible quintessence field, or similar new physics that alter the expansion history at late time enters into the CMB power spectra only through a rescaling of the relation between angular scales, on the one hand, and physical scales, on the other, around last scattering, and this rescaling can be encapsulated into a single variable d_{l_s} .

If the family of FLRW solutions extended to admit spatial manifolds of constant positive or negative curvature, the expression for the angular size must be modified to the following for a negatively curved (hyperbolic) universe

$$\theta = \frac{\Omega_k^{1/2} d_{l_s}}{\sinh[\Omega_k^{1/2} d_{l_s}]} \frac{d}{d_{l_s}}, \quad (50)$$

or in the case of positive curvature (i.e., a spherical universe)

$$\theta = \frac{(-\Omega_k)^{1/2} d_{l_s}}{\sin[(-\Omega_k)^{1/2} d_{l_s}]} \frac{d}{d_{l_s}}. \quad (51)$$

In the former case, the additional prefactor giving the contribution for the non-Euclidean character of the geometry has a demagnifying effect and increases the angular diameter distance, whereas for the spherical case the effect is the opposite.

In the early 1990s, many theorists working in early universe cosmology fervently believed on grounds of simplicity in a cosmological model with $\Omega_k = 0$ (supposedly an inexorable prediction of inflation) and no cosmological constant (regarded as extremely finely tuned and “unnatural”) containing only matter and radiation so that $\Omega_r + \Omega_m = 1$ exactly. This belief was maintained despite a number of discordant astronomical observations. Many in the astronomical community, however, rather adopted the attitude “I believe only what I see,” and thus favored some kind of a low-density universe, either a negatively curved universe where $\Omega_k = 1 - \Omega_m - \Omega_r$ or a universe with a nonzero cosmological constant, where $\Omega_\Lambda = 1 - \Omega_m - \Omega_r$.^a

Although it was widely claimed that spatial flatness was a prediction of inflation, the basic idea of how to produce a negatively curved universe within the framework of inflation had already been proposed in 1982 by Gott and Statler [73, 74]. However, since they had not calculated the perturbations predicted in such a model, it was not clear that such a model would work. In 1995 Bucher *et al.* [26, 27] and Yamamoto *et al.* [261] calculated the perturbations for single bubble open inflation, showing them to be consistent with all the observations available at the time. Present constraints from the CMB limit $|\Omega_k - 1|$ to a few percent at most, the exact number depending on the precise parametric model assumed [170, 175].

^aFor a snapshot of the debates in cosmology in the mid-1990s, see the proceedings of the conference *Critical dialogues in cosmology* held in 1995 at Princeton University [222].

7.4 Integrated Sachs-Wolfe effect

The discussion above claimed that the impact of late-time physics on the CMB power spectrum could be completely encapsulated into a single parameter: the angular diameter distance to last scattering d_{ls} . This is only approximately true, because the geometric argument above assumed that all the CMB anisotropy can be localized on the last scattering surface and ignored the integrated Sachs-Wolfe term in Eq. (22), which gives the part of the linearized CMB anisotropy imprinted after last scattering.

Intuitively, the integrated Sachs-Wolfe term can be understood as follows. The Newtonian gravitational potential blueshifts the CMB photons as they fall into potential wells and similarly redshifts them as they again climb out. If the depth of the potential well does not change with time, the two effects cancel. In this case, there is no integrated Sachs-Wolfe contribution because the integral can be reduced to the sum of two surface terms. But if the depth of the potential well changes with time, in particular if the overall scale of the potential is decaying, the two effects no longer cancel and an integrated Sachs-Wolfe contribution is imprinted.

In the linear theory, the gravitational potential at late times may be factorized in the following way:

$$\Phi(\mathbf{x}, t) = \Phi(\mathbf{x})T(t), \quad (52)$$

and we may normalize $T(t)$ to one when the universe has become matter dominated, but before the cosmological constant—or some other dark energy sector—has started to alter the expansion history.

From the CMB anisotropies alone, it is hard to determine the contribution of the integrated Sachs-Wolfe effect to the total CMB anisotropy on large angular scales. However one can try to isolate its contribution by measuring the cross-correlation of the CMB temperature anisotropy with the large-scale structure using a broad radial window function extending to large redshifts as was first proposed in Ref. [37], whose aim was to find evidence for a nonzero cosmological constant.

The evolution equation for the linearized density contrast of a single pressureless matter component is [151]

$$\ddot{\delta}_m(t) + 2H(t)\dot{\delta}_m(t) - \frac{3}{2}H^2(t)\Omega_m(t)\delta_m(t) = 0, \quad (53)$$

where the dots denote derivatives with respect to proper time and $H(t) = \dot{a}(t)/a(t)$. Here we treat the baryons and the CDM (cold dark matter) as a single component ignoring any relative velocity between them. This is not a bad approximation at late times, particularly on very large scales.

For an Einstein-de Sitter universe (for which Ω_r is negligible and $\Omega_\Lambda = 0$), which is a good approximation for our universe at intermediate redshifts, because for $z \lesssim z_{eq} \approx 3.4 \times 10^4$ radiation is unimportant and after the decoupling of the photons and baryons, it is valid to set the velocity of sound equal to zero as above. Let $z_{m\Lambda} = 1/(1 + a_{m\Lambda})$ be the redshift where the nonrelativistic matter and the putative cosmological constant contribute equally to the mean density of the universe, so that $\Omega_m = a_{m\Lambda}^3/(1 + a_{m\Lambda}^3)$ and $\Omega_\Lambda = 1/(1 + a_{m\Lambda}^3)$. For $\Omega_\Lambda = 0.68$, for example, we would have $z_{m\Lambda} = 0.3$ and $a_{m\Lambda} = 0.78$. For the Einstein-de Sitter case, $a(t) = t^{2/3}$ and the growing and decaying solution to Eq. (53) are $t^{2/3}$ and t^{-1} , respectively. $(1/a^2)\nabla^2\phi = (3/2)H^2\Omega_m\delta_m$, and for the growing mode $\Phi(\mathbf{x})$ is independent of

time, implying that there is no integrated Sachs-Wolfe contribution at late times. However, as the cosmological constant begins to take over and Ω_Λ starts to rise toward one, Φ starts to decay, as sketched in Fig. 15.

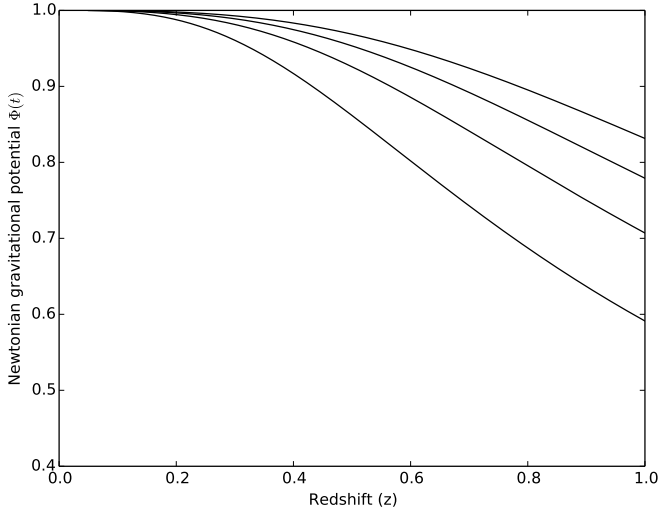


Figure 15: **Decay of gravitational potential for late-time integrated Sachs-Wolfe effect.** We sketch the time dependence of the gravitational potential for a universe with $\Omega_{\Lambda 0} = 0.9, 0.8, 0.7,$ and 0.6 (from top to bottom on the right) with $a = 1$ today. The qualitative behavior will be similar for other kinds of the dark energy.

ing homogeneity and using atomic rate and radiative transfer equations. As a rough estimate, one may assume the reionization fraction predicted by equilibrium thermodynamics given by the Saha equation, in which there is exponential sensitivity to changes in temperature. After $x \approx \frac{1}{2}$, which occurs at about $z \approx 1270$, the ionization fraction $x(z)$ rapidly decays to almost zero, except for trace amounts of ionized hydrogen (denoted as *HII* in the astrophysical literature) and of free electrons, due to the inefficiency of recombination in the presence of trace concentrations. If it were not for inhomogeneities and structure formation, this nearly perfect neutral phase would persist to the present day. However, the initially small primordial inhomogeneities grow and subsequently evolve nonlinearly. The first highly nonlinear gravitationally collapsed regions give rise to the first generation of stars and quasars, which serve as a source of UV radiation that reionizes the neutral hydrogen almost completely, except in a minority of regions of extremely high gas density, where recombination occurs sufficiently frequently to counteract the ionizing flux of UV photons.

The first observational evidence for such nearly complete reionization came from observa-

As explained in detail in Ref. [37], the maximum signal-to-noise (S/N) that can be extracted from the ISW correlation, even with an ideal measurement of the large-scale structure anisotropy within our past light cone, is modest because of the “noise” from the primary CMB anisotropies emanating from the last scattering surface. This cosmic variance noise cuts off the available S/N because on small angular scales, the relative contribution from ISW plummets. The S/N is centered around $\ell \approx 20$ and integrates to about $S/N \approx 6.5$ (assuming $\Omega_{\Lambda 0} = 0.7$). For an early detection of a correlation, see Ref. [25], and for the most recent work in this area see Ref. [172] and references therein.

7.5 Reionization

According to our best current understanding of the ionization history of the universe, the early ionization fraction around recombination is accurately modeled assum-

tions of the spectra of quasars at large redshift in the interval $10.4 \text{ eV}/(1 + z_{\text{quasar}}) < E_\gamma < 10.4 \text{ eV}$ —that is, blueward of the redshifted Lyman α line [75]. If the majority of the hydrogen along the line of sight to the quasar were neutral, resonant Ly α ($2p \rightarrow 1s$) scattering would deflect the photons in this frequency range out of the line of sight, and this part of the spectrum would be devoid of photons. The fact that the spectrum is not completely blocked in this range indicates that the universe along the line of sight was reionized. Almost complete absorption by neutral hydrogen—that is, the so-called Gunn-Peterson trough—was not observed in quasar spectra until 2001, when spectroscopic follow-up of several high-redshift quasars discovered by the Sloan digital sky survey (SDSS) detected such a trough from $z \approx 5.7$ to $z \approx 6.3$, where the continuum emission blueward of the Ly α appears to have been completely absorbed by neutral hydrogen [14].

The big question here is exactly when did the universe first become reionized. Or said another way: When did the first generation of stars and quasars form and become capable of generating enough ionizing radiation to convert the neutral gas to its present ionized state?

This is a vast subject of very current research, sometimes described as the exploration of the “Dark Ages” of the universe. While we believe that we know a lot about the conditions around the time when the CMB anisotropies were imprinted, and we also know a lot about the recent universe extending to moderate redshift, little is known with any degree of certainty concerning this intermediate epoch. Good reviews of this subject include Ref. [12]. Future observations of the 21 cm hyperfine transition of atomic hydrogen (HI) by the next generation of radio telescopes, in particular the Square Kilometer Array (SKA),^o promise to provide three-dimensional maps of the neutral hydrogen in our past light cone.

Here we limit ourselves to discussing the impact of reionization on the CMB anisotropies. The most simplistic model—or caricature—of reionization postulates that the ionization fraction $x(z)$ changes instantaneously from $x = 0$ for $z > z_{\text{reion}}$ to $x = 1$ for $z < z_{\text{reion}}$. Under this assumption, the optical depth for rescattering by the reionized electrons is

$$\tau = \int_0^{z_{\text{reion}}} dz \sigma_T n_e(z) \frac{dl}{dz}. \quad (54)$$

The Thomson scattering optical depth from redshift z to the present day is given by the integral

$$\begin{aligned} \tau(z) &= \frac{c\sigma_T}{H_0} \int_{a(z)}^1 \frac{da}{a} \frac{n_e(a)}{(\Omega_r a^{-4} + \Omega_m a^{-3} + \Omega_\Lambda)^{1/2}} \\ &= \frac{c\sigma_T n_{e0}}{H_0} \int_{a(z)}^1 \frac{da}{a^4} \frac{x_e(a)}{(\Omega_r a^{-4} + \Omega_m a^{-3} + \Omega_\Lambda)^{1/2}}, \end{aligned} \quad (55)$$

where $a(z) = 1/(z + 1)$, σ_T is the Thomson scattering cross-section, H_0 is the present value of the Hubble constant (in units of inverse length), and n_{e0} is the electron density today, assuming $x_e = 1$. The functions $n_e(a)$ and $x_e(a)$ are the electron density^p and the ionization fraction at redshift $z = 1/a - 1$, respectively.

On small angular scales, the effect of reionization on the predicted CMB temperature and polarization anisotropy spectra is straightforward to calculate. Of the CMB photons

^o<https://www.skatelescope.org/>.

^pIt is customary to define x_e as n_e/n_B , so that x_e slightly exceeds one when the helium is completely ionized as well.

emanating from the LSS, a fraction $\exp(-\tau)$ does not undergo rescattering by the reionized electrons and their fractional temperature perturbations are preserved. However, for the remaining fraction $(1 - \exp(-\tau)) \approx \tau$ that is rescattered, the small-angle CMB anisotropies are completely erased. The reionized electrons nearly completely wash out small-scale detail much like a window pane of ground glass. The net effect is that the small-scale CMB anisotropies are attenuated, by a factor of $\exp(-\tau)$ in amplitude and by a factor of $\exp(-2\tau)$ in the power spectrum. On larger angular scales, the attenuation of the anisotropy from the rescattered photon component is incomplete, and a more detailed calculation is needed to determine the detailed form of the ℓ -dependent attenuation factor. The order of magnitude of the angular scale where the attenuation starts to become incomplete is given by the ratio of the co-moving distance travelled from next-to-last to last scattering by a rescattered photon, d_{reion} , to the radius of the LSS d_{LS} . We thus obtain an angular scale $\theta_{\text{reion}} \approx d_{\text{reion}}/d_{\text{LS}}$ for this transition.

For determining the cosmological model from the C_{TT} power spectrum alone, the reionization optical depth is highly degenerate with the overall amplitude of the cosmological perturbations A . This is because except on very large scales, where cosmic variance introduces substantial uncertainty, it is the combination $A \exp(-2\tau)$ that determines the observed amplitude of the CMB angular power spectrum.

The polarization power spectra, meaning C^{EE} and also C^{TE} , help to break this degeneracy by providing a rather model independent measurement of τ_{reion} . Recall our order of magnitude estimate for the polarization introduced by the finite thickness of the LSS

$$P \sim d^2 \frac{\partial^2 T}{\partial x^2}, \quad (56)$$

where d and x are expressed in co-moving units and d is the mean co-moving distance that the photon travels from next-to-last scattering to last scattering. The second derivative is that of the temperature anisotropy evaluated at the position of a typical electron of last scatter. Let us compare the polarization imprinted during recombination to that imprinted later for the fraction of photons $(1 - \exp(-\tau)) \approx \tau$ rescattered by the free electrons from reionization, for the moment assuming that the second derivative factors are comparable for the two cases. However, $d_{\text{rec}} \ll d_{\text{reion}}$; therefore, we may expect that $P_{\text{reion}}/P_{\text{rec}} \approx \tau (d_{\text{rec}}/d_{\text{reion}})^2 \gg 1$. This polarization from reionization, however, is concentrated almost exclusively in the first few multipoles, because directions separated by a small angle see the same quadrupole anisotropy from last scattering from the vantage point of a typical free electron after reionization. Figure 16 shows the scalar power spectra for four values of τ keeping the other cosmological parameters fixed. We shall see that the same amplification applies to the tensor modes, or primordial gravitational waves, presumably generated during inflation.

We now turn to observations allowing us to fix the value of τ using the low ℓ , C^{EE} spectra and C^{TE} spectra based on the qualitative theoretical arguments above but made more precise by calculating τ within the framework of the previously described six-parameter concordance model. While the first observations of the polarization of the CMB were reported by the DASI experiment [110], it was the WMAP large-angle polarization results, first the TE correlations reported in the one-year release, later followed by the EE correlation results from the third-year results, that provided the first determination of τ_{reion} using the CMB, and subsequently refined in later updates to the WMAP results with more integration time. As part of their first-year results [240], the WMAP team reported a value for the reionization optical depth of $\tau = 0.17 \pm 0.04$ at 68% confidence level, which would correspond to $11 < z_r < 30$ at

95% confidence where a step function profile for the ionization fraction is assumed. This determination was based on exploiting only the measurement of the TE cross-correlation power spectrum, because for this first release the analysis of the polarized sky maps was not sufficiently advanced to include a reliable EE auto-correlation power spectrum measurement. The reported value of τ was larger than expected. In their third-year release [246], when WMAP presented a full analysis of the polarization with EE included, the determination of τ shifted downward, namely to $\tau = 0.10 \pm 0.03$ (using only EE data) and $\tau = 0.09 \pm 0.03$ with (TT, TE and EE all included). The final nine-year WMAP release [260] cites a value of $\tau \approx 0.089 \pm 0.014$ using WMAP alone. Including other external data sets results in small shifts about this value.

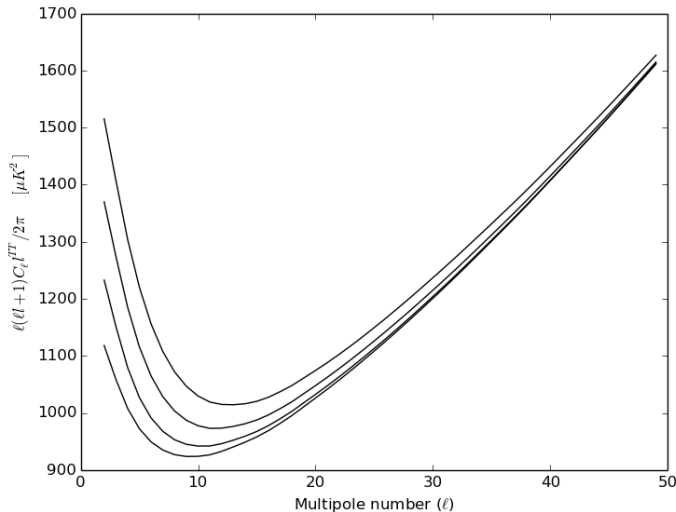


Figure 16: **CMB power spectra for four values of the reionization optical depth.** We plot the indicated power spectra for $\tau = 0.00, 0.04, 0.08$ and 0.12 assuming the same concordance values for the other cosmological parameters. We multiply the spectra by $\exp(2\tau)$ in order to remove the trivial dependence on τ at small angular scales and thus highlight what occurs at low ℓ .

In the above discussion we have assumed that reionization occurs homogeneously in space, an approximation adequate for calculating its effect on the anisotropies at large and intermediate angular scales. However, according to our best understanding, the universe becomes reionized by the formation of bubbles, or Strömgren spheres, surrounding the first sources of ionizing radiation, which grow and become more numerous, and eventually percolate. While this basic picture is highly plausible, the details of modeling exactly how this happens remain speculative. The effect on the CMB is significant only at very small angular scales, far into the damping tail of the primordial anisotropies. Power from the low- ℓ anisotropies is transformed into power at very high ℓ . This can be understood by considering the power in Fourier

The Planck 2013 Results for Cosmology [165, 170, 175] release did not include an analysis of the Planck polarization data. Therefore the likelihoods used to determine the cosmological parameters included the WMAP determination of τ as *a priori*, and in some cases the WMAP low- ℓ polarization likelihood was used in order to break the degeneracy between τ and A described above that arises when only temperature data is used.

It has been pointed out that reionization histories, which are completely characterized by function $x_e(z)$, cannot be reduced to a single number. Some work has been done to characterize what further information can be extracted from the low- ℓ CMB concerning the reionization history, as described in Refs. [93] and [100], but the conclusion is that from the CMB data at most a few nonzero numbers can be extracted at $S/N \gtrsim 1$ given the large cosmic variance at low ℓ .

space resulting from the rather sharp bubble walls, which in projection look almost like jump discontinuities. Some simulations of this effect, along with other effects at large ℓ , can be found for example in Ref. [262].

7.6 What we have not mentioned

The preceding subsections provide a sampling of what can be learned from the CMB TT and polarization power spectra with each point discussed in some detail. For lack of space, we cannot cover all the parameters and extensions of the simple six-parameter concordance model that can be explored, and here we provide a few words regarding what we have not covered giving some general references for more details.

The structure of the acoustic oscillations and the damping tail (relative heights, positions, etc.) of the CMB power spectra depends on the cosmological parameters, as forecast and explained pedagogically in Refs. [90, 97], and most recently applied to the Planck 2013 data for determining the cosmological parameters [170]. Some of the constraints are obtained in the framework of the standard six-parameter concordance model, but many extensions to this model can be constrained, such as theories with varying α_{QED} , nonminimal numbers of neutrinos, varying neutrino masses, isocurvature modes, nonstandard recombination, to name just a few examples. Moreover the question can be addressed whether there exists statistically significant evidence in favor of extending the basic six-parameter model to a model having additional parameters. See Refs. [170] and [175] for an extensive set of references.

8 Gravitational Lensing of the CMB

The previous sections presented a simplified view of the CMB where the CMB anisotropies are imprinted on the so-called last scattering surface, situated around $z \approx 1100$. It is assumed that we look back to this surface along straight line geodesics in the unperturbed coordinate system. This is not a bad approximation, but it is not the whole story. Inhomogeneities in the distribution of matter, particularly at late times when the clustering of matter has become nonlinear, act to curve the photon, or geometric optics, trajectories. These nonuniform deflections distort the appearance of the surface of last scatter, much like a fun house mirror. Gravitational lensing of the CMB is a small effect but large enough so that it has to be taken into account in order to compare models of the primordial universe with the observations correctly. In one sense, gravitational lensing may be viewed as a nuisance effect to be removed. But gravitational lensing of the CMB may also be regarded as an invaluable tool for probing the inhomogeneities of the matter distribution between us and the last scattering surface. Gravitational lensing is presently a very active area of astronomy, and the CMB is only one of the many types of objects whose gravitational lensing may be measured in order to probe the underlying mass inhomogeneities in the universe. Gravitational lensing of the CMB may be contrasted with competing weak lensing probes in that: (i) for the CMB, the sources (i.e., the objects being lensed) are the most distant possible, situated at $z \approx 1100$, (ii) because of the above, CMB lensing is sensitive to clustering at larger redshifts, thus less sensitive to nonlinear corrections, and (iii) unlike observations of the correlations of the observed ellipticities of galaxies, where there are systematic errors due to intrinsic alignments, for CMB lensing there is no such problem.

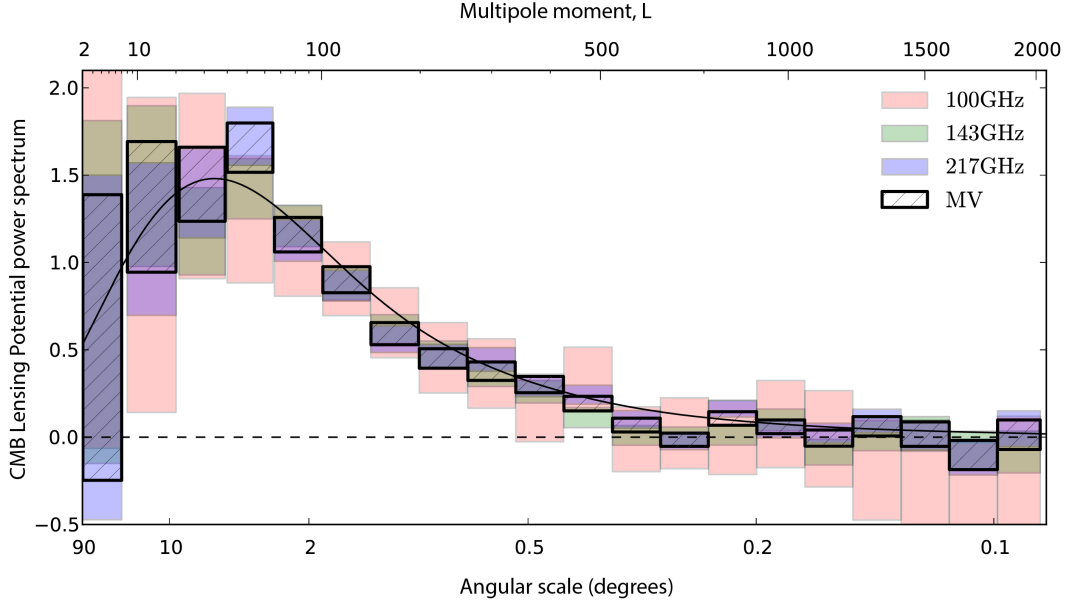


Figure 17: **Power spectrum of CMB gravitational lensing potential as measured by Planck.** The angular power spectrum for the lensing potential as reported in the Planck 2013 results is shown above. The overall statistical significance for a lensing detection is greater than 25σ . The solid curve indicates the expectation based on the concordance model whose six parameters have been fixed by the Planck data combined with ancillary data. For more details, see Ref. [171]. (*Credit: ESA/Planck Collaboration*)

In the linear theory (which is a good approximation, especially for a heuristic discussion), the deflection due to lensing may be described by means of a lensing potential, defined as a function of position $\hat{\Omega}$ on the celestial sphere. Let $\hat{\Omega}_{\text{unlens}}$ coordinatize the last scattering surface as it would look in the absence of lensing, and define $\hat{\Omega}_{\text{lens}}$ to be the position on the last scattering surface with lensing taken into account. We may express

$$\hat{\Omega}_{\text{lens}} = \hat{\Omega}_{\text{unlens}} + \nabla \Phi_{\text{lens}}(\hat{\Omega}). \quad (57)$$

It follows that

$$T_{\text{lens}} = T_{\text{unlens}} - (\nabla \Phi_{\text{lens}}) \cdot (\nabla T_{\text{unlens}}), \quad (58)$$

and similar expressions may be derived for the polarization. As in weak lensing, we may derive a projected Poisson equation for the lensing potential

$$\nabla^2 \Phi_{\text{lens}}(\hat{\Omega}) = \int_0^{x_{\text{source}}} dx W(x; x_{\text{source}}) \delta\rho(\hat{\Omega}, x), \quad (59)$$

where ∇^2 is the Laplacian operator on the sphere. More details about the lensing of the CMB and what can be learned from it may be found in the review [124] and references therein.

The first discovery of gravitational lensing of the CMB involved detecting a statistically significant nonzero cross-correlation between a lensing map reconstructed using the WMAP

data and infrared galaxies [209]. The use of a cross-correlation allows one to detect a small signal within a noisy map. Figure 17 shows the gravitational lensing spectrum as measured by Planck [171]. Measurements of gravitational lensing have also been made by ACT [39] and SPT [223], and the Polarbear experiment has recently reported the discovery of B modes due to lensing [186]. The lensing field described above (which can be expressed either as a potential, as a deflection field, or as a dilatation and shear field) can in principle be recovered from distortions in the small-scale power spectrum due to the lensing field on larger scales. As a general rule, the higher the resolution of the survey, the better the reconstruction. Hu and Okamoto [91, 146] proposed a reconstruction based on Fourier modes, and later many other estimators have been proposed, which are all quite similar because they are all exploiting the same signal. In the future, as observations at higher sensitivity and in particular due to B modes at small scales become available, lensing promises to become a powerful probe of the clustering of matter and halo structure. It is hoped that lensing will eventually be able to determine the absolute neutrino masses, even if they are as low as allowed by present neutrino oscillation data [121]. Lensing detected through B modes is particularly advantageous because the fact that the B modes should be zero in the absence of lensing means that cosmic variance does not intervene and that only the instrument noise is an issue.⁹

9 CMB Statistics

9.1 Gaussianity, non-Gaussianity, and all that

For the simplest models analyzed at linear order, the primordial CMB signal is the outcome of an isotropic Gaussian random process on the celestial sphere. While any particular realization of this random process produces a sky temperature map that is not isotropic, the hypothesis is that the underlying stochastic process is isotropic. Concretely the hypotheses of isotropy and Gaussianity imply that the probability of obtaining a sky map $T(\hat{\Omega})$, whose multipole expansion in terms of spherical harmonic coefficients is given by

$$T(\hat{\Omega}) = \sum_{\ell=0}^{\infty} \sum_{m=-\ell}^{+\ell} a_{\ell m} Y_{\ell m}(\hat{\Omega}), \quad (60)$$

is as follows:

$$P(\{a_{\ell m}\}) = \prod_{\ell=0}^{\infty} \prod_{m=-\ell}^{+\ell} \frac{1}{\sqrt{2\pi C_{\ell}^{th}}} \exp\left[-\frac{1}{2} \frac{|a_{\ell m}|^2}{C_{\ell}^{th}}\right]. \quad (61)$$

Here $\hat{\Omega} = (\theta, \phi)$ denotes a position on the celestial sphere and the set of positive coefficients $\{C_{\ell}^{th}\}$ represents the angular power spectrum of the underlying stochastic process, or the theoretical power spectrum.

If we had postulated Gaussianity alone without the additional hypothesis of isotropy, we would instead have obtained a more general probability distribution function having the form

$$P(\{a_{\ell m}\}) = \det^{-1/2}(2\pi C_{th}) \exp\left[-\frac{1}{2} \sum_{\ell, m} \sum_{\ell', m'} a_{\ell m} {}^*(C_{th})^{-1}_{\ell m, \ell' m'} a_{\ell' m'}\right]. \quad (62)$$

⁹This conclusion hardly depends on r whatever its final value may turn out to be, because the angular scales best for probing lensing lie beyond the recombination bump of the B modes.

Here C_{th} is the covariance matrix for the spherical harmonic multipole coefficients. This Ansatz is too general to be useful because there are many more parameters than observables, and in cosmology we can observe only a single sky—or said another way, only a single realization of the stochastic process defined in Eq. (62). The assumption of isotropy is very strong, greatly restricting the number of degrees of freedom by setting all the off-diagonal elements to zero and requiring that the diagonal elements depend only on ℓ .

Happily, the present data, subject to some caveats (such as gravitational lensing, discussed above in Sec. 8), seem consistent with the hypotheses of isotropy and Gaussianity, notwithstanding some “anomalies” at moderate statistical significance (discussed in detail below in Sec. 12). These anomalies could be a sign of something new, but given their limited statistical significance, the argument that they are simply statistical “flukes” cannot be rejected.

For completeness, we now indicate how the above formalism is extended to include the polarization of the primordial CMB signal. There are several formalisms for describing the polarization of the CMB, for example, using spin-weighted spherical harmonics, or using the Stokes parameters I , Q , U , V [23]. (The polarization of the CMB and its description are discussed in Refs. 35, 96, and 108) We may define $T_{ab}(\hat{\Omega}) = \langle \mathcal{E}_a(\hat{\Omega})^* \mathcal{E}_b(\hat{\Omega}) \rangle_{\text{time}}$ where $\mathcal{E}_a(\hat{\Omega})$ is the electromagnetic field component propagating from the direction $\hat{\Omega}$ and units are chosen so that for a unit electric polarization vector $\boldsymbol{\varepsilon}$, and $T_{ab}(\hat{\Omega})\varepsilon_a\varepsilon_b$ represents the CMB thermodynamic temperature when by means of a linear polarizer only the component along $\boldsymbol{\varepsilon}$ is measured. We may decompose

$$T_{ab}(\hat{\Omega}) = T(\hat{\Omega})\delta_{ab} + P_{ab}(\hat{\Omega}), \quad (63)$$

where the polarization tensor (containing the Stokes parameters Q , U and V) is trace-free and Hermitian (and also symmetric in the absence of circular polarization).

We must now choose a convenient basis for the polarization. If we considered a single point on the celestial sphere, we could use Stokes parameters set $Q = T_{11} - T_{22}$ and $U = 2T_{12}$, but no natural choice for the directions orthonormal unit vectors \hat{e}_1 and \hat{e}_2 in the tangent space at $\hat{\Omega}$ can be singled out as preferred. Had we instead chosen

$$\begin{pmatrix} \hat{e}'_1 \\ \hat{e}'_2 \end{pmatrix} = \begin{pmatrix} \cos \theta & \sin \theta \\ -\sin \theta & \cos \theta \end{pmatrix} \begin{pmatrix} \hat{e}_1 \\ \hat{e}_2 \end{pmatrix}, \quad (64)$$

we would instead have the Stokes parameters

$$\begin{pmatrix} Q' \\ U' \end{pmatrix} = \begin{pmatrix} \cos 2\theta & \sin 2\theta \\ -\sin 2\theta & \cos 2\theta \end{pmatrix} \begin{pmatrix} Q \\ U \end{pmatrix}. \quad (65)$$

The transformation law in Eq. (65) indicates that the traceless part of the polarization is of spin-2. If the sky were flat with the geometry of R^2 instead of S^2 and we had to include homogeneous modes as well, there would be no way out of this quandary. But there is a celebrated result of differential geometry that a fur on a sphere of even dimension cannot be combed without somewhere leaving a bald spot or singularity.^f A traceless tensor field on the sphere cannot have an everywhere vanishing covariant derivative.

^fThis is a consequence of the “hairy ball” theorem [60].

We can generate a complete basis for the polarization on the celestial sphere by means of derivative operators acting on the spherical harmonics. Using $Y_{\ell m}(\hat{\Omega})$ as a starting point, we may define an E mode basis vector as follows:

$$E_{ab;\ell m}(\hat{\Omega}) = N_{\ell}^{E,B} \left(\nabla_a \nabla_b - \frac{1}{2} \delta_{ab} \nabla^2 \right) Y_{\ell m}(\hat{\Omega}), \quad (66)$$

where $N_{\ell}^{E,B}$ is a normalization factor. Here $a, b = 1, 2$ indicate components with respect to an arbitrary orthonormal basis on S^2 . Without introducing more structure, this is the only way to produce a second-rank traceless tensor on the sphere with derivative operators acting on $Y_{\ell m}(\hat{\Omega})$ in a way that does not break isotropy, a feature that ensures that $E_{ab;\ell m}(\hat{\Omega})$ transforms under rotations according to the quantum numbers ℓm . However, there is another polarization, rotated with respect to the E mode by 45° , and in order to write down a basis for this other polarization, known as the B modes, it is necessary to introduce an orientation on the sphere through the unit antisymmetric tensor $\epsilon_{12} = 1$. This choice of orientation, or volume element in the language of differential geometry, defines a handedness, or direction in which the 45° rotation is made.

We may define

$$B_{ab} = \frac{1}{2} (\delta_{aa'} + \epsilon_{aa'}) (\delta_{bb'} + \epsilon_{bb'}) E_{a'b'}, \quad (67)$$

or in terms of derivative operators

$$B_{ab} = \frac{1}{2} N_{\ell}^{E,B} (\epsilon_{ac} \delta_{bd} + \epsilon_{bc} \delta_{ad}) \nabla_c \nabla_d Y_{\ell m}(\hat{\Omega}). \quad (68)$$

The difference between E modes and B modes is illustrated in Fig. 18. We want to normalize so that

$$\int d\hat{\Omega} E_{ab,\ell m}(\hat{\Omega}) E_{ab,\ell' m'}^*(\hat{\Omega}) = \int d\hat{\Omega} B_{ab,\ell m}(\hat{\Omega}) B_{ab,\ell' m'}^*(\hat{\Omega}) = \delta_{\ell,\ell'} \delta_{m,m'} \quad (69)$$

and

$$\int d\hat{\Omega} E_{ab,\ell m}(\hat{\Omega}) B_{ab,\ell' m'}^*(\hat{\Omega}) = 0, \quad (70)$$

so we require that [99]

$$N_{\ell}^{E,B} = \sqrt{\frac{2}{(\ell+2)(\ell+1)\ell(\ell-1)}}. \quad (71)$$

Although the above discussion emphasized the role of spherical harmonics, the distinction between E and B modes does not rely on spherical harmonics, and much confusion has resulted from not fully appreciating this point. The absence of an E mode component or a B mode component may be formulated in a completely local manner using covariant derivative operators acting on the polarization tensor $P_{ab}(\hat{\Omega})$. If $\nabla_a P_{ab} = 0$, then the E mode is absent, and similarly if $\epsilon_{ab} \nabla_a P_{bc} = 0$, then the B mode is absent. Consequently, if we are willing to differentiate the data, we could detect B modes locally with absolutely no leakage. However,

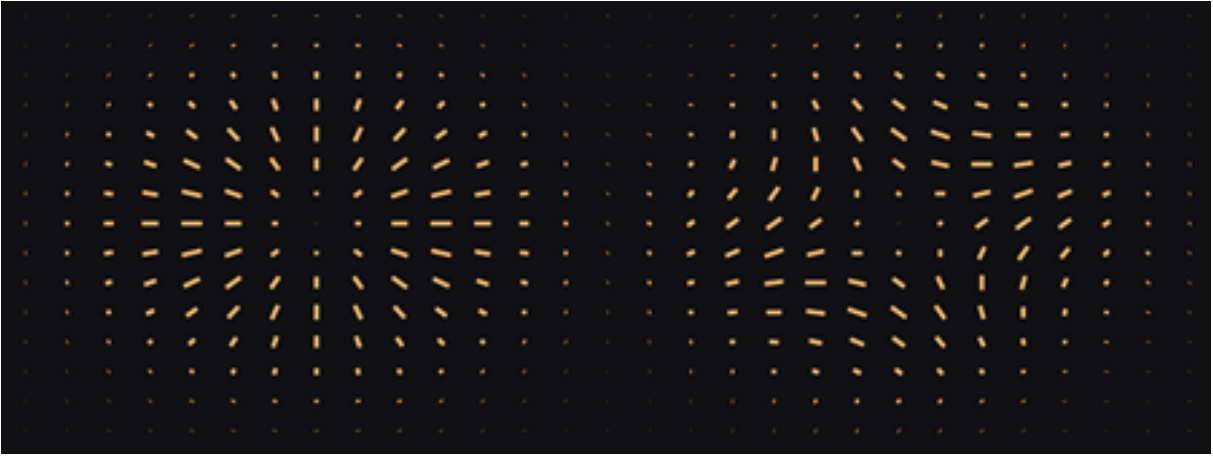


Figure 18: **E and B modes of the CMB polarization.** The polarization pattern in the left panel can be expressed as the double derivative acting on a potential with its trace removed (in this case a Gaussian potential) and thus is an E mode. The B mode pattern on the right, however, cannot be represented in this way, but can be represented by a pseudo-scalar potential whose double derivative with the trace removed followed by a 45° rotation gives the indicated pattern.

the above does not imply that a unique decomposition of P_{ab} into E and B on an incomplete sky is possible because nonsingular vector fields (akin to harmonic functions) can be found that satisfy both conditions, although no nontrivial such vector fields exist defined on the full sky. Where global topology does enter is in eliminating configurations that satisfy both the above differential constraints.

Having defined the E and B modes, we now indicate how the statistical distribution defined in Eq. (61) is modified to include polarization. We modify our notation somewhat to avoid unnecessary clutter. When polarization is included, our vector $\{a_{\ell m}^T\}$ is generalized to become $\{a_{\ell m}^T, a_{\ell m}^E, a_{\ell m}^B\}$, which we shall denote as the vector $(\mathbf{t}, \mathbf{e}, \mathbf{b})$. For each ℓ we have a positive definite covariance matrix of the form

$$\mathbf{C}_\ell = \begin{pmatrix} C_\ell^{\text{TT}} & C_\ell^{\text{TE}} & C_\ell^{\text{TB}} \\ C_\ell^{\text{ET}} & C_\ell^{\text{EE}} & C_\ell^{\text{EB}} \\ C_\ell^{\text{BT}} & C_\ell^{\text{BE}} & C_\ell^{\text{BB}} \end{pmatrix}. \quad (72)$$

If we assume that the underlying physics imprinting the cosmological perturbations is invariant under spatial inversion, then the above covariance matrix simplifies to

$$\mathbf{C}_\ell = \begin{pmatrix} C_\ell^{\text{TT}} & C_\ell^{\text{TE}} & 0 \\ C_\ell^{\text{ET}} & C_\ell^{\text{EE}} & 0 \\ 0 & 0 & C_\ell^{\text{BB}} \end{pmatrix}, \quad (73)$$

because under spatial inversion

$$C_\ell^{\text{TB}} \rightarrow -C_\ell^{\text{TB}}, \quad C_\ell^{\text{EB}} \rightarrow -C_\ell^{\text{EB}}, \quad (74)$$

whereas the other power spectra coefficients preserve their sign.

If parity is a symmetry of the physical processes generating the primordial perturbations and imprinting the CMB anisotropies, the expectation values $C_\ell^{\text{TB},th}$ and $C_\ell^{\text{EB},th}$ must vanish, although for any particular sky realization $C_\ell^{\text{TB},obs}$ and $C_\ell^{\text{EB},obs}$ will not vanish because of cosmic variance. (Recall that $C_\ell^{\text{TB},th}$ and $C_\ell^{\text{EB},th}$ is the average over a fictitious ensemble including an infinite number of sky realizations.) Studying $C_\ell^{\text{TB},obs}$ and $C_\ell^{\text{EB},obs}$ to search for statistically significant deviations from zero is a way to search for parity violation in the very early universe. However, in practice adjusting experimental parameters to minimize $C_\ell^{\text{TB},obs}$ and $C_\ell^{\text{EB},obs}$ is often used to calibrate detector angles in B mode polarization experiments.

The propagation of light, or electromagnetic radiation, at least historically and conceptually, occupies a privileged place in the theories of special and general relativity, because of the constancy of the speed of light in vacuum and the fact that at least in the eikonal approximation, light travels along null geodesics, with its electric polarization vector propagated along by parallel transport. It is by thinking of bundles of light rays that we construct for ourselves a physical picture of the causal structure of spacetime. A modification of the propagation of light (for example, from dilaton and axion couplings [144], a possible birefringence of spacetime [63, 212, 101, 32], or alternative theories of electromagnetism [71, 72, 145]) would not necessarily undermine the foundations of relativity theory, but would probably merely lead to a more complicated theory, possibly only in the electromagnetic sector. The CMB may be considered an extreme environment because of the exceptionally long travel time of the photons, and one can search for new effects beyond the known interactions with matter (e.g., Thomson and other scattering, collective plasma effects such as dispersion and Faraday rotation). Some such effects would lead to spectral distortions, for example through missing photons. The rotation of the polarization vector during this long journey would lead to mixing of E and B modes, and since the primordial E modes are so much larger, leads to interesting constraints on birefringence, which will greatly improve as more data comes in from searches for primordial B modes.

The statistical description in Eqs. (72) and (73) suffice for confronting the predictions of theory with idealized measurements of the microwave sky with complete sky coverage and no instrument noise. We must further assume that there are no secondary anisotropies, nor galactic foregrounds, both of which have been perfectly removed.

Even under these idealized assumptions, it is not possible to pin down the theory completely because of a phenomenon known as cosmic variance. The problem is that while we would like to characterize the covariance of the underlying theory $C_\ell^{\text{AB},th}$ (where A,B = T,E,B), we have only a single realization of the microwave sky, and $C_\ell^{\text{AB},obs}$ is only an estimate of $C_\ell^{\text{AB},th}$ with fluctuations about its expectation value which is equal to $C_\ell^{\text{AB},th}$. If we consider just the temperature fluctuations, we may define the sample variance for the ℓ th multipole

$$C_\ell^{\text{TT},obs} = \frac{1}{(2\ell + 1)} \sum_{m=-\ell}^{+\ell} |a_{\ell m}|^2. \quad (75)$$

The random variable $C_\ell^{\text{TT},obs}$ obeys a χ^2 -distribution with $(2\ell + 1)$ degrees of freedom and thus has fractional variance of $\sqrt{2/(2\ell + 1)}$. If we consider a microwave sky map bandlimited up to ℓ_{max} , there are approximately ℓ_{max}^2 degrees of freedom, so for example the overall amplitude of

the cosmological perturbations may be determined with a fractional accuracy of approximately $1/\ell_{\max}$.

Most analyses of the CMB data (possibly combined with other data sets) assume a model where the theoretical power spectrum depends on a number of cosmological parameters, which we may abstractly denote as $\alpha_1, \alpha_2, \dots, \alpha_D$, also written more compactly as the vector $\boldsymbol{\alpha}$. For example, in the six-parameter minimal cosmological model claimed sufficient in the 2013 Planck Analysis [170] to explain the present data, the parameters comprising this vector were $A_S, n_s, H_0, \omega_b, \omega_{\text{CDM}}$ and τ .

Whether one adopts a frequentist or Bayesian analysis to analyze the data, the input is always the relative likelihood of the competing models given the observations, or a ratio of the form:

$$\frac{P(\text{observations} \mid \boldsymbol{\alpha}_1)}{P(\text{observations} \mid \boldsymbol{\alpha}_2)}. \quad (76)$$

In this ratio, the measure for the probability density of the outcome, represented by a continuous variable, cancels.

In this abridged discussion, we shall follow a Bayesian analysis where *a priori* probability $P_{\text{prior}}(\boldsymbol{\alpha})$ is assumed on the space of models. In Bayesian statistics, Bayes' theorem is used to tell us how we should rationally update our prior beliefs (or prejudices) in light of the data or observations, to yield a posterior probability to characterize our updated beliefs given by the formula

$$P_{\text{posterior}}(\boldsymbol{\alpha}) = \frac{P(\text{observations} \mid \boldsymbol{\alpha})P_{\text{prior}}(\boldsymbol{\alpha})}{\int d^D \boldsymbol{\alpha}' P(\text{observations} \mid \boldsymbol{\alpha}')P_{\text{prior}}(\boldsymbol{\alpha}')}. \quad (77)$$

There is no reason why the posterior distribution should lend itself to a simple analytic form, and a common procedure is to explore the form of the posterior distribution using Markov Chain Monte Carlo (MCMC) methods [123, 57], which are particularly well suited to explore distributions of large dimensionality.

However, it often occurs that the likelihood and the posterior distribution can be adequately represented as a Gaussian by expanding about its maximum likelihood value. In this case, the maximum of the log of the probability can be found using a numerical optimization routine, and then by computing second derivatives using numerical finite differences, the Gaussian approximation to the posterior can be found. This infinitesimal analysis is often referred to as a Fisher analysis.

9.2 Non-Gaussian alternatives

It is incredibly difficult to test the Gaussianity of the primordial microwave sky without some guidance from theory as to what non-Gaussian alternatives are well motivated. The space of non-Gaussian stochastic models is dauntingly vast, with the space of Gaussian models occupying by any measure an almost negligible fraction of the model space. If one tests enough models, one is guaranteed to produce a result beyond any given threshold of significance. Consequently, one of the questions lurking behind any claim of a detection of non-Gaussianity is how many similar models did one test.

10 Bispectral Non-Gaussianity

Although it was recognized that inflation, in its simplest form described by Einstein gravity and a scalar field minimally coupled to gravity, would have some nonlinear corrections, early analyses of the cosmological perturbations generated by inflation linearized about a homogeneous solution and calculated the perturbations in the framework of a linearized (free) field theory. According to the lore at the time, the nonlinear corrections to this approximation would be too small to be observed. The first calculations of the leading nonlinear corrections were given by Maldacena [131] and Aquaviva *et al.* [4], who calculated the bispectrum or three-point correlations of the primordial cosmological perturbations within the framework of single-field inflation.

Subsequent work indicated that in models of multi-field inflation, bispectral non-Gaussianity of an amplitude much larger than for the minimal single-field inflationary models can be obtained. The predictions of many of these multi-field models were within the range that would be detectable by the Planck satellite. For many of these models, the non-Gaussianity, owing to the fact that it is generated by dynamics on superhorizon scales where derivative terms are unimportant, is well described by the “local” Ansatz for bispectral non-Gaussianity, under which the non-Gaussian field ζ_{NL} is generated from an underlying Gaussian field ζ_L according to the rule

$$\zeta_{NL}(\mathbf{x}) = \zeta_L(\mathbf{x}) + [\zeta_L(\mathbf{x})]^2, \quad (78)$$

where f_{NL} is a dimensionless parameter that quantifies the degree of non-Gaussianity.

Here f_{NL} is independent of wavenumber, but a dependence on wavenumber can also be contemplated, so that the above relation is generalized to the following (now working in wavenumber space):

$$\zeta_{NL}(\mathbf{k}) = \int d^3k_1 \int d^3k_2 f_{NL}(k; k_1; k_2) \delta^3(\mathbf{k} - \mathbf{k}_1 - \mathbf{k}_2) \zeta_L(\mathbf{k}_1) \zeta_L(\mathbf{k}_2). \quad (79)$$

Here as a consequence of the hypothesis of isotropy, we have expressed f_{NL} as a function depending only on the lengths of the vectors. Any two triangles (where the three vectors close) that may be mapped into each other by an isometry are assigned the same f_{NL} .

For bispectral non-Gaussianity of the *local* form, as defined in Eq. (78), we briefly sketch how the order of magnitude of $(S/N)^2$ for a detection of f_{NL} from a CMB map extending up to ℓ_{\max} may be estimated. We simplify the estimate by employing the flat sky approximation, allowing us to replace the unintuitive discrete sums and Wigner $3j$ symbols with more the transparent continuum integrals and a two-dimensional δ -function. Approximating $C_\ell \approx C_0 \ell^{-2}$ (in other words, we ignore acoustic oscillations, damping tails, and all that) and assuming that the CMB is scale invariant on the sky, as would occur if one could extrapolate the simplified Sachs-Wolfe formula $(\Delta T)/T = -\Phi/3$ to arbitrarily small scales), we may write

$$\begin{aligned} \left(\frac{S}{N}\right)^2 &= O(1) \int \frac{d^2\ell}{(2\pi)^2} \int \frac{d^2\ell_2}{(2\pi)^2} \int \frac{d^2\ell_3}{(2\pi)^2} (2\pi)^2 \delta^2(\ell_1 + \ell_2 + \ell_3) \\ &\times \frac{f_{NL}^2 C_0^4 (\ell_1^{-2} \ell_2^{-2} + \ell_2^{-2} \ell_3^{-2} + \ell_3^{-2} \ell_1^{-2})^2}{C_0^3 \ell_1^{-2} \ell_2^{-2} \ell_3^{-2}} \\ &= O(1) (f_{NL})^2 C_0 \ell_{\max}^2 \ln \left(\frac{\ell_{\max}}{\ell_{\min}} \right). \end{aligned} \quad (80)$$

The quantity in the first line simply approximates the sum over distinguishable triangles, the combinatorial factors being absorbed in the $O(1)$ factor, and the second line gives the signal-to-noise squared of an individual triangle, as calculated diagrammatically. More exact calculations taking into account more details confirm this order of magnitude estimate. Numerical calculations are needed to determine the $O(1)$ factor and deal with ℓ_{\max} more carefully. Nevertheless this rough estimate reveals several characteristics of local non-Gaussianity, namely: (i) the presence of the $\ln(\ell_{\max}/\ell_{\min})$ factor indicates that the bulk of the signal arises from the coupling of large angle modes and small angle modes (i.e., the modulation of the smallest scale power, near the resolution limit of the survey, by the very large angle modes (i.e., $\ell = 2, 3, \dots$), and (ii) the cosmic variance of the estimator derives from the inability to measure the small-scale power accurately, and thus decreases in proportion to the effective number of resolution elements of the survey. Cosmic variance on large scales is not an issue. As long as we know the particular realization on large scales accurately (which is not subject to cosmic variance), we know what kind of modulation to look for in the small-scale anisotropies.

Theoretical models for other shapes for the bispectral anisotropy can be motivated by models for fundamental physics (see for example Refs. [9] and [107] and references therein) and have been searched for as well. The Planck 2013 Results gave the following limits [177]: $f_{NL}^{\text{local}} = 2.7 \pm 5.8$, $f_{NL}^{\text{equil}} = -42 \pm 75$, and $f_{NL}^{\text{ortho}} = -25 \pm 39$. This result rules out many of the models developed to explain a result at low statistical significance from some analyses of the WMAP data and was a profound disappointment to those who hoped that Planck would turn up striking evidence against the simplest inflationary models. One may anticipate that the results from Planck 2014 will improve modestly on the 2013 results by including more modes because of the use of polarization. If there is a next-generation all-sky CMB polarization satellite having good angular resolution so that $S/N \approx 1$ maps may be obtained up to $\ell_{\max} \approx 3000$, an improvement on the limits on f_{NL} by a factor of a few may be envisaged. However, beyond $\ell \approx 3000$, the primary CMB anisotropies become a sideshow. As one pushes upward in ℓ , other nonprimordial sources of anisotropy take over, such as gravitational lensing, the Sunyaev-Zeldovich effect, and point sources of various sorts. These contaminants have angular power spectra that rise steeply with ℓ while the CMB damping tail is falling rapidly, in fact almost exponentially. For including more modes, polarization may be helpful. On the one hand, polarization measurements present formidable instrumental challenges because of their lower amplitude compared to the temperature anisotropies. However, for the polarization, the ratio of foregrounds to the primordial CMB signal is favorable up to higher ℓ than for temperature. For searching for non-Gaussianity, the primordial CMB is highly linear, unlike other tracers of the primordial cosmological perturbations. However given that the basic observables are two-dimensional maps, the small number of modes compared to three-dimensional tracers of the primordial perturbations is a handicap.

11 B Modes: A New Probe of Inflation

As discussed above, some limits on the possible contribution from tensor modes, or primordial gravitational waves, can be obtained from analyzing the C^{TT} power spectrum. However, given that r is not large, these limits become highly model dependent, and because of cosmic variance as well as uncertainty as to the correct parametric model, cannot be improved to any substantial extent. This difficulty is illustrated by the results from the Planck 2013

analysis [175], which did not include the data on polarized anisotropies collected by Planck but only the TT power spectrum. If one assumes the minimal six-parameter model plus r added as an extra parameter, a limit of $r < 0.11$ (95% C.L.) is obtained. However, if the primordial power spectrum in this model (where a form $P(k) \sim k^{n_s-1}$ is assumed) is generalized to $P(k) \sim (k/k^*)^{n_s-1} \exp(\alpha(\ln(k/k^*))^2)$, the limits on r loosen by about a factor of two to become $r < 0.2$ (95% confidence level). This lack of robustness to the assumptions of the parametric model highlights the fragility of this approach and demonstrates that the statistical error bars are not to be trusted unless one has strong reason to trust the underlying parametric model. However, given our current understanding of inflationary potentials and dynamics, we have no reason to trust any of the parametric models, which serve more as fitting functions for summarizing the current state of the observations.

Searching for tensor modes using B modes, on the other hand, allows us to probe much lower values of r in a manner that is substantially model independent because in the linear theory “scalar” perturbations cannot generate any B modes, and this conclusion is independent of the parametric model assumed.

11.1 Suborbital searches for primordial B modes

In March 2014, the BICEP2 Collaboration [17, 18] claimed a detection of primordial gravitational waves based primarily on observations at a single frequency (150 GHz) over a small patch of the sky (1% of the sky) that was believed to be of particularly low polarized dust emission. Using a telescope based at the South Pole, the BICEP2 team created a map at 150 GHz of the polarized sky emission from which the B mode contribution was extracted. The BICEP2 analysis included many null tests to estimate and exclude systematic errors as well as to estimate the statistical noise in the measurement. However, in order to claim a detection of primordial gravitational waves, the BICEP2 team had to exclude a nonprimordial origin for the observed B mode signal, for which the main suspect would be polarized thermal dust emission. An independent analysis [67] called into question the BICEP2 estimate of the likely dust contribution in their field, claiming that all the observed signal could be attributed to dust. A subsequent Planck analysis estimating the dust contribution in the BICEP2 field by extrapolating polarized dust maps at higher frequencies where dust is dominant down to 150 GHz confirmed this finding [163]. While this analysis does not necessarily exclude a nonzero primordial contribution to the B modes observed by BICEP2 at 150 GHz, the argument crucial to the BICEP2 claim that a dominant contribution from dust can be excluded collapses in light of this new finding from Planck concerning the expected contribution from thermal dust emission. A cross-correlation study is now underway as a joint project of the two teams that will combine the BICEP2 map at 150 GHz with the Planck polarization maps higher frequencies (which are dominated by dust). It remains to be seen whether this effort can establish a limit on r better than what is currently available or whether this combined analysis might even result in a detection of primordial B modes albeit at a lower level of r .

In any case, a number of experiments are now underway involving observations at multiple frequencies that will push down the limits on r using B modes if not result in a first detection if r is not too small. The BICEP2 team has a series of upgrades to their experiment expanding their frequency coverage as well as massively increasing the number of detectors and hence their sensitivity. Other competing efforts include POLARBEAR [8], SPIDER [34] and QUBIC [13], as well as ACTPol and SPTPol.

Moreover, farther into the future, a more ambitious upgrade to ground based efforts is contemplated through the US Stage 4 (S4) [1, 2] CMB experiment currently under consideration by the US DOE. S4 contemplates deploying approximately a total of 2×10^5 detectors from the ground in order to achieve a massive improvement in raw sensitivity. Although it is claimed that an improvement in the control of systematic errors to a comparable level can be achieved, it remains to be seen whether S4 can realize its projected performance.

11.2 Space based searches for primordial B modes

Several groups around the world have proposed space missions specifically dedicated to mapping the microwave polarization over the full sky with a sensitivity that would permit the near ultimate measurement of the CMB B modes. In Europe, three ESA missions had been proposed: BPol in 2007 [43], COre [33] in 2010, both of which were medium-class, and the large-class mission PRISM [189] in 2013. None of these missions was selected. A mission proposal called COre+ is currently in the process of being submitted. In Japan a mission called LiteBird [84] has been developed, but final approval is still pending. In the US, CMBPol/EPIC [61] has proposed a number of options for a dedicated CMB polarization space mission,^s but none of these has been successful in securing funding. All the above concepts involve a focal plane including several thousand single-mode detectors in order to achieve the required sensitivity. Another proposal endeavors to achieve the needed sensitivity by another means: multi-moded detectors. In the Pixie [105] proposal, a Martin-Pupplet Fourier spectrometer comparing the sky signal to that of an artificial blackbody is proposed. The setup is similar to the COBE FIRAS instrument, except that polarization sensitive bolometers and a more modern technology are used, which will allow an improvement in the measurement of the absolute spectrum about two orders of magnitude better than FIRAS.

12 CMB Anomalies

The story recounted so far has emphasized the agreement of the observations accumulated over the years with the six-parameter so-called “concordance” model. But this would not be a fair and accurate account without reporting a few wrinkles to this remarkable success story. These wrinkles may either be taken as hints of new physics, or discounted as statistical flukes, perhaps using the pejorative term *a posteriori* statistics. On the one hand, one can argue that if one looks at enough models that are in some sense independent, one is bound to turn up something at high statistical significance, and by most standards the significance of these anomalies is not high. Which interpretation is preferred is presently under debate. Ultimately, despite all the fancy statistical terminology used in this discourse, what one concludes inevitably relies on a subjective judgment of theoretical plausibility.

One anomaly explored over the years, known under several names including “hemispherical asymmetry,” “dipolar modulation,” and “bipolar disorder,” asks the question whether the local angular power spectrum is identical when compared between opposite directions on the celestial sphere. There is no unique way to pose this question precisely. The statistical significance, amplitude, and direction of the asymmetry depend somewhat on the precise formulation chosen. However, the WMAP finding of a dipolar modulation with an amplitude

^sSee <http://cmbpol.uchicago.edu/papers.php> for a list of papers on this effort.

of $\approx 7\%$ and a significance ranging within about $2 - 4\sigma$, and pointing approximately toward $(l, b) = (237^\circ, 20^\circ)$ in galactic coordinates is broadly confirmed by the Planck 2013 Results. This confirmation by Planck, owing to the additional high frequency coverage, renders less plausible a nonprimordial explanation based on foreground residuals. The sensitivity to dipolar modulation on these angular scales is primarily limited by cosmic variance for both WMAP and Planck, so future experiments cannot hope to improve substantially on the significance of these results. Planck, however, because of its superior angular resolution, was able to probe for dipolar modulation pushing to smaller scales, where cosmic variance is less of a problem and a possible modulation can be constrained more tightly. [The measurement uncertainty in the scale-dependent dipole modulation of the amplitude of the perturbations $\Delta A(\ell)$ (assuming broad binning) scales as $1/\ell$ as long as cosmic variance is the limiting factor.] The Planck 2013 data find no evidence of dipolar modulation at the same amplitude extending to small angular scales, suggesting that if the dipolar modulation observed by WMAP is not a statistical fluke, a scale-dependent theoretical mechanism for dipolar modulation is needed. Moreover, Planck does not see evidence of modulation associated with higher multipoles (e.g. quadrupolar and higher order disorders). This last point is important for constraining theoretical models producing statistical anisotropy by means of extra fields disordered during inflation.

Another anomaly is the so-called “cold spot.” Rather than limiting ourselves to two-point statistics, or to three-point statistics, searching for a bispectral signal using theoretically motivated templates, as described in Sec. 10, we may ask whether the most extreme values of an appropriately filtered pure CMB map lie within the range that may be expected assuming an isotropic Gaussian stochastic process, or whether their p -values (i.e., probability to exceed) render the Gaussian explanation implausible. There are many ways to formulate questions of this sort, a fact that renders the assessment of statistical significance difficult. One approach that has been applied to the data is to filter the sky maps with a spherical Mexican hat wavelet (SMHW) filter, which on the sphere would have the profile of the Laplacian operator applied to a Gaussian kernel of a given width σ , giving a broad [i.e., $(\Delta\ell)/\ell = O(1)$] two-dimensional spatial bandpass filter. (See Ref. [224] for more details concerning the methodology and Ref. [225] for the original claim of a cold spot detection. See also Ref. [257] for an assessment by the WMAP team as well as Ref. [176] for the analysis from Planck 2013.)

The final anomaly concerns possible alignments of the low- ℓ multipoles, imaginatively named the “axis of evil” by Land and Magueijo [114]. A Gaussian isotropic theory for the temperature anisotropy^t predicts that the multipole vectors $\mathbf{a}_\ell = \{A_{\ell m}\}_{m=-\ell}^{+\ell}$ are each Gaussian and independently distributed. If we add three or more such vectors together according to the tensor product of representations of $SO(3)$

$$L_1 \otimes L_2 \otimes \cdots \otimes L_N, \tag{81}$$

which may be decomposed into a direct sum of irreducible representations. Provided that the triangle inequality is satisfied, we may extract one or more scalars (transforming according to $L = 0$) from the above tensor product. The mathematics is simply that of the usual addition of angular momentum. For each of these scalars, we may ask whether the observed value lies within the range expected from cosmic variance in the framework of a Gaussian theory taking into account the uncertainty in the determination of the underlying power

^tThe discussion can readily be generalized to polarization, but we shall stick to the temperature anisotropy alone in our discussion.

spectrum. The approach just described was not the approach of Land and Magueijo, who maximized $\max_{m \in [-\ell, +\ell]} |a_{\ell m}(\hat{\mathbf{n}})|$ as a function of $\hat{\mathbf{n}}$ where $a_{\ell m}(\hat{\mathbf{n}})$ is the expansion coefficient in the coordinate system with $\hat{\mathbf{n}}$ pointing to the north pole. In this way, for each generic value of the multipole number ℓ a unique double headed vector, or axis, $\pm \hat{\mathbf{n}}$ may be extracted, and the alignments between these axes may be assessed. Land and Magueijo report an alignment of the $\ell = 3$, $\ell = 4$, and $\ell = 5$ axes with a p -value less than 10^{-3} in the Gaussian theory. Accurate p values may be obtained for each of these invariant quantities by resorting to MC simulations to account for the practicalities of dealing with a cut sky, etc. However, there still remains a subjective element to assessing statistical significance. One may ask how many invariants were tried before arriving at a reportable statistically significant anomaly.

13 Sunyaev-Zeldovich Effects

In the simplified discussion of reionization presented in Sec. 7.5, it was assumed that the electrons responsible for the rescattering are at rest with respect to the cosmic rest frame. This approximation treats the reionized gas as a cold plasma having a vanishing peculiar velocity field. As pointed out by Sunyaev and Zeldovich [215], corrections to this approximation arise in two ways: (i) In the so-called thermal Sunyaev-Zeldovich effect (tSZ), the random thermal motions of the free electrons alter the spectrum of the rescattered CMB photons through the Doppler effect and Compton recoil. Because $\langle \mathbf{v} \rangle = 0$, this effect is second order in the velocity, or linear in the electron temperature, and results in a spectral distortion not respecting the frequency dependence of a blackbody spectrum with a perturbed temperature. (See Fig. 19.) (ii) In the kinetic Sunyaev-Zeldovich (kSZ) effect the peculiar velocity of the gas results in a shift in temperature proportional to the component of the peculiar velocity along the line of sight. The kSZ effect has the same frequency dependence as the underlying primary CMB perturbations, thus making it hard to detect given its small magnitude. There is also a much smaller effect where the transverse peculiar velocity imparts a linear polarization to the scattered photons for which the polarization tensor P_{ij} is proportional to $(\mathbf{v}_\perp \otimes \mathbf{v}_\perp - \frac{1}{2}v_\perp^2 \boldsymbol{\delta}_\perp)$, where \mathbf{v}_\perp is the peculiar velocity perpendicular to the line of sight and $\boldsymbol{\delta}_\perp$ is the Kronecker delta function in the plane perpendicular to the line of sight.

Galaxy clusters are filled with hot gas [$T_{\text{gas}} = O(10 \text{ KeV})$] that emits primarily at X-ray frequencies. The hot electrons of this fully ionized gas, or plasma, scatter CMB photons by Thomson, or Compton, scattering, shifting their frequency by a factor of approximately $(1 + \beta \cos \theta)$ where $\beta = k_B T / m_e c^2$ and we have ignored higher order corrections in β . The y -distortion parameter along a line of sight is given by the integral

$$y = \int d\tau \frac{k_B T_e}{m c^2} = \int d\ell \sigma_T n_e \frac{k_B T_e}{m c^2}, \quad (82)$$

and the fractional perturbation in the CMB thermodynamic temperature in the nonrelativistic approximation is given by

$$\frac{\delta T_{\text{CMB}}(\nu, \hat{\Omega})}{\bar{T}_{\text{CMB}}} = \left(\frac{x(e^x + 1)}{e^x - 1} - 4 \right) y(\hat{\Omega}), \quad (83)$$

where $x = h\nu / k_B T_{\text{CMB}} = \nu / (57 \text{ GHz})$ and $y(\hat{\Omega})$ is the y -distortion map as defined by the line of sight integral in Eq. (82).

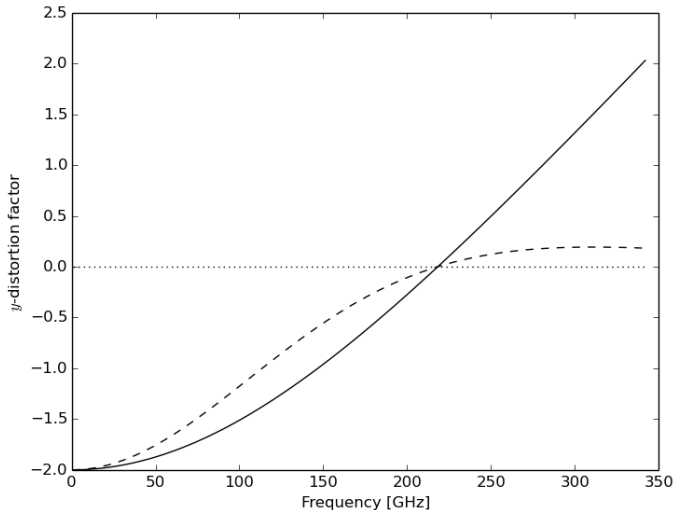


Figure 19: **Frequency dependence of thermal Sunyaev-Zeldovich spectral distortions.** The solid and dashed curves show the fraction spectral distortion in terms of the CMB thermodynamic and R-J temperatures, respectively. For low frequencies ($\nu < 217$ GHz), there is a decrement in temperature, corresponding to the fact that low frequency photons are on the average Doppler shifted to higher frequencies by the hot electrons. On the other hand, for $\nu > 217$ GHz the net effect is to increase the photon phase space density.

On the one hand, the thermal Sunyaev-Zeldovich effect provides a powerful probe of the dynamics of galaxy clusters, which can be used to discover new clusters and to probe the structure of known clusters away from their central core. On the other hand, for observing the primordial CMB, the thermal Sunyaev-Zeldovich effect constitutes a contaminant that must either be removed or modelled. The review by Birkinshaw [19] recounts the early history of tSZ measurements. See also the reviews by Carlstrom *et al.* [29] and by Rephaeli [195]. For the observation of the kSZ, see Ref. [80]. For more recent measurements, see the SZ survey papers from the ACT [133], SPT[232], and Planck [173, 174] collaborations. See Ref. [189] for a discussion of what might ultimately be possible from space in the future.

14 Experimental Aspects of CMB Observations

Like astronomical observations at other wavelengths, most modern microwave experiments consist of a telescope and a number of detectors situated at its focal plane. The COBE experiment was an exception, as it used single-moded feed horns pointed directly at the sky to define its beam, which was relatively broad (7° FWHM). However for measurements at higher angular resolution, it is difficult to construct a feed horn forming a sufficiently narrow beam on the sky without the help of intermediate optics, unless one resorts to interferometry as for example in the DASI experiment.

Observations of the sky at microwave frequencies present a number of challenges unique to this frequency range. Unlike at other frequencies, the microwave sky is remarkably isotropic. The CMB monopole moment, and to a much lesser extent the dipole moment, dominates. In the bands where other contaminants contribute least—that is, roughly in the range 70–150 GHz—virtually all the photons collected result from the isotropic 2.725 K background. The brightest feature superimposed on this uniform background is the CMB dipole, resulting from our proper motion with respect to the cosmic rest frame, at the level of 0.1%. When

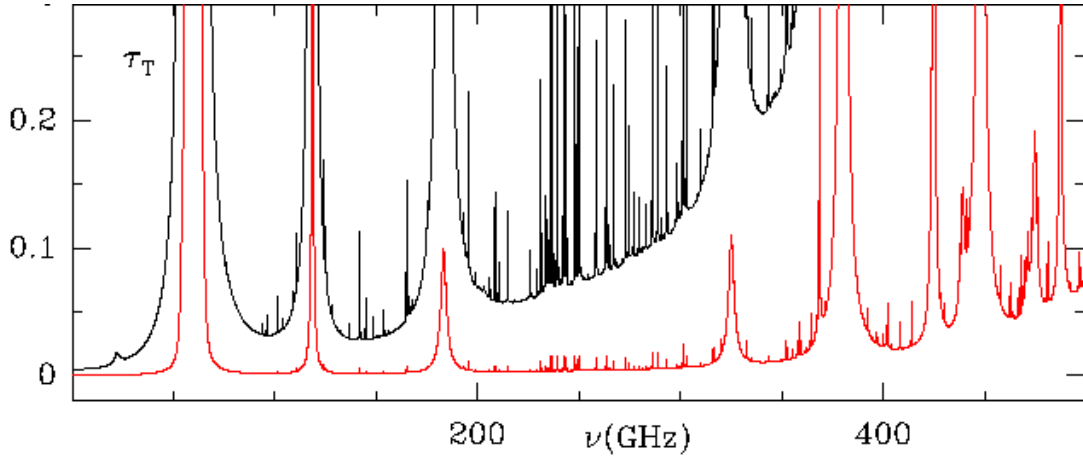


Figure 20: **Atmospheric optical depth as a function of frequency for 1 mm of precipitable water vapor.** Water vapor is an important but not the only source of atmospheric contamination. See Ref. [148] for more details. A column density of 0.5–1 mm of precipitable water vapor corresponds to good conditions in the Atacama deserts. Conditions at the South Pole are often better by a factor of a few. The black curve shows the opacity, or optical depth, and the red curve shows the opacity multiplied by $1/20$ in order to highlight the structure around the resonances. The limited transmission $0 < t < 1$ [where $t = \exp(-\tau)$], on the one hand, attenuates the desired sky signal. But more serious is the superimposed additive noise, having a brightness temperature $(1 - t)T_{\text{atm}}$. Here T_{atm} is the effective temperature of the atmosphere. (*Credit: J. Cernicharo*)

this dipole component is removed, the dominant residual is the primordial CMB anisotropy, whose amplitude on large angular scales is about $35 \mu\text{K}$, or roughly 10^{-5} . This situation is to be contrasted for example with X-ray astronomy where only some 50 photons need to be collected to make an adequate galaxy cluster detection. For the CMB about 10^{10} photons must be collected in each pixel just to obtain the temperature anisotropy at a signal-to-noise ratio of one, and many more photons are needed for measuring polarization at the same marginal signal-to-noise. The challenge is to measure minute differences in temperature between different points on the celestial sphere without introducing spurious effects. These can arise from a variety of sources: drifts in the zero point of the detector, detector noise, hot objects in the far sidelobes of the beam, and diffraction around the edges of the mirrors, to name some of the most common problems.

For this reason, almost all measurements of the microwave sky are in some sense differential. Drifts in the zero point of the detector (known as $1/f$ noise) can be mitigated by rapidly switching either between the sky and an artificial cold load with a long time constant or between different parts of the sky. This can be accomplished by moving the beam rapidly across the sky, so that in one way or the other the basic observable becomes differences in intensity of pixels whose measurements are closely separated in time. The point to take away is that one absolutely avoids making direct rather than differential measurements of the sky temperature.

Another specificity of astronomical observations at microwave frequencies is that extremely stringent requirements must be imposed limiting the magnitude of the far sidelobes of the

beam. Given the smallness of the differences in temperature of interest, contamination from the ground, the earth, the sun, and moon, and also from the galaxy near the galactic plane, can easily introduce spurious signals if the beam does not fall sufficiently rapidly away from its central peak. Ground pickup (from a spherical angle of 2π) is particularly challenging to shield, and this is why the WMAP and Planck satellites were situated at L2 (the second Lagrange point, where the earth and the moon have a tiny angular diameter) rather than in a low-earth orbit, which would equally well avoid atmospheric emission, which is the other major motivation for going to space. The second earth-sun Lagrange point (L2) is 1.5×10^6 km from the earth—that is, about 4 times the earth-moon distance. From L2 the earth subtends an angle of only 16 arcminutes. More importantly from L2, the sun, earth, and moon all appear at approximately the same position in the sky making it easier to keep away from the far sidelobes of the beam.

A formidable challenge for suborbital observations is emission from the atmosphere, primarily but not exclusively from water vapor. The emission from the atmosphere has a complicated frequency dependence, as shown in Fig. 20, where the optical depth as a function of frequency is shown. This optical depth must be multiplied by the atmospheric temperature (i.e., ≈ 270 K) to obtain the sky brightness. The structure in frequency of the regions of high opacity implies that bands must be carefully chosen to avoid emission lines and bands, giving less flexibility for wide frequency coverage than from space. The problems arising from atmospheric emission can be mitigated to some extent by choosing a site on the ground with a particularly small water column density, such as the South Pole or the Atacama desert in Chile, or by observing from a stratospheric balloon. Atmospheric emission is problematic in two respects. First, if the atmospheric emission were stable in time, it would merely introduce additional thermal loading on the detectors, which could be mitigated simply by deploying more detectors or by observing over a longer time. If the contribution from the sky is T_{sky} , then the fluctuations in intensity at the detector (assumed perfect for the moment) would increase by a factor of $(T_{\text{sky}} + T_{\text{CMB}})/T_{\text{CMB}}$, meaning that we could measure the sky temperature with the same error by increasing either the number of detectors or the total observation time by a factor of $((T_{\text{sky}} + T_{\text{CMB}})/T_{\text{CMB}})^2$. At 150 GHz from the South Pole, for example, to choose a band where the sky brightness temperature is not very high, one has $T_{\text{sky}} \approx 16$ K. This means that under the idealized assumptions made here, almost 40 times more detectors would be required than for a space-based experiment. But the situation is worse than this, because the atmosphere contamination is not stable in time but rather fluctuates in a complicated way characterized by a wide range of time scales (owing to the underlying turbulence). Moreover, the atmospheric load varies with zenith angle, roughly according to a secant law. Of course, observations from the ground are attractive because of their low cost, the fact that telescopes can be improved from season to season to address problems as they arise, and larger telescopes with many more detectors can be deployed. As experiments increase in sensitivity, requirements for mitigating these problems will become more stringent. At present it is not known what is the limit on the quality of measurements that can be achieved from the ground or from balloons.

14.1 Intrinsic photon counting noise: ideal detector behavior

In radio astronomy (where the frequency of observations is typically lower than for CMB observations) the following expression, known as the radio astronomers' equation [45, 111],

gives the fractional error of an observation under slightly idealized assumptions:

$$\frac{\delta I}{I} = \left[\frac{T_{\text{sky}} + T_{\text{sys}}}{T_{\text{sky}}} \right]^2 \frac{1}{\sqrt{(\Delta B)t_{\text{obs}}}}. \quad (84)$$

Here t_{obs} is the time of observation of a pixel and (ΔB) is the bandwidth. T_{sky} is the sky brightness temperature averaged over the pixel and T_{sys} represents the additional noise introduced within the receiver. This expression can be understood by considering the source in the sky as having thermal statistics—that is, fluctuating in intensity as a Gaussian random field. In radio astronomy, detection is coherent and each detector picks up only a single transverse mode of the electromagnetic field incident from the sky, which is converted by an antenna or a feed horn into an electrical signal, which depends only on time. This signal is coherently amplified and nowadays digitized. Mathematically, in the absence of additional detector noise, the sky signal can be thought of as a signal whose complex amplitude fluctuates according to a Gaussian distribution with a variance proportional to T_{sky} . The coherence time is $1/(\Delta B)$, so in a time interval t_{obs} , $N_{\text{samp}} = 2(\Delta B)t_{\text{obs}}$ independent realizations of this Gaussian random process whose variance we are trying to measure are collected, leading to a fractional error in the determination of the variance, or T_{sky} , of $1/\sqrt{N_{\text{samp}}}$. For a more realistic measurement noise is also introduced, and in the above formula the noise is idealized as an independent additive Gaussian random signal, characterized in terms of a system temperature T_{sys} , to be added to T_{sky} to obtain the variance actually measured. The additive noise lumped together and known as the “system” temperature includes thermal emission from the atmosphere, Johnson noise from dielectric losses in the feedlines, noise in the detector itself—in other words, everything other than the sky temperature that one would measure from space with an ideal measuring device.

The above formula was derived treating the incoming electromagnetic field as entirely classical, and for a thermal source this treatment is valid in the R-J part of the spectrum—that is, when $T_{\text{source}} \gg h\nu/k_{\text{B}}$. For the CMB, with $T_{\text{CMB}} = 2.725$ K, this requires that $\nu \lesssim \nu_{\text{CMB}} = k_{\text{B}}T_{\text{CMB}}/h = 57$ GHz, meaning that quantum effects introduce significant corrections to the above formula, but one is still far from the regime where photons arrive in a nearly uncorrelated way, obeying Poissonian counting statistics, which is what happens for observations in the extreme Wien tail of the blackbody distribution. Before introducing the quantum corrections to Eq. (84), let us finish our discussion of this result based on classical theory extracting all the lessons to be learnt from this result. In the R-J regime, where $N \gg 1$, N being the photon occupation number, roughly speaking, photons arrive in bunches of N photons, so the discreteness of the photons is not an issue. As long as a fraction greater than about $1/N$ of the photons is captured, little additional noise is introduced. The intrinsic noise of the incoming electromagnetic field is almost entirely classical in origin and can be modeled faithfully using stochastic classical electromagnetic formalism. (For a more detailed discussion of these issues, see Ref. [132].) From the above formula, we learn that noise can be reduced by the following measures: (i) choosing as wide a bandwidth as possible, (ii) increasing the observation time, and (iii) increasing the number of detectors. We also learn that although lowering the internal noise of the detection system increases the accuracy of the measurements, once the system temperature is approximately equal to the brightness temperature of the source, lowering the system temperature further leads only to marginal improvement in sensitivity.

We now derive the quantum corrected version of the radio astronomer’s equation, using a Planck distribution instead of the classical description based on a deterministic stochastic

Gaussian field. For the Planck distribution, where $p_N = x^N/(1-x)$ with $x = \exp(-h\nu/k_B T)$,

$$\langle(\delta N)^2\rangle = \langle N\rangle^2 + \langle N\rangle = \bar{N}^2 + \bar{N}. \quad (85)$$

In the R-J regime, where $\bar{N} \gg 1$, the first term dominates, reproducing the result obtained using a classical random field as described above. But as the frequency is increased and one starts to pass toward the Wien tail of the distribution, the second term increases in importance. In the extreme Wien tail, where the second term dominates, we observe the fluctuations characterized by Poisson statistics, where the (rare) arrivals of photons are completely uncorrelated. This means that the fractional error for the number of photons counted must be increased by a factor of

$$\left(1 + \frac{1}{\bar{N}}\right) = \exp\left(\frac{h\nu}{2k_B(T_{\text{sky}} + T_{\text{sys}})}\right), \quad (86)$$

and the quantum-corrected version of Eq. (84) becomes [113]

$$\frac{\delta I}{I} = \left(\frac{T_{\text{sky}} + T_{\text{sys}}}{T_{\text{sky}}}\right)^2 \frac{1}{\sqrt{(\Delta B)t_{\text{obs}}}} \exp\left(\frac{h\nu}{2k_B(T_{\text{sky}} + T_{\text{sys}})}\right). \quad (87)$$

14.2 CMB detector technology

Having analyzed the performance of an ideal detector limited only by the intrinsic fluctuations of the incoming electromagnetic field, we now review the state of the art of existing detector technologies, which may be divided into two broad classes: (i) coherent detectors, and (ii) incoherent detectors.

Coherent detectors transfer the signal from a feed horn or antenna onto a transmission line and then coherently amplify the signal using a low-noise amplifier, generally using high electron mobility transistors (HEMTs) and switching with a cold load or between different points on the sky in order to mitigate $1/f$ noise [187]. Coherent detection is an older technology. Coherent detectors have the advantage that they can operate at much higher temperatures than the competing incoherent bolometric detectors. Avoiding active cooling through a cryogenic system is a definite plus, especially in space, where reducing risk of failure is important. However, unlike their incoherent competitors, at the high frequencies of interest for CMB observations, coherent detectors have noise levels far above the quantum noise limit, and until now coherent detectors have not been able to reach frequencies above circa 100 GHz, although some believe that this situation may improve. It is not presently known how coherent amplification would function in the Wien part of the blackbody spectrum. Coherent detectors were used for the COBE DMR experiment, for WMAP (including the frequencies 20, 30, 40, 60, and 90 GHz), and the Planck LFI (low frequency instrument), which included the frequencies 30, 45, and 70 GHz. One advantage of coherent detectors is their insensitivity to cosmic rays.

Another property of coherent detectors is that for a single mode measurement, all four Stokes parameters (i.e., I, Q, U, V) can be measured simultaneously. For incoherent detectors one can measure only two Stokes parameters simultaneously. However for measurements outside the R-J part of the spectrum, this advantage of coherent detectors disappears, because in the Wien part of the spectrum, the photons are not bunched to any appreciable degree. On the other hand, for coherent detectors, it is not possible to construct multi-moded detectors, where the number of detectors can be greatly reduced by sacrificing angular resolution, but

not at the cost of less sensitivity on large angular scales. Coherent detectors are always single-moded, sampling at the diffraction limit.

Incoherent detectors, unlike their coherent counterparts, do not attempt to amplify the incident electromagnetic wave. Rather the incident electromagnetic wave, or equivalently the stream of photons, is directly converted into heat, changing the temperature of a small part of the detector of small heat capacity, whose temperature is monitored using a thermistor of some sort. Typically the detector is cooled to an average temperature much lower than that of the incident radiation. The bolometers of the Planck high frequency instrument (HFI) were cooled to 0.1 K. Consequently each CMB photon produces many phonons in the detector, and therefore the counting statistics of the phonons do not to any appreciable extent limit the measurement. Heat flows from the sky onto the detector and is then conducted to a base plate of high heat capacity and thermal stability. A thermal circuitry (which can be modelled as a sort of RC circuit with as many loops as time constants) is chosen with a carefully optimized time response.

Several technologies are used for the thermistor. One of the most popular nowadays is transition edge sensors (TES) [118], where a superconducting thin film is kept at the edge of the superconducting transition, so that minute changes in temperature give rise to large changes in resistivity. A feedback circuitry with heating is used to maintain the assembly near a fixed location on the normal-superconducting transition edge. One disadvantage of TES detectors is their low electrical impedance, which requires that SQUIDS (superconducting quantum interference devices), which need careful magnetic shielding, be used for the readout.

Several new promising technologies are being developed and perfected for the next generation of bolometric detectors. One such technology is kinetic inductance detectors (also known as KIDs) [41, 47]. For these detectors, a resonant electric circuit is constructed by depositing a pattern of superconducting film on a thick dielectric. Photons incident on the superconducting film break Cooper pairs causing its surface impedance to vary with the incident photon flux, which in turn alters the resonant frequency. The shifts in frequency of the resonator allow the KID to be read out in a simple way without using SQUIDS. The surface impedance of the superconducting film is largely determined by the inertia of the superconducting electrons, hence the name “kinetic inductance.”

Another possibly promising technology is the cold electron bolometer [112], involving a small metal filament connected to a superconductor on both sides by means of a junction with a thin insulator in between. A bias current that passes through the assembly acts to cool the electrons in the thin wire through a Peltier-like effect to a temperature far below that of the substrate. CEBs are hoped to be more resistant to cosmic ray spikes than other detector technologies.

Cosmic rays have proved to be more problematic than anticipated in the Planck experiment, and substantial effort was needed to remove the contamination from cosmic ray events in the raw time stream [185]. Some of the data was vetoed and corrections were applied to the long-time tails of the larger magnitude events. While experiments from the ground benefit from substantial shielding of cosmic rays by the Earth’s atmosphere, how best to minimize interference from cosmic rays will be a major challenge for the next generation of experiments from space, which target sensitivities more than two orders of magnitude beyond the Planck HFI. Another challenge will be multiplexing, which is necessary to reduce the cooling requirements when the number of detectors is greatly expanded.

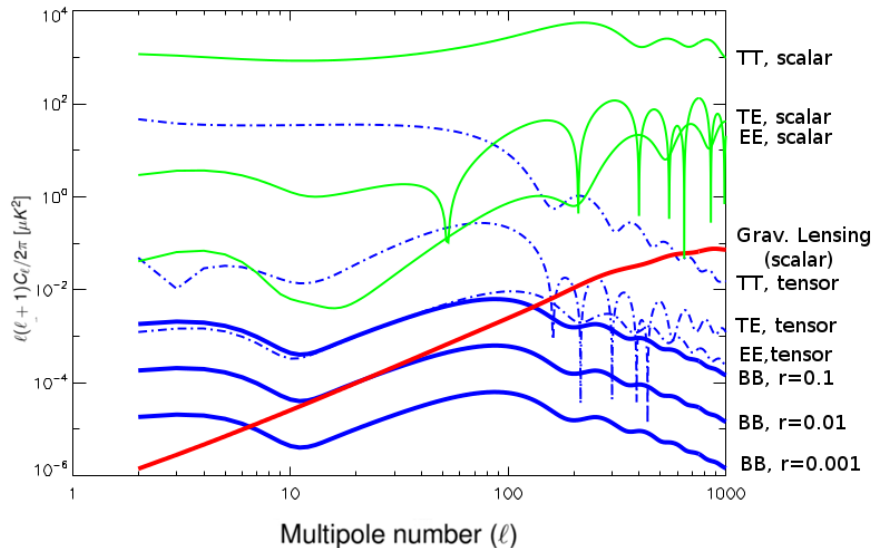


Figure 21: **Summary of T,E, and B anisotropy power spectra from scalar and tensor modes.** The green curves (from top to bottom) represent the TT, TE and EE CMB power spectra for the “scalar” mode, while the blue curves represent the CMB isotropies for the tensor mode. The broken blue curves (from top to bottom) and the top solid blue curve represent the TT, TE, EE and BB anisotropies assuming a value of the tensor-to-scalar ratio of $r = 0.1$. The lower two solid curves represent the predicted BB anisotropy for $r = 0.01$ and $r = 0.001$. The red curve shows the BB power spectrum arising nonlinearly from the scalar mode as a result of gravitational lensing. (*Credit: M. Bucher*)

14.3 Special techniques for polarization

If it were not for the fact that the polarized CMB anisotropy (i.e., the Q and U Stokes parameters) is much smaller than the anisotropy in the I Stokes parameter, measuring polarization would not pose any particular problems, because most detectors are polarization sensitive or can easily be made so, and there would be no need to discuss any techniques particular to polarization measurements. An inspection of the relative amplitudes of the spectra in Fig. 21 highlights the problems encountered. In particular if one wants to search for B modes at the level of $r \approx 10^{-3}$ or better, the requirements for preventing leakages of various types become exceedingly stringent, as we now describe.

Let us characterize the problem for the most difficult polarization observation: measuring the primordial B modes. We may classify the leakages to be avoided by ordering them from most to least severe: (i) leakage of the CMB temperature monopole to the B mode, (ii) leakage of the T anisotropies to the B mode, and (iii) leakage of the E mode to the B mode.

One of the solutions to many of these problems is polarization modulation. The idea is to place an element such as a rotating half-wave plate, whose orientation we shall denote by the angle θ , between the sky and the detector, preferably as the first element of the optical chain, as sketched in Fig. 22. Half-wave plates can be constructed using anisotropic crystals such as sapphire or using a mirror with a layer of wires a certain distance above it so that one

linear polarization reflects off the wires while the other reflects off the mirror, resulting in a difference in path length. Mathematically, we have

$$\begin{aligned} \begin{pmatrix} E_x^{(\text{out})} \\ E_y^{(\text{out})} \end{pmatrix} &= \begin{pmatrix} +\cos(\theta) & -\sin(\theta) \\ +\sin(\theta) & +\cos(\theta) \end{pmatrix} \begin{pmatrix} 1 & 0 \\ 0 & -1 \end{pmatrix} \begin{pmatrix} +\cos(\theta) & +\sin(\theta) \\ -\sin(\theta) & +\cos(\theta) \end{pmatrix} \begin{pmatrix} E_x^{(\text{in})} \\ E_y^{(\text{in})} \end{pmatrix} \\ &= \begin{pmatrix} +\cos(2\theta) & +\sin(2\theta) \\ -\sin(2\theta) & -\cos(2\theta) \end{pmatrix} \begin{pmatrix} E_x^{(\text{in})} \\ E_y^{(\text{in})} \end{pmatrix}, \end{aligned} \quad (88)$$

so that in terms of the Stokes parameters, expressed below as the matrix-valued expectation value $\langle \mathcal{E}_i < \mathcal{E}_j^* \rangle$, so that

$$\begin{aligned} &\begin{pmatrix} I + Q & U + iV \\ U - iV & I - Q \end{pmatrix}_{\text{det}} \\ &= \begin{pmatrix} \cos 2\Omega t & \sin 2\Omega t \\ \sin 2\Omega t & -\cos 2\Omega t \end{pmatrix} \begin{pmatrix} I + Q & U + iV \\ U - iV & I - Q \end{pmatrix}_{\text{sky}} \begin{pmatrix} \cos 2\Omega t & \sin 2\Omega t \\ \sin 2\Omega t & -\cos 2\Omega t \end{pmatrix} \\ &= \begin{pmatrix} I + \cos(4\Omega t)Q + \sin(4\Omega t)U & -\cos(4\Omega t)U + \sin(4\Omega t)Q - iV \\ -\cos(4\Omega t)U + \sin(4\Omega t)Q + iV & I - \cos(4\Omega t)Q - \sin(4\Omega t)U \end{pmatrix}. \end{aligned} \quad (89)$$

By measuring only the component that varies with an angular frequency 4Ω , we can measure the polarization without making two independent measurements of large numbers that are then subtracted from each other. The much larger Stokes intensity I does not mix because it remains constant in time.

To see how polarization modulation helps, let us suppose that the vector $\mathbf{P}_{\text{det}}^{(\text{ideal})} = (I_{\text{det}}^{(\text{ideal})}, Q_{\text{det}}^{(\text{ideal})}, U_{\text{det}}^{(\text{ideal})}, V_{\text{det}}^{(\text{ideal})})$ is replaced by the vector $\mathbf{P}_{\text{det}}^{(\text{actual})}$, with $\mathbf{P}_{\text{det}}^{(\text{actual})} = (I_{\text{det}}^{(\text{actual})}, Q_{\text{det}}^{(\text{actual})}, U_{\text{det}}^{(\text{actual})}, V_{\text{det}}^{(\text{actual})}) = (\mathbf{I} + \boldsymbol{\epsilon})\mathbf{P}_{\text{det}}^{(\text{ideal})}$, where \mathbf{I} is the identity matrix and $\boldsymbol{\epsilon}$ represents a hopefully small but unknown uncorrected residual error in the actual linear response of the detector pair.

We discuss the setup for measuring polarization used in Planck as described above (see Fig. 23). We describe some of the possible systematic effects and how polarization modulation by means of a rotating half-wave plate would remove these systematic effects. Ideally the two orthogonal grids of wires would correspond, but for the direction of the linear polarization, to exactly the same circular beam on the sky and be perfectly calibrated, with no offset between the beam centers, nor any time-dependent drift of the differential gain. But in practice the beams are not identical and the gain and offset of the electronics drift in time. The centers of the beams do not coincide, and without corrections this would cause a local gradient of the T to be mistaken for E or B polarization. Differential ellipticity would cause the second derivative of T to leak into E and B . Moreover, the actual beams are more complicated and require three functions [i.e., maps of $I(\hat{\Omega})$, $Q(\hat{\Omega})$, and $U(\hat{\Omega})$] for a complete description. All the above effects disappear, at least ideally, with the polarization modulation scheme described above. Polarization modulation can resolve or mitigate a lot of problems but is not a panacea. For example, polarization modulation cannot prevent $E \rightarrow B$ leakages. If there are any errors in the calibration of the angles of the direction of the linear polarization in the sky, these errors act to rotate E into B and vice versa. Moreover polarization modulation has been difficult to realize in practice for a number of reasons such as spurious signals due to microphonic

coupling. Both continuously rotating and discretely stepped half-wave plates are options for polarization modulation.

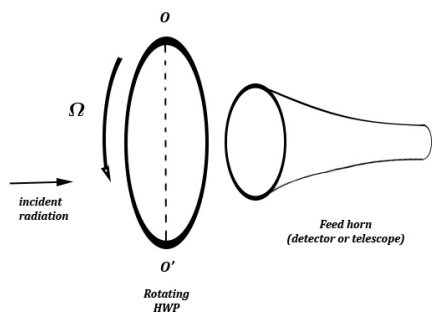


Figure 22: **Polarization modulation by a rotating half-wave plate.** We show a transmissive rotating half-wave plate (HWP), here placed in front of a microwave feed horn pointing directly at the sky. However for modern CMB experiments, the horn would generally be replaced with a telescope having intermediate optical elements and horns on the focal plane. The rotating HWP is birefringent, with its fast polarization axis represented by the line OO' . As explained in the main text, by measuring only that part of the signal varying at an angular frequency 4Ω (where Ω is the angular velocity of the rotating HWP), one can prevent leakage from the much larger Stokes parameter I into the linearly polarized components Q and U . The presence of the HWP, while complicating the instrument design somewhat, allows many hardware requirements to be relaxed substantially compared to what would be needed without polarization modulation.

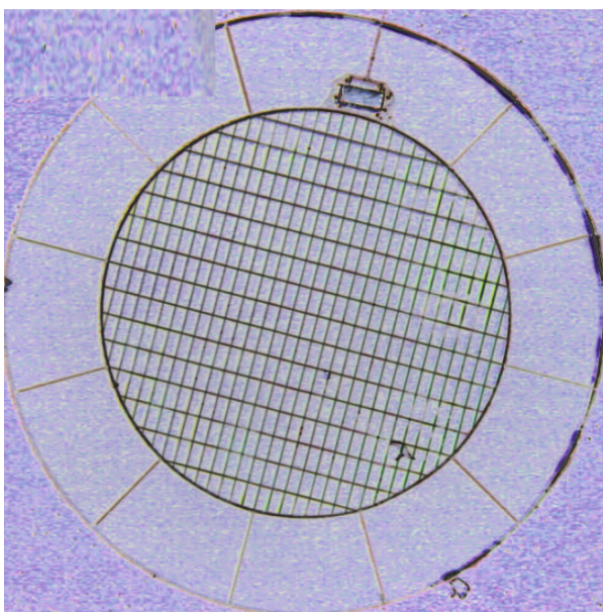


Figure 23: **Planck polarization sensitive bolometers.** Shown above is a photograph of one of the Planck polarization sensitive bolometers consisting of two grids of parallel wires oriented orthogonally and placed on top of each other but separated by a small distance. Each grid has its own thermistor, allowing the two selected components of the linear polarizations to be read out separately. (*Credit: ESA/Planck Collaboration*)

15 CMB Statistics Revisited: Dealing with Realistic Observations

The analysis of a CMB experiment going from the raw time stream of data taken, to sky maps at a given frequency, then to a clean sky map containing only the CMB, and finally to a likelihood function, whose input is a complete theoretical power spectrum, involves many steps and details. Space does not permit a complete discussion. The following Planck papers and references therein describe this analysis for the Planck experiment from the Planck 2013 Results series. See in particular the following papers: Overview of products and results [165], low frequency instrument data processing [183], high frequency instrument data processing [184], component separation [166], and HFI energetic particle effects [185]. Similar descriptions can be found for other experiments. In this Section, we limit ourselves to sketching a few issues and to describing an idealized statistical analysis.

One of the main steps in CMB analysis is constructing a likelihood for the data given a particular theoretical model. Relative likelihood lies at the heart of almost all statistical inference, whether one uses frequentist methods, Bayesian methods, or an ecumenical approach borrowing from both doctrines. Here we shall discuss only how to formulate the likelihood, as how to exploit the likelihood is less specific to the CMB and details can be found in standard treatises on modern statistics. (See for example Ref. [127] for a brief overview and Ref. [219] for an authoritative treatment emphasizing the frequentist approach. For Bayesian sampling as applied to the CMB, see Refs. [123] and [57] and references therein.)

Constructing a likelihood is straightforward for an idealized survey for which the noise

in the sky maps is Gaussian and isotropic. For the simplest likelihood function, the input argument is a model for the CMB sky signal, or more precisely the parameters defining this model. This theoretical model defines an isotropic Gaussian stochastic process whose parameters one is trying to infer. In order to introduce some of the complications that arise, we start by writing down the likelihood \mathcal{L} for the data given the model, or rather the variable $-2\ln[\mathcal{L}]$, which in some ways resembles χ^2 in the Gaussian approximation. We have

$$-2\ln(\mathcal{L}) = \sum_{\ell=2}^{\infty} (2\ell + 1) \left\{ \ln \left(\frac{B_{\ell} C_{\ell}^{\text{TT},(th)} + N_{\ell}}{C_{\ell}^{\text{TT},(sky)} + N_{\ell}} \right) + \left(\frac{C_{\ell}^{\text{TT},(sky)} + N_{\ell}}{B_{\ell} C_{\ell}^{\text{TT},(th)} + N_{\ell}} \right) - 1 \right\}. \quad (90)$$

Here the parameters N_{ℓ} represent the noise of the measurement. In the approximation of white instrument noise—that is, with no unequal time correlations—we have $N_{\ell} = N_0$. The factor B_{ℓ} represents the smearing of the sky signal due to the finite beam width. For the beam profile approximated as having a Gaussian shape, $B_{\ell} = \exp[-\sigma^2 \ell^2]$ where the sky intensity map is convolved with the Gaussian function $K(\theta) = (1/\sqrt{2\pi\sigma^2}) \exp[-\theta^2/(2\sigma^2)]$.^u Note that we ignore constant offsets in the log likelihood because for most statistical analysis only differences in the log likelihood are relevant. The presence of the normalization of the Gaussian imply that a quadratic representation of the log likelihood is not exact and higher order corrections are needed to avoid bias, especially at low ℓ .

To generalize the above expression to include polarization, we define the matrix

$$\mathbf{c}_{\ell} = \begin{pmatrix} C_{\ell}^{\text{TT}} + B_{\ell}^{-1} N_{\ell}^{\text{TT}} & C_{\ell}^{\text{TE}} \\ C_{\ell}^{\text{TE}} & C_{\ell}^{\text{EE}} + B_{\ell}^{-1} N_{\ell}^{\text{EE}} \end{pmatrix}, \quad (91)$$

so that

$$-2\ln(\mathcal{L}) = \sum_{\ell=2}^{\infty} (2\ell + 1) \{ \ln[\mathbf{c}_{\ell}^{(th)} (\mathbf{c}_{\ell}^{(\text{obs})})^{-1}] + \text{tr}[\mathbf{c}_{\ell}^{(\text{obs})} (\mathbf{c}_{\ell}^{(th)})^{-1}] - 2 \}. \quad (92)$$

In order to generalize to less idealized (i.e., more realistic) situations, it is useful to rewrite the above results in a more abstract matrix notation, in which the expressions can be interpreted simultaneously as expressions in real (i.e., angular) space and as expressions in harmonic space.

$$-2\ln[\mathcal{L}] = \det(\mathbf{C}_{th} + \mathbf{N}) + \mathbf{t}^T (\mathbf{C}_{th} + \mathbf{N})^{-1} \mathbf{t}. \quad (93)$$

Here the vector \mathbf{t} represents the observed sky map, \mathbf{C}_{th} is the covariance matrix of the underlying sky signal (in general depending on a number of parameters whose values one is trying to infer), and \mathbf{N} represents the covariance matrix of the instrument (and other) noise. In the idealized case where everything is isotropic, this is simply a rewriting of Eq. (90), but in less idealized cases the likelihood in Eq. (93) is correct whereas Eqs. (90) and (92) are not applicable to the more general case.

Let us now consider the effect of partial sky coverage, which may result from a survey that does not cover the whole sky or from masking portions of the sky such as the galaxy and bright point sources where contamination of the primordial signal cannot be corrected for in a

^uNote that in the literature, beam widths are generally specified in terms of FWHM rather than using the Gaussian definition above.

reliable way. If the vectors and matrices in Eq. (93) are understood as representations in pixel space, at least formally there is no difficulty in evaluating this expression in the subspace of pixel space representing the truncated sky. If the dimensionality of the pixelized maps were small, there would be no difficulty in simply evaluating this expression by brute force. Another complication arises from inhomogeneous noise. Most surveys do not cover the sky uniformly because requirements such as avoiding the sun, the earth, and the planets as well as instrumental considerations lead to nonuniform sky coverage. This leads to a noise matrix that has a simple representation in pixel space (under the assumption of white noise), but not in harmonic space.

Unfortunately evaluating likelihoods such as in Eq. (93) exactly is not possible for full-sky surveys at high angular resolution such as the Planck survey for which pixelized maps include up to about $N_{\text{pix}} = 5 \times 10^7$ pixels. While \mathbf{C}_{th} is simple (i.e., sparse) in harmonic space, it is dense in pixel space, and the opposite holds for \mathbf{N} (ignoring correlated noise), so no representation can be found to simplify the calculation in which all the matrices are sparse. Since even enumerating the matrices involves $O(N_{\text{pix}}^2)$ operations, and inverting these matrices or taking their determinant requires $O(N_{\text{pix}}^3)$ operations, it is immediately apparent that brute force will not work, and more clever, approximate techniques are required. Pixel based likelihoods are however used at low- ℓ , where other approximations have difficulty representing the likelihood, in large part because the cosmic variance is non-Gaussian.

While the likelihoods above assumed an isotropic Gaussian stochastic process for the underlying theoretical model generating the anisotropy pattern in the sky, these likelihoods can be generalized to include nonlinear effects, such as non-Gaussianity through f_{NL} , gravitational lensing, and certain models of weak statistical anisotropy, to name just a few examples. Using the likelihood as a starting point, possibly subject to some approximations, has the virtue that one is guaranteed that an optimal statistical analysis will result without any special ingenuity.

In the above simplified discussion, we have not touched on a number of very important issues, of which we list just a few examples: asymmetric beams, far side-lobe corrections, band-pass mismatch, errors from component separation, estimating noise from the data, and null tests (also known as “jackknives”). The reader is referred to the references at the beginning of this Section for a more complete discussion and references to relevant papers.

16 Galactic Synchrotron Emission

An inspection of the single frequency temperature maps from the Planck space mission (see Fig. 8), shown here in galactic coordinates so that the equator corresponds to the galactic plane, suggests that the 70 GHz frequency map is the cleanest, as the excess emission around the galactic plane is the narrowest at this frequency. But at lower frequencies, the region where the galactic contamination dominates over the primordial CMB temperature anisotropies widens. This contamination at low frequencies is primarily due to galactic synchrotron emission, resulting from ultrarelativistic electrons spiralling in the galactic magnetic field, whose strength is of order a few microgauss. (See for example Ref. [78].) This emission is generally described as nonthermal because the energy spectrum of charged particles is non-Maxwellian, especially at high energies. The electrons in question reside in the high energy tail of the electron energy spectrum, described empirically as a falling power law spectrum. Models of cosmic ray acceleration, for example arising about a shock from an expanding supernova remnant, are able to explain spectra having such a power law form [20]. If the

radiating charged particles were nonrelativistic, their radiation would be emitted at the cyclotron frequency $\omega_c = eB/mc$, with very little emission in higher harmonics, and given the measured values of the galactic magnetic field, one could not thus explain the observed high frequency emission. However, if the charged particles are highly relativistic, due to beaming effects the bulk of the radiation is emitted in the very high order harmonics, allowing the observed emission to be explained for reasonable values of the galactic magnetic field [70]. Although the data concerning the three-dimensional structure of the galactic magnetic field is at present in a very rudimentary state, and little is known observationally about the cosmic ray spectrum outside our immediate solar neighborhood, the physical mechanism underlying galactic synchrotron emission is well understood physics. One important point is that no matter what the details of the cosmic ray energy spectrum may be, the kernel of the integral transform relating this distribution to the frequency spectrum of the observed synchrotron emission applies considerable smoothing. Thus we can assume with a high degree of confidence that the synchrotron spectrum is smooth in frequency. Theory also predicts that this synchrotron emission will be highly polarized, at least to the extent that the component of the galactic magnetic field coherent over large scales is not negligible. This expectation is borne out by observations. It is customary to describe the synchrotron spectrum using a power law, so that its R-J brightness temperature may be fit by an Ansatz of the form

$$T_{R-J}(\hat{\Omega}, \nu) = T_{R-J}(\hat{\Omega}, \nu_0) \left(\frac{\nu}{\nu_0} \right)^\alpha, \quad (94)$$

where empirically it has been established that $\alpha \approx 2.7\text{--}3.1$. The same holds for the polarization—that is, the Stokes Q and U (and also V) parameters. In the ultrarelativistic approximation this emission is primarily linearly polarized, but there is also a smaller circularly polarized component suppressed by a factor of $1/\gamma$. Variations in the spectral index depending on position in the sky have been observed [68].

A description of the WMAP full-sky observations of synchrotron emission appears in the first-year WMAP foregrounds paper [238] and the polarization observations are described in the three-year WMAP paper on foreground polarization [244]. A greater lever arm, in particular for studying the synchrotron spectral index, can be obtained by including the 408 MHz Haslam map covering almost the entire sky [81].

17 Free-Free Emission

Another source of low-frequency galactic contamination is free-free emission arising from Bremsstrahlung photons emitted from electron-electron collisions in the interstellar medium, and to a lesser extent from electron-ion collisions. Like galactic synchrotron emission, the free-free emission brightness temperature falls with increasing frequency, but the fall-off is slower than that of the galactic synchrotron emission.

Unlike synchrotron emission, free-free emission is not polarized. $H\alpha$ ($n = 3 \rightarrow n = 2$) emission resulting from recombination of ionized atomic hydrogen can be used as a template for removing the free-free component, because the $H\alpha$ emission likewise is proportional to the square of the electron density. However, because the $\Gamma_{H\alpha}(T)$ and $\Gamma_{\text{free-free}}(T, \nu)$ do not have an identical temperature dependence, free-free removal using an $H\alpha$ template has some intrinsic error. $\Gamma_{H\alpha}(T)$ is defined as the constant of proportionality in the emissivity relation:

$\epsilon_{H\alpha} = \Gamma_{H\alpha}(T)n_e^2$ where $\epsilon_{H\alpha}$ is a bolometric emissivity (power per unit volume) and n_e is the density of free electrons. Likewise $\epsilon_{\text{free-free}}(\nu) = \Gamma_{\text{free-free}}(T, \nu)n_e^2$ where the emissivity has units of power per unit frequency per unit volume per unit solid angle.

18 Thermal Dust Emission

In Sec. 16 we discussed galactic synchrotron emission, whose R-J brightness temperature rises with decreasing frequency, making it exceedingly difficult to measure CMB anisotropies at frequencies below ≈ 20 GHz, especially close to the galactic plane where the galactic synchrotron emission is most intense. We also saw how the fact that the brightness temperature increases with decreasing frequency can be understood as a consequence of the synchrotron optical depth being much smaller than unity and increasing with decreasing frequency. Eventually when the frequency is low enough so that the optical depth is near one, the brightness temperature stops rising and approaches a temperature related to the cosmic ray electron kinetic energy.

This Section considers another component contributing to the microwave sky: the thermal emission from interstellar dust, whose brightness temperature increases in the opposite way—that is, the brightness temperature increases with increasing frequency. This behavior results because at microwave frequencies, the wavelength greatly exceeds the typical size of a dust grain. At long wavelengths, the cross-section for absorbing or elastically scattering electromagnetic radiation is much smaller than the geometric cross-section $\sigma_{\text{geom}} \approx a^2$ where a is the effective grain radius. The dust grains can be approximated as dipole radiators in this frequency range because higher order multipoles are irrelevant. The dependence of the cross-section on frequency can be qualitatively understood by modeling the electric dipole moment of the grain as a damped harmonic oscillator where the resonant frequency is much higher than the frequencies of interest. In this low frequency approximation

$$\sigma_{\text{abs}} \sim \left(\frac{a}{\lambda}\right)^2 a^2 \quad (95)$$

for absorption, and for the elastic, or Rayleigh, scattering component, which becomes subdominant at very low frequencies,

$$\sigma_{\text{elastic}} \sim \left(\frac{a}{\lambda}\right)^4 a^2. \quad (96)$$

This is a simplistic approximation that we later shall see is not accurate, but it does provide intuition about the qualitative behavior expected.

Our knowledge of interstellar dust derives from combining different observations spanning a broad range of frequencies, from the radio to the UV and even X-ray bands, in order to put together a consistent theoretical model able to account simultaneously for all the observations. (For a nice recent overview, see for example Refs. [48] and [49].) In this Section, we restrict ourselves to discussing the thermal microwave emission properties of the dust.

An empirical law commonly used to model thermal dust emission at low frequencies is a Planck blackbody spectrum modulated by a power law emissivity, or graybody factor

$$I_{\text{dust}}(\nu) = I_{\text{dust}}(\nu_0) \left(\frac{\nu}{\nu_0}\right)^\beta \frac{B(\nu, T_{\text{dust}})}{B(\nu_0, T_{\text{dust}})} \quad (97)$$

where the Planck spectrum is given by

$$B(\nu; T) = \frac{2h\nu^3}{c^2} \frac{1}{\left(\exp\left(\frac{h\nu}{k_B T}\right) - 1\right)}. \quad (98)$$

The physical basis for this modification to the Planck spectrum can be partially motivated by the following argument based on the linear electric susceptibility of the dust grain, following a line of reasoning first suggested by EM Purcell in 1969 [192]. The simple argument, subject to a few caveats, suggests that $\beta = 2$. However the observational data do not bear out this prediction and instead are better fit by a power law with $\beta \approx 1.4 - 1.6$ [147, 162]. Let $\chi(\omega)$ represent the linear susceptibility of a dust grain, which as a consequence of the Kramers-Kronig dispersion relations must include both nonvanishing real and imaginary parts. Here $\mathbf{d}(\omega) = \chi(\omega)\mathbf{E}(\omega)$, where $\mathbf{d}(\omega)$ and $\mathbf{E}(\omega)$ are the grain electric dipole moment and the surrounding electric field, respectively. As a consequence of causality, $\chi(\omega)$ is analytic on the lower half-plane. Its poles in the upper half-plane represent those decaying mode excitations of the grain that are coupled to the electromagnetic field. Moreover, on the real axis $\chi(-\omega) = [\chi(+\omega)]^*$. If we assume analyticity in a neighborhood of the origin, we may expand as a power series about the origin, so that

$$\chi(\omega) = \omega_0 + i\chi_1\omega + \chi_2\omega^2 + \dots, \quad (99)$$

and $\chi_0, \chi_1, \chi_2, \dots$ are all real. It follows that the energy dissipated is characterized by the absorptive cross-section

$$\sigma_{\text{abs}}(\omega) = \frac{4\pi\omega\text{Im}[\chi(\omega)]}{c}, \quad (100)$$

and at low frequencies

$$\sigma_{\text{abs}}(\omega) \approx \left(\frac{4\pi\chi^1}{c}\right)\omega^2, \quad (101)$$

which corresponds to an emissivity index $\beta = 2$ as $\omega \rightarrow 0$. The perhaps questionable assumption here is that there exists a circle of nonzero radius about the origin of the ω -plane where $\chi(\omega)$ has no singularities. If we postulate that there is an infinite number of poles of suitably decreasing strength whose accumulation point is $\omega = 0$, we may evade the conclusion that asymptotically as $\omega \rightarrow 0$, $\beta \rightarrow 2$. For an insightful discussion of how such low-frequency poles could arise, see C. Meny *et al.* [137].

19 Dust Polarization and Grain Alignment

The fact that interstellar dust grains are aligned was first seen through the polarization of starlight at optical frequencies in 1949 [77, 87, 88]. Since this discovery an abundant literature has been amassed elucidating numerous aspects of dust grain dynamics. The best bet solution to the alignment problem has evolved over the years as additional relevant physical effects were pointed out. It is unclear whether the current understanding will remain the last word on this subject. The most naive solution to the alignment problem would be some sort of compass needle type mechanism with some dissipation. However, it was discovered early on

that in view of the plausible magnitudes for the galactic magnetic field, such an explanation cannot work [214]. The theoretical explanation that has evolved involves detailed modeling of the rotational dynamics of the grains, which as we shall see below almost certainly rotate suprathermally.

For microwave observations of the primordial polarization of the CMB at ever greater sensitivity, the removal of contamination from polarized thermal dust emission is of the utmost importance. This fact is highlighted by the discussion of how to interpret the recent BICEP2 claim (discussed in Sec. 11.1) of a detection of a primordial B mode signal based on essentially a single frequency channel. This interpretation however seems unlikely given subsequent Planck estimates of the likely dust contribution [163]. The problem is that little data is presently available on polarized dust emission at microwave frequencies. Current models of polarized dust involve a large degree of extrapolation and are in large part guided by simplicity. From a theoretical point of view, polarized dust could be much more complicated than the simplest empirical modeling suggests. For example there is no *a priori* reason to believe that polarized emission from dust must follow the same frequency spectrum as its emission in intensity. It could well be that the weighting over grain types gives a different frequency dependence, or that as more precise dust modeling is called for, the need to include several species of dust with spatially nonuniform distributions will become apparent. Moreover, based on theoretical considerations, it is not clear that there should be a simple proportionality between polarization and the strength of the magnetic field. If the BICEP2 B mode signal is confirmed as a dust artefact, we could see ourselves in the coming years trying to detect values of the tensor-to-scalar ratio around $r \approx 10^{-3}$, which would require exceedingly accurate polarized dust removal from the individual frequency maps, and before this happens a wealth of new observational data on polarized dust emission will become available. If, on the other hand, a detection of B modes at a large value of r is made, as one tries to map out the precise primordial B mode spectrum, for example to measure n_T and thus check the consistency between $\mathcal{P}_S(k)$ and $\mathcal{P}_T(k)$, the need for accurate dust removal will likewise be great, but for slightly different reasons.

Since the observational inputs are likely to change, here we particularly emphasize the underlying physics of the alignment, which may be updated, but is likely to change less. The theoretical issues of dust alignment have so far not been widely discussed among those not specialized in the ISM (interstellar medium). Nevertheless, we believe that the questions raised will become increasingly relevant for CMB observations in the future, and this is why a thorough discussion is presented here.

We shall find that the alignment of interstellar dust grains is closely linked to the rotational dynamics of a dust grain. We therefore start with a study of the rotation of a dust grain. Mathematically, the simplest case to analyze is a prolate (needle-like) or oblate (flattened spherical) dust grain with an axis of azimuthal symmetry, which constitutes a symmetric top. In this case, the motions can be solved in terms of elementary functions. For the more general case of an asymmetric grain (where none of the three principal values of the moment of inertia tensor are equal) integration of the equations of motion in the absence of torques is more difficult, but can be achieved using Jacobian elliptic functions [234].

In the noninertial frame rotating with the dust grain, which is convenient because in this frame the moment of inertia tensor is constant in time, two types of inertial forces arise: (i) a centrifugal force, described by the potential $V_{ctr}(\mathbf{x})/m = -\Omega^2(t)\mathbf{x}^2 + (\boldsymbol{\Omega}(t) \cdot \mathbf{x})^2$, and (ii) a Coriolis force $\mathbf{F}_{cor}/m = -2\boldsymbol{\Omega}(t) \times \mathbf{v}$, which for our purposes is unimportant because

the velocities are negligible in the co-rotating frame. In order to understand the alignment process, we must model the solid as being elastic with dissipation included.

19.1 Why do dust grains spin?

A flippant answer to the above question might be: Why not? If we can associate a temperature with the three kinetic degrees of freedom of the dust grain, we would conclude that

$$\frac{1}{2}I\omega^2 \sim \frac{3}{2}k_{\text{B}}T_{\text{rot}}. \quad (102)$$

Early discussions of rotating dust grains supposed that the rotational degrees of freedom are subject to random torques, so that

$$\langle \mathbf{\Gamma} \rangle = 0. \quad (103)$$

Later it was realized that suprathreshold rotation is plausible, where the implied temperature of the rotation can greatly exceed the effective temperature of any of the other relevant degrees of freedom.

The question now arises what temperature one should use for T_{rot} . A natural candidate might be the kinetic temperature of the ambient gas T_{kin} . Indeed one expects molecules of the ambient gas to collide with the dust grains, and such collisions do provide random torques, causing the angular momentum to undergo a random walk accompanied by a dissipation mechanism, as must be present to prevent the angular velocity from diverging with time.

19.2 About which axis do dust grains spin?

This question has two parts. First, we may ask what is the alignment of the co-rotating internal (body) coordinates with respect to the angular momentum vector. Second, we may ask how the angular momentum aligns itself with respect to the inertial coordinates of the ambient space. In this Section, we consider only the first question, postponing the second question to a later section.

But for exceptional situations where two or more eigenvalues of the moment of inertia tensor coincide, the principal axes of moment of inertia tensor provide a natural set of axes for the dust grain, and we may order the eigenvalues so that $I_1 < I_2 < I_3$. We argue that the dust grain tends to align itself so that its I_3 axis is parallel to the angular momentum. This orientation of the grain minimizes the rotational energy subject to the constraint that the total angular momentum remains constant. If the grain starts in a state of random orientation, the grain wobbles. While \mathbf{L} remains constant, $\mathbf{\Omega}(t) = \mathbf{I}^{-1}(t)\mathbf{L}$ (expressed in inertial coordinates) does not, but rather fluctuates, exciting internal vibrational modes that dissipate. As the excess rotational energy is dissipated, an alignment as described above is achieved.^v The relevant question is how this time scale compares to other time scales of the grain rotation dynamics. It turns out that this time scale, which we denote τ_{I-L} , is short. In the equations

^vMuch to the dismay of NASA engineers, this is exactly what happened to the Explorer 1 rocket, the first US satellite launched in 1958 following Sputnik, due primarily to dissipation from its whisker antennas. The elongated streamlined cylinder was initially set in rotation about its long axis, but subsequently, after an initial wobble phase, ended up spinning about an axis at right angles in the body coordinates. Since then rotational stability, also relevant in ballistics, has become a carefully considered design issue for spacecraft.

that follow, we exploit the shortness of τ_{I-L} compared to the other relevant time scales. This hierarchy of time scales allows us to simplify the equations by excluding the degrees of freedom that describe the lack of alignment of the principal axis of maximum moment of inertia from \mathbf{L} , leading to a considerable simplification of the formalism.

19.3 A stochastic differential equation for $\mathbf{L}(t)$

Mathematically, we may describe the combined effects of the torque from random collisions and its associated damping through the coherent torque using a stochastic differential equation of the form

$$\dot{\mathbf{L}}(t) = -\alpha \left(\mathbf{L}(t) - \bar{L} \frac{\mathbf{L}(t)}{|\mathbf{L}(t)|} \right) + \mathbf{\Gamma}_{\text{ran}}(t). \quad (104)$$

In this equation, the torque described by the first term is coherent with respect to the body coordinates of the dust grain. Later we shall also consider torques that are coherent with respect to the ambient inertial coordinates, which must be modeled in a different way. Here the stochastic Gaussian forcing term has the expectation values

$$\begin{aligned} \langle \Gamma_{\text{ran},i}(t) \rangle &= 0, \\ \langle \Gamma_{\text{ran},i}(t) \Gamma_{\text{ran},j}(t') \rangle &= \mu_L \delta_{ij} \delta(t - t'), \end{aligned} \quad (105)$$

where the angular momentum diffusion coefficient has units $[\mu_L] = (\text{Torque})^2/(\text{Time})$.

Let us analyze the stationary ensemble defined by the above equation—in other words, the probability function $p(\mathbf{L})$ toward which the biased random walk defined by the above equation evolves after a long period of time. In the low-temperature limit, $|\mathbf{L}| \approx \bar{L}$, with negligible fractional fluctuations, and the direction of the angular momentum vector $\hat{\mathbf{n}}_{\mathbf{L}} = \mathbf{L}(t)/|\mathbf{L}(t)|$ follows a random walk on the surface of the sphere with diffusion coefficient $\mu_{\hat{n}} = \mu_L/\bar{L}^2$. In the opposite high temperature limit, the \bar{L} term is a sideshow or small correction, and the main effect is the competition between the first and second terms leading to a thermal ensemble, which for an isotropic moment of inertial tensor would take the form

$$p(\mathbf{L}) = \left(\frac{\beta}{2\pi} \right)^{3/2} \exp[-\beta \mathbf{L}^2], \quad (106)$$

where $\beta = \alpha/\mu_L$. Without other sources of dissipation or random torques, we expect that $\beta = 1/(2k_B T_{\text{kin}} I_{\text{max}})$ where I_{max} is the largest eigenvalue of the moment of inertia tensor of the particular grain being modelled and T_{kin} is the kinetic temperature of the ambient gas. It is straightforward to generalize Eq. (106) to the intermediate case. It was however later noted that a number of mechanisms exist for which $\langle \mathbf{\Gamma} \rangle \neq 0$, which can give rise to what is known as “suprathermal rotation” [193]—that is, rotation at an angular velocity larger than any temperature associated with the other degrees of freedom interacting with the dust grain.

19.4 Suprathermal rotation

To see how such *suprathermal rotation* might come about, consider the caricature of a dust grain as sketched in Fig. 24. Let us assume that the dust grain emits radiation isotropically in the infrared, but that in the visible and UV bands radiation is absorbed or reflected by the

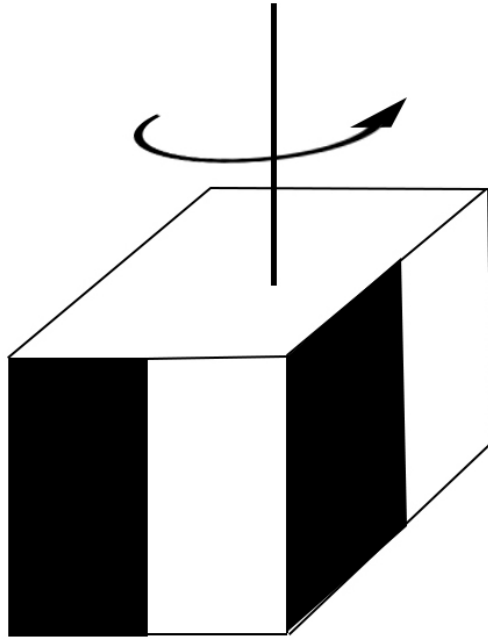


Figure 24: **Coherent torques from grain radiation pressure.**

surfaces indicated in the figure. Let us further assume an isotropic visible or UV illumination. The blackened (perfectly absorbing) faces suffer a radiation pressure equal to half that of the mirrored surfaces, giving a coherent torque in the direction indicated in the figure. The presence of two distinct temperatures, reminiscent of a thermal engine, is crucial to avoid thermal equilibrium for the rotational degree of freedom. As in the thermodynamics of an engine, there is a heat flow from a hotter temperature to a colder temperature with some of the energy being siphoned off in the form of work exerted on the three rotational degrees of freedom of the dust grain. Other possibilities for coherent torques result from photoelectron emission at privileged sites and the catalysis of molecular hydrogen on favored sites on the grain surface. In the former case, the incident UV photon is almost pure energy due to its masslessness, but the emitted electron carries substantial momentum for which there is a recoil. Molecular hydrogen forms almost exclusively through catalysis on a grain surface. Unlike in ordinary chemistry where truly two-body collisions are an exception and activation barriers prevent reactions from establishing equilibrium, for molecular hydrogen formation in the cold interstellar medium, the bottleneck is the lack of three-body collisions and the lack of an efficient mechanism for carrying away the excess energy, so that the hydrogen atoms combine rather than simply bouncing off each other. In principle, the energy can be lost radiatively, but the rate for this is too slow. Given that 4.2eV is liberated, the recoil at selected sites can produce a substantial coherent torque on the grain.

19.5 Dust grain dynamics and the galactic magnetic field

Much of the dust grain rotational dynamics does not single out any preferred direction. To explain the polarization of starlight and of the thermal dust emission at microwave frequencies, some mechanism is needed that causes the dust grains to align themselves locally at least along

a common direction such as that of the magnetic field.

19.5.1 Origin of a magnetic moment along \mathbf{L}

Two effects generate a magnetic moment along the axis of \mathbf{L} :

(i) **Inhomogeneous electric charge distribution in the dust grain.** The second moment of the electric charge density about the principal axis of the largest eigenvalue of the moment of inertia tensor (denoted z) induces a magnetic dipole moment as the grain rotates about this axis, according to

$$\boldsymbol{\mu} = \hat{\mathbf{z}}\Omega_z \int d^3r \rho_e(\mathbf{r})(x^2 + y^2), \quad (107)$$

where $\rho_e(\mathbf{r})$ is the electrostatic charge density of the dust grain. In general, and particularly when the grain structure is amorphous, the net charge density is nonvanishing, so the integral above does not vanish. This effect is known as the *Rowland effect*.

(ii) **The Barnett effect.** Minimizing the free energy tends to align the free spins of a rotating body with the direction of rotation. In nonferromagnetic substances this effect is usually negligible, but rotating dust grains present an extreme environment because of their minute size and isolation from their environment. Interstellar dust grains are among the fastest rotating macroscopic objects known.

To understand the origin of the Barnett effect, consider an isolated rotating body, whose conserved total angular momentum may be decomposed into two parts

$$\mathbf{L}_{\text{tot}} = \mathbf{L}_{\text{bulk}} + \mathbf{S}_{\text{free}}. \quad (108)$$

We consider the energetics of the exchange of angular momentum between the bulk and spin degrees of freedom. We assume the spins to be free neglecting any interactions between them. In this case, the Hamiltonian for the system is

$$H = \frac{\mathbf{L}_{\text{bulk}}^2}{2I} = \frac{(\mathbf{L}_{\text{tot}} - \mathbf{S})^2}{2I}, \quad (109)$$

and retaining only the term linear in the spin, we obtain

$$H = -\boldsymbol{\Omega} \cdot \mathbf{S}, \quad (110)$$

where $\boldsymbol{\Omega}(t) = \mathbf{I}^{-1}(t)\mathbf{L}$ is the angular rotation velocity. The spins want to align themselves with the rotation to lower the rotational energy [115]. So far we have not included any terms opposing complete alignment, so at $T = 0$ complete alignment would result with $\mathbf{S} = S_{\text{available}}\boldsymbol{\Omega}/|\boldsymbol{\Omega}|$. But at finite temperature entropic considerations oppose such alignment, and it is the free energy $F = H - TS(\mathbf{S})$ or

$$F(\mathbf{S}; \boldsymbol{\Omega}) = -\boldsymbol{\Omega} \cdot \mathbf{S} + aT\mathbf{S}^2 \quad (111)$$

that is minimized. Far from saturation, when the degree of alignment is small, this quadratic term provides a good approximation to the entropy of the spin system.

19.6 Magnetic precession

Having established that a spinning dust grain has a magnetic moment parallel to its angular momentum vector, which is aligned with the principal axis of the largest eigenvalue of the moment of inertia tensor, we now consider the effect of the torque resulting from the interaction with the ambient magnetic field. The interaction Hamiltonian is

$$H = -\boldsymbol{\mu} \cdot \mathbf{B}, \quad (112)$$

from which it follows that

$$\dot{\mathbf{L}} = \boldsymbol{\mu} \times \mathbf{B} = \gamma_m \mathbf{L} \times \mathbf{B}. \quad (113)$$

In other words, the angular momentum vector precesses at a frequency $\omega_{\text{prec}} = \gamma_m |\mathbf{B}|$ around the magnetic field. Under this precession, the angle between \mathbf{L} and $\boldsymbol{\mu}$ remains constant, meaning that this effect neither aligns nor disaligns the grain with respect to the local magnetic field direction.

We estimate the time scale of this precession. Let \mathcal{S} denote the spin polarization density (angular momentum per unit volume), which under saturation (i.e., all free spins aligned) would have a magnitude \mathcal{S}_{sat} , whose order of magnitude can be estimated by assuming approximately Avogadro's number N_A of spins having a magnitude \hbar in a cubic centimeter volume, giving $\mathcal{S}_{\text{sat}} \approx O(1)(4 \times 10^{-4}) \text{erg} \cdot \text{s} \cdot \text{cm}^{-3}$. We obtain the following free energy density (per unit volume):

$$F_0(\mathbf{S}; T) = \frac{1}{2} (k_B T) \mathcal{N}_{\text{spin}} \left(\frac{\mathcal{S}}{\mathcal{S}_{\text{sat}}} \right)^2. \quad (114)$$

Here for a paramagnetic substance the order of magnitude for $\mathcal{N}_{\text{spin}}$ might be around 10^{24}cm^{-3} but for a ferromagnetic substance could be much smaller, corresponding to the density of domains. Minimizing the free energy with respect to \mathcal{S} gives the spin polarization density

$$\mathcal{S} = \frac{\mathcal{S}_{\text{sat}}^2}{(k_B T) \mathcal{N}_{\text{spin}}} = I_S \boldsymbol{\Omega}. \quad (115)$$

We express the constant of proportionality as if it were a moment of inertia because it has the same units.

$$\begin{aligned} \frac{I_S}{I_L} &\approx \frac{\mathcal{N}_{\text{free}} \hbar^2}{k_B T \rho a^2} \\ &\approx (3 \times 10^{-5}) \left(\frac{N_{\text{free}}}{10^{24} \text{cm}^{-3}} \right) \left(\frac{100 \text{K}}{T} \right) \left(\frac{3g \text{cm}^{-3}}{\rho} \right) \left(\frac{10 \text{nm}}{a} \right)^2. \end{aligned} \quad (116)$$

19.6.1 Barnett dissipation

The coupling in the Barnett effect between the bulk and spin angular momenta does not act instantaneously. Rather as the instantaneous angular velocity $\boldsymbol{\Omega}(t)$ changes, there is a lag in the response of $\mathbf{S}(t)$. In his landmark 1979 paper [193], Purcell pointed out that this lag would help align the body coordinates so that the axis of maximum moment of inertia is parallel to the angular momentum vector. Purcell coined the name *Barnett dissipation* for this effect, whose magnitude is greater than the mechanical dissipation mentioned above.

Two types of free spins participate in the Barnett effect: the electronic spins and the nuclear spins. The electronic spins are much more relevant for establishing a magnetic moment along \mathbf{L} as discussed above in Sec. 19.5.1 because electronic magnetic moments are larger than nuclear magnetic moments by a factor of about (m_p/m_e) . But for dissipation, this strong coupling is a liability. The nuclear spins contribute predominantly to Barnett dissipation because of their longer lag time.

Mathematically, the coupled equations

$$\begin{aligned}\dot{\mathbf{S}}(t) &= -\gamma(\mathbf{S}(t) - \alpha\mathbf{\Omega}(t)), \\ \dot{\mathbf{L}}(t) &= +\gamma(\mathbf{S}(t) - \alpha\mathbf{\Omega}(t)),\end{aligned}\tag{117}$$

describe this effect. We may integrate out $\mathbf{S}(t)$ to obtain the following equation in inertial coordinates for the torque on \mathbf{L} resulting from the exchange of angular momentum between the bulk and spin degrees of freedom

$$\dot{\mathbf{L}}(t) = -\alpha\gamma\mathbf{\Omega}(t) + \alpha\gamma^2 \int_0^\infty d\tau \exp[-\gamma\tau]\mathbf{\Omega}(t - \tau).\tag{118}$$

To calculate how fast this exchange of angular momentum aligns the axis of maximum moment of inertia with the angular momentum vector, we calculate the averaged rotational energy loss rate of the bulk degrees of freedom retaining only secular contributions. This calculation is simpler than keeping track of torques. The degree of alignment of $\mathbf{\Omega}(t)$ with the axis of maximum moment of inertia is a function of the rotational energy in the bulk rotational degrees of freedom. The instantaneous power transferred from the bulk rotation to the spin degrees of freedom is given by

$$\begin{aligned}P_{\text{loss}}(t) &= \mathbf{\Omega}(t) \cdot \dot{\mathbf{L}}(t) = -\mathbf{\Omega}(t) \cdot \dot{\mathbf{S}}(t) \\ &= -\gamma I_s \mathbf{\Omega}(t) - \gamma \left\{ \mathbf{\Omega}(t) - \gamma \int_0^\infty dt' \exp[-\gamma t'] \mathbf{\Omega}(t - t') \right\},\end{aligned}\tag{119}$$

and to obtain the averaged or secular contribution, we decompose $\mathbf{\Omega}(t)$ into harmonic components of amplitude $\mathbf{\Omega}_a$ and frequency ω_a , so that

$$\left\langle \mathbf{\Omega}(t) \cdot \left\{ \mathbf{\Omega}(t) - \gamma \int_0^\infty dt' \exp[-\gamma t'] \mathbf{\Omega}(t - t') \right\} \right\rangle = \frac{1}{2} \sum_a \mathbf{\Omega}_a^2 \frac{\omega_a^2}{\gamma^2 + \omega_a^2}.\tag{120}$$

It follows that

$$\langle P_{\text{loss}} \rangle = -\frac{1}{2} I_s \sum_a \mathbf{\Omega}_a^2 \frac{\omega_a^2}{\gamma^2 + \omega_a^2}.\tag{121}$$

We see that the stationary component (with $\omega_a = 0$) does not contribute to the loss but the precessing components dissipate.

We obtain an order of magnitude for the alignment rate by assuming that $(\delta I)/I \approx O(1)$ and that except for the stationary component $\omega_a \approx \omega_{\text{max}} = L/I_{\text{max}}$, so that the excess energy is approximately

$$E_{\text{excess}} \approx O(1) I_{\text{max}} \omega_{\text{max}}^2 \sin^2 \theta\tag{122}$$

where θ is the disalignment angle, and the rate of dissipation is approximately

$$\bar{P}_{\text{loss}} \approx O(1)\gamma I_S \omega_{\text{max}}^2 \frac{\omega_{\text{max}}^2}{\gamma^2 + \omega_{\text{max}}^2} \sin^2 \theta, \quad (123)$$

so that

$$\gamma_{\text{align}} \approx \gamma \frac{I_S}{I_3} \frac{\omega_{\text{max}}^2}{\gamma^2 + \omega_{\text{max}}^2}. \quad (124)$$

The action of the imperfect coupling of the spins to the bulk angular momentum and bulk rotational velocity is somewhat analogous to that of a harmonic balancer on a rotating shaft (such as a crankshaft), a common device in mechanical engineering. Here however the weakly and dissipatively coupled flywheel is replaced by the internal spin degrees of freedom.

19.7 Davis-Greenstein magnetic dissipation

If a grain rotates with an angular velocity along the direction of the magnetic field, in the frame co-rotating with the grain, the magnetic field is time independent. However the component of the angular velocity in the plane normal to the magnetic field $\boldsymbol{\Omega}_{\perp}$ gives rise to an oscillating magnetic field of angular frequency Ω_{\perp} . In general, the magnetic susceptibility at nonzero frequency has a nonzero imaginary part $\chi_{m,i}$, where

$$\chi_m(\omega) = \chi_{m,r}(\omega) + i\chi_{m,i}(\omega). \quad (125)$$

The lag in the response of the magnetization to the applied driving field gives rise to dissipation accompanied by a torque that tends to align (or antialign) the spin with the magnetic field. This effect is known as the Davis-Greenstein mechanism [40].

The alignment tendency of the Davis-Greenstein mechanism may be described by the pair of equations

$$\dot{\mathbf{L}}_{\perp} = -\frac{1}{\tau_{DG}} \mathbf{L}_{\perp}, \quad \dot{\mathbf{L}}_{\parallel} = 0, \quad (126)$$

where the decay time τ_{DG} indicates the time scale of the Davis-Greenstein relaxation process. In deriving this simple form, we have assumed that $\tau_{\text{prec}} \ll \tau_{DG}$, so that we may average over many precessions. We also assume that the alignment with the axis of maximum moment of inertia likewise is very fast. If these assumptions do not apply, an averaged equation of the simple form above does not hold, and these effects need to be analyzed simultaneously.

A key issue in evaluating the viability of the Davis-Greenstein mechanism is the frequency of reversals of the direction of the coherent torque, termed ‘‘cross-over’’ events in the literature. If we consider for example coherent torques from the formation of molecular hydrogen at a small number of catalysis sites on the grain surface, the orientation of this torque depends on the structure of the outermost surface atomic monolayer, and its structure is likely to change as new layers are deposited or as old layers are eroded away. Consequently, the long term coherence time of the ‘‘coherent’’ torque is uncertain. Under the assumption that the alignment of the body coordinates with the angular momentum is fast, it is the evolution of the coherent torque projected onto the axis of maximum moment of inertia that matters. While the grain rotates suprathermally, its direction is relatively stable against random perturbing

torques, but when its rotation velocity is in the process of changing sign and of the same order as the would-be “thermal” rotation velocity, the grain is particularly susceptible to changing orientation as a result of random torques as discussed in detail in Refs. [213] and [116].

In deciding whether τ_{DG} is too long for producing a significant degree of alignment, we must consider competing effects that tend to disalign the grains, which modify the above equation to become a stochastic differential equation of the form

$$\dot{\mathbf{L}} = -\frac{1}{\tau_{DG}} (\mathbf{L} - \hat{\mathbf{e}}_B(\hat{\mathbf{e}}_B \cdot \mathbf{L})) - \frac{1}{\tau_{rel}} (\mathbf{L} - \bar{L}\hat{\mathbf{e}}_L) + \frac{\bar{L}}{\tau_{rand}^{1/2}} \mathbf{n}(t) \quad (127)$$

where $\hat{\mathbf{e}}_B = \mathbf{B}/|\mathbf{B}|$, $\hat{\mathbf{e}}_L = \mathbf{L}/|\mathbf{L}|$, and $\mathbf{n}(t)$ is a normalized white noise source whose expectation value is given by

$$\langle n_i(t) n_j(t') \rangle = \delta(t - t'). \quad (128)$$

If $\tau_{rel} \lesssim \tau_{rand}$, in the absence of a magnetic field, \mathbf{L} undergoes a random walk on the surface of a sphere of radius \bar{L} . If $\tau_{DG} \ll \tau_{rand}$ the magnetic dissipation is strong enough to bring about almost complete alignment. However if, on the other hand, $\tau_{DG} \gg \tau_{rand}$, the magnetic dissipation leads to a negligible amount of alignment.

19.8 Alignment along \mathbf{B} without Davis-Greenstein dissipation

Because of the magnetic precession discussed in Sec. 19.6, an average alignment with the magnetic field direction (or more precisely with a direction very close to the magnetic field direction) can be obtained if there is a tendency toward alignment with some other direction characterized by a time scale t_{align} where $t_{align} \gg t_{prec}$. The effect of precession about an axis $\boldsymbol{\Omega}$ (presumably along $\pm\mathbf{B}$) in competition with alignment about another direction $\hat{\mathbf{n}}$ is described by the ordinary differential equation

$$\dot{\mathbf{L}} = \boldsymbol{\Omega} \times \mathbf{L} - \gamma(\mathbf{L} - \hat{\mathbf{n}}\bar{L}). \quad (129)$$

This equation has two time scales: Ω^{-1} and γ^{-1} . We are primarily interested in fast precession (i.e., $\Omega \gg \gamma$). Equation (129) is a linear equation whose solution decomposes into a stationary part and transient spiralling in to approach the stationary attractor. We solve

$$\begin{pmatrix} -\gamma & +\Omega & 0 \\ -\Omega & -\gamma & 0 \\ 0 & 0 & -\gamma \end{pmatrix} \begin{pmatrix} L_{\perp 1} \\ L_{\perp 2} \\ L_{\parallel} \end{pmatrix} = -\gamma\bar{L} \begin{pmatrix} \hat{n}_{\perp 1} \\ \hat{n}_{\perp 2} \\ \hat{n}_{\parallel} \end{pmatrix}, \quad (130)$$

so that

$$\begin{aligned} L_{\perp 1} &= \frac{\gamma^2}{\gamma^2 + \Omega^2} \bar{L} \hat{n}_{\perp 2} - \frac{\gamma\Omega}{\gamma^2 + \Omega^2} \bar{L} \hat{n}_{\perp 1}, \\ L_{\perp 2} &= \frac{\gamma^2}{\gamma^2 + \Omega^2} \bar{L} \hat{n}_{\perp 1} + \frac{\gamma\Omega}{\gamma^2 + \Omega^2} \bar{L} \hat{n}_{\perp 2}, \\ L_{\parallel} &= \bar{L} \hat{n}_{\parallel}. \end{aligned} \quad (131)$$

In the fast precession regime of most interest to us, $\mathbf{L} = \bar{L}\boldsymbol{\Omega}(\boldsymbol{\Omega} \cdot \hat{\mathbf{n}})/\Omega^2$, with corrections suppressed by a factor (γ/Ω) . The precession has no alignment tendency of its own, but if the

precession period is shorter than the time scale of the alternative alignment mechanism, the precession acts to suppress alignment in the plane normal to $\boldsymbol{\Omega}$.

If it turns out that radiative torques combined with the fast precession described above is the solution to the alignment problem, a number of interesting observational consequences follow. Blind data analysis might suggest that one should be able to predict polarization from the thermal dust emission intensity combined with a map of the galactic magnetic field, perhaps deduced from rotation measures and synchrotron emission. However, if the above mechanism is correct, this procedure will not work, even with a three-dimensional model of the unpolarized dust emission and galactic magnetic field. In the above equations, provided that the galactic magnetic field is strong enough, its direction serves to define the direction of the grain alignment but its precise magnitude has little relevance. The above mechanism can also accommodate a large amount of small-scale power in the polarized dust signal, even if both the galactic magnetic field and the dust density are smooth. One might expect the field characterizing the radiative alignment tendency $\bar{L}(\mathbf{x})\hat{\mathbf{n}}(\mathbf{x})$ to include an appreciable component varying on small scales.

19.9 Radiative torques

Electromagnetic radiation scattered or absorbed by the dust grain in general exerts a torque on the dust grain, as already modeled in Sec. 19.4 for isotropic illumination, which is simpler because the torque direction is constant in the co-rotating body coordinates. Here we generalize to anisotropic illumination.

Let $\boldsymbol{\Gamma}(\nu, \hat{\mathbf{n}})$ expressed in body coordinates be the torque exerted on a dust grain by monochromatic electromagnetic radiation of frequency ν and unit spectral radiance propagating in the $\hat{\mathbf{n}}$ direction. For an illumination described by the spectral radiance $I(\nu, \hat{\mathbf{n}})$, the torque exerted on the dust grain in inertial coordinates is given by

$$\boldsymbol{\Gamma}(t) = \int_0^\infty d\nu \int_{S^2} d\hat{\mathbf{n}} \boldsymbol{\Gamma}(\nu, \mathcal{R}(t)\hat{\mathbf{n}}) I(\nu, \hat{\mathbf{n}}). \quad (132)$$

The complication here arises from the need to include both inertial and co-rotating body coordinates, related by the transformation $\mathbf{x}_{\text{iner}} = \mathcal{R}(t)\mathbf{x}_{\text{body}}$.

Assuming that the time scale for radiative torques is long compared to the moment of inertia alignment time scale τ_{I-L} , we may take $\boldsymbol{\Omega}$ to be aligned with \mathbf{L} and define an averaged kernel $\bar{\boldsymbol{\Gamma}}(\nu, \hat{\mathbf{n}}_I; \hat{\mathbf{n}}_L)$, defined as

$$\bar{\boldsymbol{\Gamma}}(\nu, \hat{\mathbf{n}}_I; \hat{\mathbf{n}}_L) = \frac{1}{2\pi} \int_0^{2\pi} d\chi \boldsymbol{\Gamma}(\nu, \mathbf{R}_{(\chi, \hat{\mathbf{n}}_L)}\hat{\mathbf{n}}_I), \quad (133)$$

where $\mathbf{R}_{(\chi, \hat{\mathbf{n}}_L)}$ represents a rotation by χ about the $\hat{\mathbf{n}}_L$ axis. Apart from a few general observations, little can be said about the form and properties of the radiative torque kernel, which differ from grain to grain. At very long wavelengths—that is, long compared to the size of the dust grain—it is a good approximation to treat the grain as a dipole (as one does for Rayleigh scattering). In the dipole approximation there are no torques. Therefore, (a/λ) serves as an expansion parameter for which the torque approaches zero as this parameter tends toward zero. Likewise a spherical grain gives a vanishing torque at any frequency as the result of symmetry arguments.

Convolving the incident radiation intensity $I(\nu, \hat{\mathbf{n}}_{\mathbf{I}})$ with this kernel, we obtain the angle-averaged torque $\mathbf{\Gamma}_{\text{tot,rad}}(\hat{\mathbf{n}}_{\mathbf{L}})$. If there were no magnetic field, we could incorporate the torque above into the previously derived stochastic differential equation for the evolution of \mathbf{L} [Eq. (104)] to obtain

$$\dot{\mathbf{L}}(t) = -\beta\mathbf{L}(t) + \beta\bar{L}\frac{\mathbf{L}(t)}{|\mathbf{L}(t)|} + \mathbf{\Gamma}_{\text{tot,rad}}\left(\frac{\mathbf{L}(t)}{|\mathbf{L}(t)|}\right) + \mathbf{n}_{\text{ran}}(t), \quad (134)$$

where a coherent torque in body coordinates has been included as well. The above equation describes a random walk $\mathbf{L}(t)$ in three-dimensional angular momentum space. Owing to the stochastic random torque noise term, the rotational degree of freedom loses memory of its initial state after some characteristic decay time t_{ran} , after which its state can be described by a probability distribution $p(\mathbf{L})$ calculable based on the above equation. The stochastic equation above has the general form

$$\dot{\mathbf{L}} = \mathbf{v}(\mathbf{L}) - \mathbf{n}(t), \quad (135)$$

for which the associated Fokker-Planck equation describing the evolution of the probability density is

$$\frac{\partial p(\mathbf{L})}{\partial t} = \nabla^2 p(\mathbf{L}) + \nabla \cdot (p(\mathbf{L})\mathbf{v}(\mathbf{L})). \quad (136)$$

With the magnetic field included, we add the magnetic precession term to obtain

$$\dot{\mathbf{L}}(t) = -\beta\mathbf{L}(t) + \beta\bar{L}\frac{\mathbf{L}(t)}{|\mathbf{L}(t)|} + \mathbf{\Gamma}_{\text{tot,rad}}\left(\frac{\mathbf{L}(t)}{|\mathbf{L}(t)|}\right) + \gamma_{\text{mag}}\mathbf{L} \times \mathbf{B} + \mathbf{n}_{\text{ran}}(t), \quad (137)$$

where the constant γ_{mag} relates the magnetic moment to the angular momentum according to $\boldsymbol{\mu}_B = \gamma_{\text{mag}}\mathbf{L}$.

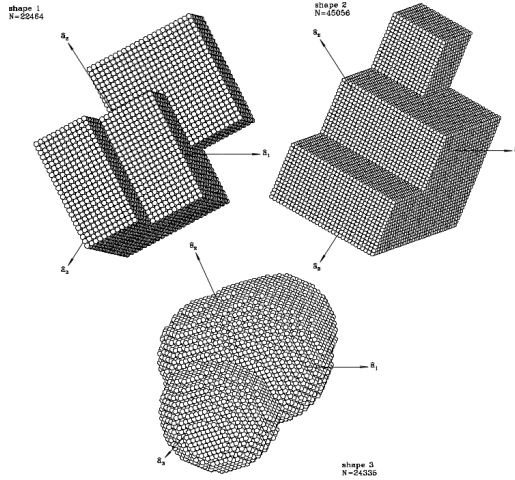


Figure 25: **Selection of grain shapes for studying radiative torques.** In Ref. [53], Draine and Weingartner calculated the radiative torque on a dust grain as a function of frequency ν and incident photon direction $\hat{\mathbf{n}}$ for the three grain shape illustrated above. (*Credit: B. Draine and J. Weingartner*)

When $t_{\text{ran}}, t_{\text{rad}} \gg t_{\text{prec}}$, it is possible to reduce the dimension of the stochastic differential equation to two dimensions, namely the angular velocity ω and the angle θ_{BL} between the vectors \mathbf{L} and \mathbf{B} , obtaining

$$\dot{\theta}_{BL} = F(\theta_{BL}, \omega) + n_{\theta}(t), \quad \dot{\omega} = G(\theta_{BL}, \omega) + n_{\omega}(t). \quad (138)$$

Unfortunately, very little can be said about the form of the functions $F(\theta_{BL}, \omega)$ and $G(\theta_{BL}, \omega)$, which depends on the detailed grain shapes and other properties. Draine and Weingartner [53, 54, 231] studied three possible irregular grain shapes (shown in Fig. 25), calculating numerically the radiative torque as a function of illumination direction and frequency. Then assuming a certain anisotropic illumination, they calculated the functions F and G in Eq. (138) and studied the solutions to this equation numerically establishing the orbits in the absence of noise. Their simulations conclude that radiative torques can provide a plausible alignment mechanism.

The proposal that radiative torques resulting from anisotropic illumination align the interstellar dust grains with the magnetic field offers a promising alternative to the Davis-Greenstein magnetic dissipation mechanism whose characteristic time scale may be too long to provide the needed degree of alignment. However, its viability is hard to evaluate given our ignorance concerning the shapes of the dust grains. Without such shape information, the best case that can be put forward in favor of this scenario based on radiative torques and anisotropic illumination is to show that some candidate shapes exist that give the right orders of magnitude combined with the argument that the Davis-Greenstein scenario cannot account for the data. It is discouraging that it is not possible to formulate precise predictions for the radiative torque scenario. The origin of grain alignment seems to remain an open question.

19.10 Small dust grains and anomalous microwave emission (AME)

The thermal emission of interstellar dust grains discussed above was based on the assumption that its thermal state may be characterized by a mean temperature (around 20 K) and that fluctuations about this temperature subsequent to the absorption of an UV photon constitute a negligible correction. If a dust grain is sufficiently large, this is a good approximation, but for small molecules an FUV (far ultraviolet) photon can raise the grain temperature momentarily by an order of magnitude or more, allowing emission in bands where there would be almost no emission for a grain at its average temperature. The bulk of the energy absorbed from the UV photon is then rapidly re-emitted through IR fluorescence as the molecule rapidly cools back down to its mean temperature. Hints of such emission requiring a temperature significantly above the mean temperature were noted through the observation of aromatic infrared emission features consistent with C–H bonds on the edge of an aromatic molecule—that is, around 3.3 and 11.3 microns [55, 119]. Later, analysis of the IRAS dust maps showed that a significant fraction of the UV photons absorbed through extinction were re-emitted in bands of wavelength shorter than $60\ \mu$, where under the assumption of a reasonable average temperature and a modified blackbody law there should be no emission [190]. As a consequence, the dust models were revised to extend the size distribution to include small grains thought to be PAHs as a result of the infrared emission features described above. PAHs (polycyclic aromatic hydrocarbons) are essentially small monolayer planar sheets of graphite with hydrogen frills on their edges.

A template for the small grain population can be constructed using maps of infrared emission at $\lambda \lesssim 60\ \mu$ where the thermal emission from large grains does not contribute. Since the short wavelength emission from the dust grains is proportional to the local FUV flux density, these templates can in principle be improved by dividing the local FUV flux density to obtain a better map of the projected small dust grain column density, which in turn can be correlated with the AME (anomalous microwave emission) at low frequencies.

It was also pointed out that such a population of very small dust grains would be expected to rotate extremely rapidly, giving rise to electric dipole emission at its rotation frequency and possibly at higher harmonics, since $P_e \sim \mu_E \omega^4$ and $\omega^2 \approx (k_B T_{\text{rot}})/ma^2$ in the absence of suprathermal rotation [50, 51, 6]. The possibility of magnetic dipole emission from small rotating grains has also been investigated [52].

Observationally, emission at low frequencies, where diffuse thermal dust emission should be minuscule, was found correlated with high frequency dust maps [42, 106, 120]. Such emission would be consistent with dipole emission from small rapidly rotating dust grains, as described above. As an alternative explanation for such a correlation, it was proposed that regions of free-free emission could be correlated with regions of thermal dust emission. However, this low frequency excess was found not to be correlated with $H\alpha$ line emission, which serves as a tracer of free-free emission. One possibility to weaken such a correlation would be to postulate an extremely high temperature, so that $\Gamma_{\text{free-free}}(T)/\Gamma_{H\alpha}$ is large. However, it was found that such a high temperature would require an implausible energy injection rate to prevent this phase from cooling.

The spectrum of anomalous microwave emission, presumably from spinning dust, has been measured by taking spectra in targeted regions having a large contribution from AME and subtracting the expected synchrotron, free-free, thermal dust, and primordial CMB signals [229, 86]. Figure 26 shows the spectrum thus obtained. The observed fall-off at low ν disfavors

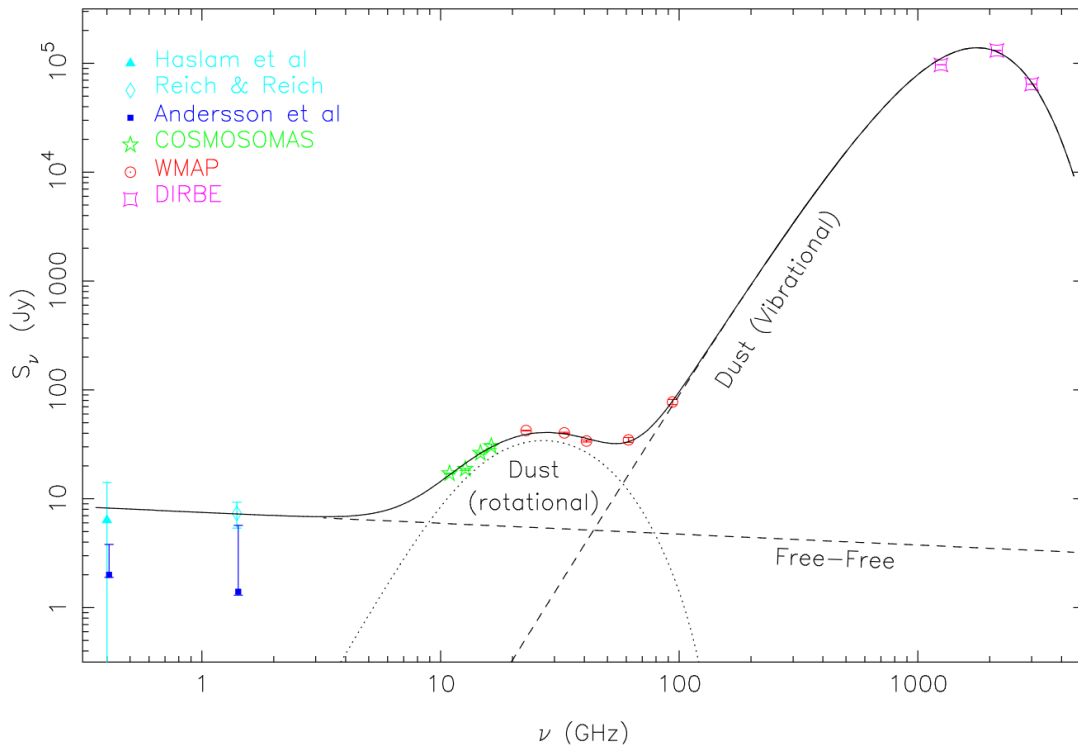


Figure 26: **Consistency of anomalous microwave emission with spinning dust.** The multi-frequency observations shown here were taken for a molecular cloud believed to have strong anomalous dust emission. We observe that given the shape a linear combination of thermal dust and free-free emission cannot explain the observed shape. However, if an anomalous dust component with the spectral shape predicted by Draine and Lazarian for electric dipole emission from spinning dust is included (dotted curve), a reasonable fit may be obtained. For more details, see Ref. [229]. (*Credit: COSMOMAS Collaboration*)

the hypothesis of free-free emission correlated with thermal dust emission as the origin of the anomalous emission, because in that case, the spectrum of the residual should rise as ν is lowered.

Most theoretical studies have assumed that the small grains do not become aligned with the galactic magnetic field, but alignment mechanisms for this grain population have not yet been investigated in detail. Observational limits on the anomalous microwave emission constrain the degree of polarization to less than a few per cent [198].

20 Compact Sources

The above processes pertain primarily to diffuse galactic emission, which contaminates the primordial CMB signal most severely at low multipole number ℓ . On smaller scales, however, compact sources become more of a concern and eventually become the dominant contribution at all frequencies. We use the term “compact” to denote both unresolved point sources and partially resolved, localized sources.

The angular power spectrum of point sources distributed according to a Poissonian dis-

tribution would scale with multipole number as ℓ^0 . If ignoring the structure of the acoustic oscillations, one approximates the primordial CMB spectrum as having the shape ℓ^{-2} , one would conclude that compact sources rapidly take over at high ℓ . Because of Silk damping combined with the smoothing from the finite width of the last scattering surface, the fall-off of the CMB at large ℓ is even more rapid. The fact that point sources are clustered rather than distributed in Poissonian manner causes the point source power spectrum to be clustered, leading to an excess of power at small ℓ compared to an ℓ^0 power law.

20.1 Radio galaxies

Section 16 described the physical process of synchrotron emission, emphasizing its contribution to the diffuse emission from our own galaxy. However the same process is also at work in galaxies other than our own, and in particular in the rare, but highly luminous radio galaxies at high redshift, extreme processes fueled by a central black hole give rise to intense emission in many bands, including synchrotron emission in the radio and microwave bands. For our purposes, the most salient and relevant feature of these sources is their inverted spectrum. For a detailed survey of radio sources, see Ref. [221]. Since each source differs slightly in its spectral properties, the strategy for dealing with these sources is to mask out the brightest sources and then model the residual arising from the remaining unmasked sources.

20.2 Infrared galaxies

In Sec. 18, we discussed at length the contamination from thermal emission from the interstellar dust in our galaxy. Thermal dust emission, however, is not restricted to our galaxy. All galaxies contribute some thermal dust emission. However, the galaxies at high redshift in which star formation is occurring at a rapid rate contribute predominantly to the extragalactic thermal dust emission in the microwave bands of interest to us. In fact, most of the energy of the radiation from these galaxies in which intense star formation is taking place is emitted in the infrared, because the light and UV emitted is absorbed by dust, which becomes heated and in turn re-emits in the infrared.

Some of these infrared galaxies are resolved by current observation. Others remain unresolved by present day observations and these are attributed to the diffuse infrared background. These infrared galaxies do not all emit with the same frequency spectrum, in part because they are spread over a wide range of redshifts. For the early discovery papers on the CIB (cosmic infrared background) from COBE see Refs. [191, 82] and [64]. For more recent observations from Planck, see Ref. [159].

21 Other Effects

21.1 Patchy reionization

In Sec. 7.5, we idealized the reionized hot electron gas extending from intermediate redshifts to today as being isotropically distributed so that the free electron density depends only on redshift. Such a reionization scenario is implausible but provides a good approximation for the effect of reionization on the CMB power spectrum at low ℓ . In a more realistic reionization scenario, the universe becomes reionized in an inhomogeneous manner. As the first stars and

quasars form, their UV radiation creates around them spheres of almost completely ionized HII that grow and eventually coalesce. These spheres have sharp edges that act to transform large-angle power from the primordial CMB into small-scale power. For some estimates of the impact due to patchy reionization of the angular CMB spectrum, see Ref. [262].

21.2 Molecular lines

The sources of diffuse galactic emission discussed so far all have a broad continuum emission spectrum. But there also exist molecular lines, mostly from rotational transitions of molecules, that emit in the microwave bands of interest here. The brightest of these are the CO lines [38], of which the lowest is situated at 115.3 GHz. Since CO is a linear molecule, there are also transitions at integer multiples of this frequency. Removing CO emission from the Planck data has proven to be a challenge [167]. For more sensitive future experiments, it is likely that other lines will also present concerns.

21.3 Zodiacal emission

Besides the planets and asteroids, our solar system is filled with large dust grains, known as zodiacal dust, which on the average are much larger than the interstellar dust grains described above. These grains manifest themselves by a variety of means. In the visible they scatter light from the sun, and this background must be subtracted when analyzing diffuse emission in the optical and near infrared bands. The zodiacal dust is concentrated around the ecliptic plane. It is a good but not perfect approximation to model the distribution of zodiacal dust assuming azimuthal symmetry. The temperature of the zodiacal dust is much above that of the interstellar dust and roughly proportional to the inverse square of the distance from the sun. Subtracting zodiacal emission is challenging because its contribution to a given point on the celestial sphere depends on the time of year when the observation is made, because observations at different times of the year look through different columns of dust, even when azimuthal symmetry is assumed. The ideal observing program for characterizing the zodiacal dust would cover the whole sky many times over the year in order to accumulate as many lines of sight to the same point on the celestial sphere as possible and to carry out a sort of tomography. For a discussion of zodiacal emission at long wavelengths as measured by Planck, see Ref. [168]. For previous work on zodiacal emission in the far infrared, see Ref. [65].

22 Extracting the Primordial CMB Anisotropies

Most of the contaminants described above, with the exception of gravitational lensing and the kinetic SZ effect, have a frequency dependence that differs from that of the primary CMB anisotropies. This property can be exploited to remove these nonprimordial contaminants and lies at the heart of all component separation techniques. If there are N distinct components, each of which is characterized by a fixed frequency spectrum, in the absence of measurement noise, a perfect separation of these components is possible using sky maps in N frequency bands. With more bands, the separation is overdetermined allowing validation of the model. The component separation strategy sketched above, which may be described as a linear method, is based on a linear model, but this is not the only way to clean maps. More sophisticated nonlinear models may be formulated, often based on or inspired by Bayesian

statistics that exploit other properties such as the positivity of certain components, spatial variation of spectral indices, and so on. Some methods are characterized as being “blind,” meaning that the number of components is indicated by data itself, while other methods are more physically based.

Because of limitations of space, we do not go into the details or practicalities of component separation, instead referring the reader to a few excellent reviews for more details. For an early discussion of the component separation problem and various approaches, see Refs. [24] and [44]. Reference [117] includes a comparison of methods used for the Planck analysis. Reference [56] describes foreground removal challenges for future CMB B mode polarization experiments and includes extensive references to the literature.

23 Concluding Remarks

Prior to the discovery of the CMB anisotropy in 1992 by the COBE team, cosmology was a field with a questionable reputation. Many from other fields described cosmology as a field where theorists were free to speculate with almost no observational or experimental constraints to contradict them. Much was made of the supposed distinction between an “observation” and an “experiment.”^w However, between 1992 and today cosmology has transformed into a precision science where it has become increasingly difficult to propose new models without contradicting present observation. Ironically, much science having only a tenuous connection to cosmology is now being explained to the public as serving to probe the big bang.

In this review, we have tried to sketch the most important aspects of the physics of the CMB in a self-contained way. Other reviews with a different emphasis include Refs. [92], [153] and [201]. We have seen how the CMB provides a snapshot of the state of the universe at around $z \approx 1100$, when the primordial perturbations were still very nearly linear, and how the precise angular pattern on the sky is also sensitive to a number of other cosmological parameters, which can be determined in many cases to the percent level or better. We have also explored tests of non-Gaussianity. At present no non-Gaussianity of a primordial origin has been observed, ruling out many nonminimal models of inflation, in particular multi-field models developed to explain hints of non-Gaussianity in the WMAP data, which subsequently were excluded by Planck.

We also saw how better measurements of the CMB absolute spectrum could reveal deviations from a perfect blackbody spectrum, some of which are to be expected and others of which would constitute signs of novel physics, such as energy injection at high-redshift. The absolute spectrum remains a promising frontier of CMB science.

The other promising area of CMB research is the characterization of the polarized sky, in particular to search for primordial B modes from inflation, which constitutes the most unique prediction of inflation. Maps of B modes on smaller angular scales would also allow characterization of the gravitational lensing field at much greater precision than is possible from observations of the temperature anisotropy. Such data would provide an important cross check of weak lensing surveys using the ellipticities of galaxies and provide a unique probe of absolute neutrino masses, perhaps allowing one to distinguish the normal from the inverted

^wIt is not clear whether proton-antiproton colliders would be classified as constituting an “experiment” under this criterion, because the experimenter has virtually no control over parameters of the hard parton-parton collisions of interest due to the broad spread in x of the parton distribution functions.

mass hierarchy.

Since this volume is dedicated to Albert Einstein and the hundredth anniversary of his celebrated paper presenting the general theory of relativity, we close with a few remarks about Einstein, and in particular about his relation to the subject of this chapter. Einstein is remembered by today's generation of physicists mostly for his role in the development of the special and general theories of relativity. This part of Einstein's work sometimes overshadows Einstein's numerous achievements in other areas and the extreme breadth of his scientific interests. Einstein is often viewed today as the paragon of the abstruse, highly mathematical theorist. Many physicists today would be surprised to learn that Einstein patented a design for an ammonia-butane refrigerator [59]. Others might be surprised to learn that Einstein is the author of one experimental paper for work after which the Einstein-de Haas effect is named. This effect may be thought of as the converse of the Barnett effect, which we saw in Sec. 19.5.1 plays a crucial role in the alignment of interstellar dust grains. Moreover, the stochastic differential equations in that section bear a close relation to Einstein's work on Brownian motion. General relativity was once regarded as an abstruse, highly mathematical subfield of physics. Within astrophysics, relativity was first introduced through the emergence of a subfield known as "relativistic astrophysics." But nowadays general relativity pervades almost all areas of astrophysics and has become one of the elements of the underlying fundamental physics that every astrophysicist must know. One can no longer neatly separate "relativistic astrophysics" from the rest of astrophysics.

This chapter told the story of the big bang cosmology from a point of view emphasizing the observations of the relic blackbody radiation. Einstein's theory of general relativity culminating in his celebrated 1915 formulation of the gravitational field equations^{x,y} enters as a key ingredient to this story in two ways. First there is unperturbed spacetime solution now known as the FLRW solutions. This family of spatially homogeneous and isotropic solutions to the Einstein equations was first found by Alexandre Friedmann in 1922 and independently by Georges Lemaître in 1927. At that time, the solutions were surprising because of their prediction of a non-eternal dynamical universe whose natural state was either expansion or contraction, an idea that was before its time. It was not until 1929 that Hubble discovered that the recessional velocities of distant galaxies except for some noise vary approximately linearly with distance (although in its first version the data was not statistically compelling). Einstein's general theory was deduced by drawing mainly on considerations of mathematical simplicity and elegance and on the equivalence principle, but remarkably applied to the expanding universe through the FLRW solution and its linearized perturbations, general relativity remains the basis of cosmology despite the great improvement in the data that has taken place between the 1920s and now. Today there is much talk about "modified gravity," largely motivated by the discovery of the so-called "dark energy," which no one yet really understands. It can be argued whether the dark energy belongs to the left hand side of the Einstein field equation, in which case it would constitute a revision to Einstein's theory, or on the right-hand side, in which case it would simply constitute a new form of exotic stress-

^xA. Einstein, "Die Feldgleichungen der Gravitation," *Sitzungsberichte der Königl. Preussische Akademie der Wissenschaften*, p. 844 (25 November, 1915).

^yFor an authoritative account from a scientific perspective of the path involving over a dozen papers and several reversals that finally led Einstein to the gravitational field equations as we know them today (i.e., $G_{\mu\nu} = R_{\mu\nu} - \frac{1}{2}g_{\mu\nu}R = (8\pi G_N)T_{\mu\nu}$), see Abraham Pais, *Subtle is the Lord* (New York, Oxford University Press, 1982).

energy, leaving the gravitational sector unchanged. But so far Einstein's theory of relativity as a classical field theory has survived without change. To be sure, we believe that gravitational theory as formulated by Einstein is an incomplete story. Where quantum effects become relevant, we know that there must be a more complete theory of which classical relativity is but a limiting case. But we do not yet know what that larger theory is. In the classical regime, Einstein's theory has survived many stringent tests, and perhaps more importantly has become an indispensable foundation for our current understanding of the universe and its origins.

Acknowledgments

MB would like to thank Ken Ganga, Kavilan Moodley, Heather Prince, Doris Rojas, and Andrea Tartari for many invaluable comments, corrections, and suggestions, and Jean-Luc Robert for making several of the figures. MB thanks the University of KwaZulu-Natal for its hospitality where a large part of this review was written.

References

- [1] K. N. Abazajian *et al.*, Neutrino physics from the cosmic microwave background and large scale structure, arXiv:astro-ph/1309.5383.
- [2] K. N. Abazajian *et al.*, Inflation physics from the cosmic microwave background and large scale structure, arXiv:astro-ph/1309.5381.
- [3] L. F. Abbott and M. B. Wise, Constraints on generalized inflationary cosmologies, *Nucl. Phys. B* **244** (1984) 541.
- [4] V. Acquaviva, N. Bartolo, S. Matarrese and A. Riotto, Gauge-invariant second-order perturbations and non-Gaussianity from inflation, *Nucl. Phys. B* **667** (2002) 119, arXiv:astro-ph/0209156.
- [5] A. Albrecht, D. Coulson, P. Ferreira and J. Magueijo, Causality, randomness, and the microwave background, *Phys. Rev. Lett.* **76** (1996) 1413.
- [6] Y. Ali-Haïmoud, C. M. Hirata and C. Dickinson, A refined model for spinning dust radiation, *Mon. Not. R. Astron. Soc.* **395** (2009) 1055.
- [7] R. A. Alpher, H. Bethe and G. Gamov, The origin of chemical elements, *Phys. Rev.* **73** (1948) 803.
- [8] K. Arnold *et al.*, The POLARBEAR CMB polarization experiment, *Proc. SPIE* **7741** (2010) 77411E.
- [9] D. Babich, P. Creminelli and M. Zaldarriaga, The shape of non-Gaussianities, *J. Cosmol. Astropart. Phys.* **08** (2004) 009, arXiv:astro-ph/0405356.
- [10] J. M. Bardeen, Gauge-invariant cosmological perturbations, *Phys. Rev. D* **22** (1980) 1882.
- [11] J. M. Bardeen, P. J. Steinhardt and M. S. Turner, Spontaneous creation of almost scale-free density perturbations in an inflationary universe, *Phys. Rev. D* **28** (1983) 679.
- [12] R. Barkana and A. Loeb, In the beginning: The first sources of light and the reionization of the universe, *Phys. Rep.* **349** (2001) 125, arXiv:astro-ph/0010468.
- [13] E. Battistellie *et al.*, QUBIC: The QU bolometric interferometer for cosmology, *Astropart. Phys.* **34** (2011) 705, arXiv:astro-ph/1010.0645.
- [14] R. H. Becker *et al.*, Evidence for reionization at $z \sim 6$: Detection of a Gunn-Peterson trough in a $z = 6.28$ quasar, *Astron. J.* **122** (2001) 2850, arXiv:astro-ph/0108097.
- [15] P. de Bernardis *et al.*, A flat universe from high-resolution maps of the cosmic microwave background radiation, *Nature* **404** (2000) 955, arXiv:astro-ph/0004404.
- [16] E. Bertschinger, COSMICS: Cosmological initial conditions and microwave anisotropy codes, arXiv:astro-ph/9506070.

- [17] BICEP2 Collab. (P. A. R. Ade *et al.*), Detection of B-mode polarization at degree angular scales by BICEP2, *Phys. Rev. Lett.* **112** (2014) 241101.
- [18] BICEP2 Collab. (P. A. R. Ade *et al.*), BICEP2. II. Experiment and three-year data set, *Astrophys. J.* **792** (2014) 62, arXiv:astro-ph/1403.4302.
- [19] M. Birkinshaw, The Sunyaev-Zel'dovich effect, *Phys. Rep.* **310** (1999) 97, arXiv:astro-ph/9808050.
- [20] R. Blandford and D. Eichler, Particle acceleration at astrophysical shocks: A theory of cosmic ray origin, *Phys. Rep.* **154** (1987) 1.
- [21] N. W. Boggess *et al.*, The COBE mission—Its design and performance two years after launch, *Astrophys. J.* **397** (1992) 420.
- [22] J. R. Bond and G. Efstathiou, Cosmic background radiation anisotropies in universes dominated by nonbaryonic dark matter, *Astrophys. J.* **285** (1984) L45.
- [23] M. Born and E. Wolf, *Principles of Optics* (Pergamon, New York, 1970).
- [24] F. R. Bouchet and R. Gispert, Foregrounds and CMB experiments: I. Semi-analytical estimates of contamination, *New Astron.* **4** (1999) 443, arXiv:astro-ph/9903176.
- [25] S. Boughn and R. Crittenden, A correlation between the cosmic microwave background and large-scale structure in the universe, *Nature* **427** (2004) 45, arXiv:astro-ph/0305001.
- [26] M. Bucher, A. S. Goldhaber and N. Turok, An open universe from inflation, *Phys. Rev. D* **52** (1995) 3314, arXiv:hep-ph/9411206.
- [27] M. Bucher and N. Turok, Open inflation with an arbitrary false vacuum mass, *Phys. Rev. D* **52** (1995) 5538.
- [28] M. Bucher, K. Moodley and N. Turok, General primordial cosmic perturbation, *Phys. Rev. D* **62** (2000) 083508, arXiv:astro-ph/9904231.
- [29] J. E. Carlstrom, G. P. Holder and E. D. Reese, Cosmology with the Sunyaev-Zel'dovich effect, *Ann. Rev. Astron. Astrophys.* **40** (2002) 643, arXiv:astro-ph/0208192.
- [30] J. Chluba and R. M. Thomas, Towards a complete treatment of the cosmological recombination problem, *Mon. Not. R. Astron. Soc.* **412** (2011) 748, arXiv:astro-ph/1010.3631.
- [31] J. Chluba and R. A. Sunyaev, Pre-recombinational energy release and narrow features in the CMB spectrum, *Astron. Astrophys.* **501** (2009) 29, arXiv:astro-ph/0803.3584.
- [32] C. R. Contaldi, J. Magueijo and L. Smolin, Anomalous CMB polarization and gravitational chirality, *Phys. Rev. Lett.* **101** (2008) 141101, arXiv: astro-ph/0806.3082.
- [33] COrE Collab. (F. Bouchet *et al.*), COrE (Cosmic Origins Explorer): A White Paper, arXiv:1102.2181.

- [34] B. P. Crill *et al.*, SPIDER: A balloon-borne large-scale CMB polarimeter, *Proc. SPIE 7010, Space Telescopes and Instrumentation 2008: Optical, Infrared, and Millimeter, 70102P* (July 12, 2008).
- [35] R. Crittenden, R. L. Davis and P. J. Steinhardt, Polarization of the microwave background due to primordial gravitational waves, *Astrophys. J.* **417** (1993) L13, arXiv:astro-ph/9306027.
- [36] R. G. Crittenden and N. Turok, Doppler peaks from cosmic texture, *Phys. Rev. Lett.* **75** (1995) 2642.
- [37] R. G. Crittenden and N. Turok, Looking for a cosmological constant with the Rees-Sciama effect, *Phys. Rev. Lett.* **76** (1996) 575, arXiv:astro-ph/9510072.
- [38] T. M. Dame *et al.*, The milky way in molecular clouds: A new complete CO survey, *Astrophys. J.* **547** (2001) 792.
- [39] S. Das *et al.*, Detection of the power spectrum of cosmic microwave background lensing by the atacama cosmology telescope, *Phys. Rev. Lett.* **107** (2011) 021301, arXiv:astro-ph/1103.2124.
- [40] L. Davis and J. Greenstein, The polarization of starlight by aligned dust grains, *Astrophys. J.* **114** (1951) 206.
- [41] P. Day *et al.*, A broadband superconducting detector suitable for use in large arrays, *Nature* **425** (2003) 817.
- [42] A. de Oliveira-Costa *et al.*, Galactic microwave emission at degree angular scales, *Astrophys. J.* **482** (1997) L17, arXiv:astro-ph/9702172.
- [43] P. De Bernardis, M. Bucher, C. Burigana and L. Piccirillo, B-Pol: Detecting primordial gravitational waves generated during inflation, *Exp. Astron.* **23** (2009) 5, arXiv:0808.1881.
- [44] J. Delabrouille, J.-F. Cardoso and G. Patanchon, Multi-detector multi-component spectral matching and applications for CMB data analysis, *Mon. Not. R. Astron. Soc.* **346** (2003) 1089, arXiv:astro-ph/0211504.
- [45] R. H. Dicke, The measurement of thermal radiation at microwave frequencies, *Rev. Sci. Instrum.* **17** (1946) 238.
- [46] R. H. Dicke, P. J. E. Peebles, P. G. Roll and D. T. Wilkinson, Cosmic black-body radiation, *Astrophys. J.* **142** (1965) 414.
- [47] S. Doyle, P. Mauskopf, J. Naylor, A. Porch and C. Duncombe, Lumped element kinetic inductance detectors, *J. Low Temp. Phys.* **151** (2008) 530.
- [48] B. T. Draine, Interstellar dust grains, *Ann. Rev. Astron. Astrophys.* **41** (2003) 241, arXiv:astro-ph/0304489.

- [49] B. T. Draine, Astrophysics of dust in cold clouds, in *The Cold Universe, Saas-Fee Advanced Course 32*, ed. D. Pfenniger (Springer-Verlag, Berlin, 2004), pp. 213–303, arXiv:astro-ph/0304488.
- [50] B. T. Draine and A. Lazarian, Electric dipole radiation from spinning dust grains, *Astrophys. J.* **508** (1998) 157, arXiv:astro-ph/9802239.
- [51] B. T. Draine and A. Lazarian, Diffuse galactic emission from spinning dust grains, *Astrophys. J.* **494** (1998) L19.
- [52] B. T. Draine and A. Lazarian, Magnetic dipole microwave emission from dust grains, *Astrophys. J.* **512** (1999) 740, arXiv:astro-ph/9807009.
- [53] B. T. Draine and J. C. Weingartner, Radiative torques on interstellar grains. I. Superthermal spin-up, *Astrophys. J.* **470** (1996) 551.
- [54] B. T. Draine, J. C. Weingartner and C. Joseph, Radiative torques on interstellar grains. II. Grain alignment, *Astrophys. J.* **480** (1997) 633.
- [55] W. W. Duley and D. A. Williams, The infrared spectrum of interstellar dust—Surface functional groups on carbon, *Mon. Not. R. Astron. Soc.* **196** (1981) 269.
- [56] J. Dunkley *et al.*, CMBPol mission concept study: Prospects for polarized foreground removal, *AIP Conf. Proc.* **1141** (2009) 222, arXiv:astro-ph/0811.3915.
- [57] J. Dunkley, M. Bucher, P. G. Ferreira and K. Moodley, C Skordis “Fast and reliable MCMC for cosmological parameter estimation, *Mon. Not. R. Astron. Soc.* **356** (2005) 925, arXiv:astro-ph/0405462.
- [58] J. Dunkley *et al.*, The Atacama cosmology telescope: Cosmological parameters from the 2008 power spectrum, *Astrophys. J.* **739** (2011) 52, arXiv:astro-ph/1009.0866.
- [59] A. Einstein and L. Szilárd, Refrigeration (Appl: 16 December 1927; Priority: Germany, 16 December 1926) U. S. Patent 1,781,541, 11 November 1930.
- [60] M. Eisenberg and R. Guy, A proof of the hairy ball theorem, *Am. Math. Mon.* **86** (1979) 571.
- [61] EPIC Collab. (J. Bock *et al.*), Study of the experimental probe of inflationary cosmology EPIC-Intermediate mission for NASA’s einstein inflation probe, arXiv:0906.1188.
- [62] R. Fabbri and M. Pollock, The effect of primordially produced gravitons upon the anisotropy of the cosmological microwave background radiation, *Phys. Lett. B* **125** (1983) 445.
- [63] A. Ferte and J. Grain, Detecting chiral gravity with the pure pseudospectrum reconstruction of the cosmic microwave background polarized anisotropies, arXiv:astro-ph/1404.6660.
- [64] D. J. Fixsen *et al.*, The spectrum of the extragalactic far-infrared background from the COBE FIRAS observations, *Astrophys. J.* **508** (1998) 123.

- [65] D. J. Fixsen and E. Dwek, The zodiacal emission spectrum as determined by COBE and its implications, *Astrophys. J.* **578** (2002) 1009.
- [66] D. J. Fixen *et al.*, The cosmic microwave background spectrum from the full COBE FIRAS data set, *Astrophys. J.* **473** (1996) 576.
- [67] R. Flauger, J. C. Hill and D. N. Spergel, Toward an understanding of foreground emission in the BICEP2 region, arXiv:astro-ph/1405.7351.
- [68] U. Fuskeland, I. K. Wehus, H. K. Eriksen and S. K. Naess, Spatial variations in the spectral index of polarized synchrotron emission in the 9 yr WMAP sky maps, *Astrophys. J.* **790** (2014) 104, arXiv:astro-ph/1404.5323.
- [69] M. Giard, G. Serra, E. Caux, F. Pajot and J. M. Lamarre, First detection of the aromatic 3.3-micron feature in the diffuse emission of the Galactic disk, *Astron. Astrophys.* **201** (1988) L1.
- [70] V. L. Ginzburg and S. I. Syrovatsk, Developments in the theory of synchrotron radiation and its reabsorption, *Ann. Rev. Astron. Astrophys.* **7** (1969) 375.
- [71] A. S. Goldhaber and M. Nieto, Terrestrial and extraterrestrial limits on the photon mass, *Rev. Mod. Phys.* **43** (1971) 277.
- [72] A. S. Goldhaber and M. Nieto, Photon and graviton mass limits, *Rev. Mod. Phys.* **82** (2010) 939, arXiv:hep-ph/0809.1003.
- [73] J. R. Gott III, Creation of open universes from de Sitter space, *Nature* **295** (1982) 304.
- [74] J. Richard Gott III and T. S. Statler, Constraints on the formation of bubble universes, *Phys. Lett. B* **136** (1984) 157.
- [75] J. E. Gunn and B. A. Peterson, On the density of neutral hydrogen in intergalactic space, *Astrophys. J.* **142** (1965) 1633.
- [76] A. H. Guth and S. Y. Pi, Fluctuations in the new inflationary universe, *Phys. Rev. Lett.* **49** (1982) 1110.
- [77] J. S. Hall, Observations of the polarized light from stars, *Science* **109** (1949) 166.
- [78] J. L. Han *et al.*, Pulsar rotation measures and the large-scale structure of the galactic magnetic field, *Astrophys. J.* **642** (2006) 868, arXiv:astro-ph/0601357.
- [79] S. Hanany *et al.*, MAXIMA-1: A measurement of the cosmic microwave background anisotropy on angular scales of 10° - 5° , *Astrophys. J.* **545** (2000) L5, arXiv:astro-ph/0005123.
- [80] N. Hand *et al.*, Evidence of galaxy cluster motions with the kinematic Sunyaev-Zel'dovich effect, *Phys. Rev. Lett.* **109** (2012) 041101, arXiv:astro-ph/1203.4219.
- [81] C. G. T. Haslam *et al.*, A 408 MHz all-sky continuum survey. I— Observations at southern declinations and for the north polar region, *Astron. Astrophys.* **100** (1981) 209.

- [82] M. G. Hauser *et al.*, The COBE diffuse infrared background experiment search for the cosmic infrared background. I. Limits and detections, *Astrophys. J.* **508** (1998) 25.
- [83] S. W. Hawking, The development of irregularities in a single bubble inflationary universe, *Phys. Lett. B* **115** (1982) 295.
- [84] M. Hazumi *et al.*, LiteBIRD: A small satellite for the study of B-mode polarization and inflation from cosmic background radiation detection, *Proc. SPIE 8442, Space Telescopes and Instrumentation 2012: Optical, Infrared, and Millimeter Wave, 844219* (August 22, 2012).
- [85] C. M. Hirata and E. R. Switzer, Primordial helium recombination. II. Two-photon processes, *Phys. Rev. D* **77** (2008) 083007, arXiv:astro-ph/0702144.
- [86] S. R. Hildebrandt, R. Rebolo, J. A. Rubiño-Martín, R. A. Watson, C. M. Gutiérrez, R. J. Hoyland and E. S. Battistelli, COSMOSOMAS observations of the cosmic microwave background and Galactic foregrounds at 11 GHz: Evidence for anomalous microwave emission at high Galactic latitude, *Mon. Not. R. Astron. Soc.* **382** (2007) 594, arXiv:0706.1873.
- [87] W. A. Hiltner, Polarization of light from distant stars by interstellar medium, *Science* **109** (1949) 165.
- [88] W. A. Hiltner, On the presence of polarization in the continuous radiation of stars. II., *Astrophys. J.* **109** (1949) 471.
- [89] W. Hu, D. Scott and J. Silk, Power spectrum constraints from spectral distortions in the cosmic microwave background, *Astrophys. J.* **430** (1994) L5, arXiv:astro-ph/9402045.
- [90] W. Hu and M. White, Acoustic signatures in the cosmic microwave background, *Astrophys. J.* **471** (1996) 30, arXiv:astro-ph/9602019.
- [91] W. Hu and T. Okamoto, Mass reconstruction with CMB polarization, *Astrophys. J.* **574** (2002) 566, arXiv:astro-ph/0111606.
- [92] W. Hu and S. Dodelson, Cosmic microwave background anisotropies, *Ann. Rev. Astron. Astrophys.* **40** (2002) 171, arXiv:astro-ph/0110414.
- [93] W. Hu and G. P. Holder, Model-independent reionization observables in the CMB, *Phys. Rev. D* **68** (2003) 023001, arXiv:astro-ph/0303400.
- [94] W. Hu and M. White, A CMB polarization primer, *New Astron.* **2** (1997) 323, arXiv:astro-ph/9706147.
- [95] A. F. Illarionov and R. A. SiuniaeV, Comptonization, the background-radiation spectrum, and the thermal history of the universe, *Sov. Astron.* **18** (1975) 691.
- [96] N. Jarosik *et al.*, First year Wilkinson microwave anisotropy probe (WMAP) observations: On-orbit radiometer characterization, *Astrophys. J.* **148** (2003) 29, arXiv:astro-ph/0302224.

- [97] G. Jungman, M. Kamionkowski, A. Kosowsky and D. N. Spergel, Cosmological parameter determination with microwave background maps, *Phys. Rev. D* **54** (1996) 1332, arXiv:astro-ph/9512139.
- [98] M. Kamionkowski and A. Kosowsky, The cosmic microwave background and particle physics, *Ann. Rev. Nucl. Part. Sci.* **49** (1999) 77, arXiv:astro-ph/9904108.
- [99] M. Kamionkowski, A. Kosowsky and A. Stebbins, Statistics of cosmic microwave background polarization, *Phys. Rev. D* **55** (1997) 7368, arXiv:astro-ph/9611125.
- [100] M. Kaplinghat, M. Chu, Z. Haiman, G. Holder, L. Knox and C. Skordis, Probing the reionization history of the universe using the cosmic microwave background polarization, *Astrophys. J.* **583** (2003) 24, arXiv:astro-ph/0207591.
- [101] J. Kaufman, B. Keating and B. Johnson, Precision tests of parity violation over cosmological distances, arXiv:astro-ph/1409.8242.
- [102] R. Keisler *et al.*, A measurement of the damping tail of the cosmic microwave background power spectrum with the south pole telescope, *Astrophys. J.* **743** (2011) 28, arXiv:astro-ph/1105.3182.
- [103] H. Kodama and M. Sasaki, Cosmological perturbation theory, *Prog. Theor. Phys. Suppl.* **78** (1984) 1.
- [104] A. Kogut *et al.*, Dipole anisotropy in the COBE DMR first-year sky maps, *Astrophys. J.* **419** (1993) 1, arXiv:astro-ph/9312056.
- [105] A. Kogut *et al.*, The primordial inflation explorer (PIXIE): A nulling polarimeter for cosmic microwave background observations, *J. Cosmol. Astropart. Phys.* **1107** (2011) 025, arXiv:astro-ph/1105.2044.
- [106] A. Kogut, A. J. Banday, C. L. Bennett, K. M. Gorski, G. Hinshaw and W. T. Reach, High-latitude galactic emission in the COBE differential microwave radiometer 2 year sky maps, *Astrophys. J.* **460** (1996) 1.
- [107] E. Komatsu and D. Spergel, Acoustic signatures of the primary microwave background bispectrum, arXiv:astro-ph/000503.
- [108] A. Kosowsky, Cosmic microwave background polarization, *Ann. Phys.* **246** (1996) 49, arXiv:astro-ph/9501045.
- [109] A. Kosowsky, The Atacama cosmology telescope, *New Astron. Rev.* **47** (2003) 939, arXiv:astro-ph/0402234.
- [110] J. Kovac *et al.*, Detection of polarization in the cosmic microwave background using DASI, *Nature* **420** (2002) 772, arXiv:astro-ph/0209478.
- [111] J. Kraus, *Radio Astronomy* (McGraw-Hill, New York, 1966).
- [112] L. Kuzmin, Ultimate cold-electron bolometer with strong electrothermal feedback, *Proc. SPIE Conf., Millimeter and Submillimeter Detectors for Astronomy II*, Vol. 5498 (2004), pp. 349.

- [113] J. M. Lamarre, Photon noise in photometric instruments at far infrared and submillimeter wavelengths, *Appl. Opt.* **25** (1986) 870.
- [114] K. Land and J. Magueijo, Examination of evidence for a preferred axis in the cosmic radiation anisotropy, *Phys. Rev. Lett.* **95** (2005) 071301, arXiv:astro-ph/0502237.
- [115] L. D. Landau and E. M. Lifshitz, *Electrodynamics of a Continuous Media: Course of Theoretical Physics*, Vol. 8 (First English edition) (Pergamon Press, New York, 1960).
- [116] A. Lazarian and B. Draine, Thermal flipping and thermal trapping: New elements in grain dynamics, *Ap. J.* **516** (1999) 37.
- [117] S. M. Leach *et al.*, Component separation methods for the Planck mission, *Astron. Astrophys.* **491** (2008) 597, arXiv:astro-ph/0805.0269.
- [118] A. T. Lee, P. L. Richards, S. W. Nam, B. Cabrera and K. D. Irwin, A superconducting bolometer with strong electrothermal feedback, *Appl. Phys. Lett.* **69** (1996) 1801.
- [119] A. Leger and J. L. Puget, Identification of the “unidentified” IR emission features of interstellar dust? *Astron. Astrophys.* **137** (1984) L5.
- [120] E. M. Leitch, A. C. S. Readhead, T. J. Pearson and S. T. Myers, An anomalous component of galactic emission, *Astrophys. J.* **486** (1997) L23, arXiv:astro-ph/9705241.
- [121] J. Lesgourgues and S. Pastor, Massive neutrinos and cosmology, *Phys. Rep.* **429** (2006) 307, arXiv:astro-ph/0603494.
- [122] A. Lewis, A. Challinor and A. Lasenby, Efficient computation of cosmic microwave background anisotropies in closed Friedmann-Robertson-Walker models, *Astrophys. J.* **538** (2000) 473.
- [123] A. Lewis and S. Bridle, Cosmological parameters from CMB and other data: A Monte-Carlo approach, *Phys. Rev. D* **66** (2002) 103511, arXiv:astro-ph/0205436.
- [124] A. Lewis and A. Challinor, Weak gravitational lensing of the CMB, *Phys. Rep.* **429** (2006) 1, arXiv:astro-ph/0601594.
- [125] A. R. Liddle and D. H. Lyth, *Cosmological Inflation and Large-Scale Structure* (Cambridge University Press, Cambridge, 2009).
- [126] E. M. Lifshitz and I. M. Khalatnikov, Investigations in relativistic cosmology, *Adv. Phys.* **12** (1963) 185.
- [127] R. Lupton, *Statistics in Theory and Practice* (Princeton University Press, Princeton, 1993).
- [128] D. Lyth, Large-scale energy-density perturbations and inflation, *Phys. Rev. D* **31** (1985) 1792.
- [129] D. H. Lyth and A. Riotto, Particle physics models of inflation and the cosmological density perturbation, *Phys. Rep.* **314** (1999) 1, arXiv:hep-ph/9807278.

- [130] C.-P. Ma and E. Bertschinger, Cosmological perturbation theory in the synchronous and conformal newtonian gauges, *Astrophys. J.* **455** (1995) 7, arXiv:astro-ph/9506072.
- [131] J. Maldacena, Non-Gaussian features of primordial fluctuations in single field inflationary models, *J. High Energy Phys.* **05** (2003) 013, arXiv:astro-ph/0210603.
- [132] L. Mandel and E. Wolf, *Optical Coherence and Quantum Optics* (Cambridge University Press, Cambridge, 1995).
- [133] T. A. Marriage *et al.*, The Atacama cosmology telescope: Sunyaev-Zel'dovich—Selected galaxy clusters at 148 GHz in the 2008 survey, *Astrophys. J.* **737** (2011) 61, arXiv:astro-ph/1010.1065.
- [134] J. C. Mather *et al.*, A preliminary measurement of the cosmic microwave background spectrum by the cosmic background explorer (COBE) satellite, *Astrophys. J.* **354** (1990) L37.
- [135] J. C. Mather *et al.*, Measurement of the cosmic microwave background spectrum by the COBE FIRAS instrument, *Astrophys. J.* **420** (1994) 439.
- [136] J. C. Mather, D. J. Fixsen and R. A. Shafer, Design for the COBE far-infrared absolute spectrophotometer, *Proc. SPIE* 2019, *Infrared Spaceborne Remote Sensing* (1993) 168.
- [137] C. Meny *et al.*, Far-infrared to millimeter astrophysical dust emission I: A model based on physical properties of amorphous solids, *Astron. Astrophys.* **468** (2007) 171, arXiv:astro-ph/0701226.
- [138] A. D. Miller *et al.*, A measurement of the angular power spectrum of the CMB from $\ell = 100$ to 400, *Astrophys. J.* **524** (1999) L1, arXiv:astro-ph/9906421.
- [139] V. F. Mukhanov, Gravitational instability of the universe filled with a scalar field, *JETP Lett.* **41** (1985) 493.
- [140] V. F. Mukhanov and G. V. Chibisov, Quantum fluctuation and nonsingular universe (in Russian), *JETP Lett.* **33** (1981) 532.
- [141] V. F. Mukhanov and G. V. Chibisov, The vacuum energy and large scale structure of the universe, *Sov. Phys. JETP* **56** (1982) 258.
- [142] V. F. Mukhanov, H. A. Feldman and R. H. Brandenberger, Theory of cosmological perturbations, *Phys. Rep.* **215** (1992) 203.
- [143] C. B. Netterfield *et al.*, A measurement by BOOMERANG of multiple peaks in the angular power spectrum of the cosmic microwave background, *Astrophys. J.* **571** (2002) 604, arXiv:astro-ph/0104460.
- [144] W.-T. Ni, Dilaton field and cosmic wave propagation, *Phys. Lett. A* **378** (2014) 3413, arXiv:1410.0126.
- [145] W.-T. Ni, Searches for the role of spin and polarization in gravity, *Rep. Prog. Phys.* **73** (2010) 056901, arXiv:0912.5057.

- [146] T. Okamoto and W. Hu, CMB lensing reconstruction on the full sky, *Phys. Rev. D* **67** (2003) 083002, arXiv:astro-ph/0301031.
- [147] D. Paradis *et al.*, Variations of the spectral index of dust emissivity from Hi-GAL observations of the galactic plane, *Astron. Astrophys.* **520** (2010) L8, arXiv:1009.2779.
- [148] J. R. Pardo, J. Cernicharo and E. Serabyn, Atmospheric transmission at microwaves (ATM): An improved model for millimeter/submillimeter applications, *IEEE Trans. Antennas Propagation* **49** (2001) 1683.
- [149] J. A. Peacock, *Cosmological Physics* (Cambridge University Press, Cambridge, 1998).
- [150] P.J.E. Peebles, Lyman A. Page, Jr. and R. B. Partridge (eds.), *Finding the Big Bang* (Cambridge University Press, Cambridge, England, 2009).
- [151] P.J.E. Peebles, *The Large-Scale Structure of the Universe* (Princeton University Press, Princeton, 1980).
- [152] P.J.E. Peebles, Recombination of the primeval plasma, *Astrophys. J.* **153** (1968) 1.
- [153] P.J.E. Peebles, Cosmic background temperature anisotropy in a minimal isocurvature model for galaxy formation, *Astrophys. J.* **315** (1987) L73.
- [154] P.J.E. Peebles and J. T. Yu, Primeval adiabatic perturbation in an expanding universe, *Astrophys. J.* **162** (1970) 815.
- [155] U.-L. Pen, U. Seljak and N. Turok, Power spectra in global defect theories of cosmic structure formation, *Phys. Rev. Lett.* **79** (1997) 1611.
- [156] U.-L. Pen, D. N. Spergel and N. Turok, Cosmic structure formation and microwave anisotropies from global field ordering, *Phys. Rev. D* **49** (1994) 692.
- [157] A. A. Penzias and R. W. Wilson, A measurement of excess antenna temperature at 4080 Mc/s, *Astrophys. J.* **142** (1965) 421.
- [158] S. Perlmutter *et al.*, Measurements of Ω and Λ from 42 High-Redshift Supernovae, *Astrophys. J.* **517** (1999) 565, arXiv:astro-ph/9812133.
- [159] Planck Collab. (P. A. R. Ade *et al.*), Planck early results XVIII: The power spectrum of cosmic infrared background anisotropies, *Astron. Astrophys.* **536** (2011) A18, arXiv:astro-ph/1101.2028.
- [160] Planck Collab. (P. A. R. Ade *et al.*), Planck early results. XX. New light on anomalous microwave emission from spinning dust grains, *Astron. Astrophys.* **536** (2011) A20, arXiv:1101.2031.
- [161] Planck Collab. (P. A. R. Ade *et al.*), Planck intermediate results. XV. A study of anomalous microwave emission in Galactic clouds, *Astron. Astrophys.* **565** (2014) A103, arXiv:1309.1357.

- [162] Planck Collab. (P. Ade *et al.*), Planck intermediate results. XIV. Dust emission at millimetre wavelengths in the Galactic plane, *Astron. Astrophys.* **564** (2014) A45, arXiv:1307.6815.
- [163] Planck Collab. (R. Adam *et al.*), Planck intermediate results. XXX. The angular power spectrum of polarized dust emission at intermediate and high galactic latitudes, arXiv:astro-ph/1409.5738.
- [164] Planck Collab. (P. Ade *et al.*), Planck 2013 results. XI. All-sky model of thermal dust emission, *Astron. Astrophys.* **571** (2014), arXiv:astro-ph/1312.1300.
- [165] Planck Collab. (P. Ade *et al.*), Planck 2013 results: I. Overview of products and results, *Astron. Astrophys.* **571** (2014) A1, arXiv:astro-ph/1303.5062.
- [166] Planck Collab. (P. Ade *et al.*), Planck 2013 results: XII. Diffuse component separation, *Astron. Astrophys.* **571** (2014) A12, arXiv:astro-ph/1303.5072.
- [167] Planck Collab. (P. Ade *et al.*), Planck 2013 results: XIII. Galactic CO emission, *Astron. Astrophys.* **571** (2014) A13, arXiv:astro-ph/1303.5073.
- [168] Planck Collab. (P. Ade *et al.*), Planck 2013 results: XIV. Zodiacal emission, *Astron. Astrophys.* **571** (2014) A14, arXiv:astro-ph/1303.5074.
- [169] Planck Collab. (P. Ade *et al.*), Planck 2013 results: XV. CMB power spectra and likelihood, *Astron. Astrophys.* **571** (2014) A15, arXiv:astro-ph/1303.5075.
- [170] Planck Collab. (P. Ade *et al.*), Planck 2013 results: XVI. Cosmological parameters, *Astron. Astrophys.* **571** (2014) A16, arXiv:astro-ph/1303.5076.
- [171] Planck Collab. (P. Ade *et al.*), Planck 2013 results: XVII. Gravitational lensing by large-scale structure, *Astron. Astrophys.* **571** (2014) A17, arXiv:astro-ph/1303.5077.
- [172] Planck Collab. (P. Ade *et al.*), Planck 2013 results: XIX. The integrated Sachs-Wolfe effect, *Astron. Astrophys.* **571** (2014) A19, arXiv:astro-ph/1303.5079.
- [173] Planck Collab. (P. Ade *et al.*), Planck 2013 results: XX. Cosmology from Sunyaev-Zeldovich cluster counts, *Astron. Astrophys.* **571** (2014) A20, arXiv:astro-ph/1303.5080.
- [174] Planck Collab. (P. Ade *et al.*), Planck 2013 results: XXI. All-sky Compton-parameter map and characterization, *Astron. Astrophys.* **571** (2014) A21, arXiv:astro-ph/1303.5081.
- [175] Planck Collab. (P. Ade *et al.*), Planck 2013 results: XXII. Constraints on inflation, *Astron. Astrophys.* **571** (2014) A22, arXiv:astro-ph/1303.5082.
- [176] Planck Collab. (P. Ade *et al.*), Planck 2013 results: XXIII. Isotropy and statistics of the CMB, *Astron. Astrophys.* **571** (2014) A23, arXiv:astro-ph/1303.5083.
- [177] Planck Collab. (P. Ade *et al.*), Planck 2013 results: XXIV. Constraints on primordial non-Gaussianity, *Astron. Astrophys.* **571** (2014) A24, arXiv:astro-ph/1303.5084.

- [178] Planck Collab. (P. Ade *et al.*), Planck 2013 results: XXV. Searches for cosmic strings and other topological defects, *Astron. Astrophys.* **571** (2014) A25, arXiv:astro-ph/1303.5085.
- [179] Planck Collab. (P. Ade *et al.*), Planck 2013 results: XXVI. Background geometry and topology of the Universe, *Astron. Astrophys.* **571** (2014) A26, arXiv:astro-ph/1303.5086.
- [180] Planck Collab. (P. Ade *et al.*), Planck 2013 results: XXVII. Doppler boosting of the CMB: Eppur si muove, *Astron. Astrophys.* **571** (2014) A27, arXiv:astro-ph/1303.5087.
- [181] Planck Collab. (P. Ade *et al.*), Planck 2013 results: XXIX. The Planck catalogue of Sunyaev-Zeldovich sources, *Astron. Astrophys.* **571** (2014) A29, arXiv:astro-ph/1303.5089.
- [182] Planck Collab. (P. Ade *et al.*), Planck 2013 results. XXVIII. The Planck catalogue of compact sources, *Astron. Astrophys.* **571** (2014) A28, arXiv:astro-ph/1303.5088.
- [183] Planck Collab. (N. Aghanim *et al.*), Planck 2013 results. II. Low frequency instrument data processing, *Astron. Astrophys.* **571** (2014) A2, arXiv:1303.5063.
- [184] Planck Collab. (P. A. Ade *et al.*), Planck 2013 results. VI. High frequency instrument data processing, *Astron. Astrophys.* **571** (2014) A6, arXiv:1303.5067.
- [185] Planck Collab. (P. A. Ade *et al.*), Planck 2013 results. X. HFI energetic particle effects, *Astron. Astrophys.* **571** (2014) A10, arXiv:1303.5071.
- [186] Polarbear Collab. (P. A. R. Ade *et al.*), A measurement of the cosmic microwave background B-mode polarization power spectrum at sub-degree scales with POLARBEAR, *Astrophys. J.* **794** (2014) 171, arXiv:1403.2369.
- [187] M. Pospieszalski and E. J. Wollack, Ultralow noise InP field effect transistor radio astronomy receivers: State of the art, *13 Int. Conf. Microwaves, Radar and Wireless Communications*, MIKON-2000.
- [188] J. Preskill, Vortices and monopoles, *Architecture of Fundamental Interactions at Short Distances*, ed. P. Ramond (North-Holland, Amsterdam, 1987).
- [189] PRISM (Polarized Radiation Imaging and Spectroscopy Mission): An Extended White Paper PRISM Collab. (P. André *et al.*, *J. Cosmol. Astropart. Phys.* **02** (2014) 006, arXiv:1310.1554.
- [190] J. L. Puget and A. Leger, A new component of the interstellar matter: Small grains and large aromatic molecules, *Ann. Rev. Astron. Astrophys.* **27** (1989) 161.
- [191] J.-L. Puget *et al.*, Tentative detection of a cosmic far infrared background with COBE, *Astron. Astrophys.* **308** (1996) L5.
- [192] E. M. Purcell, On the absorption and emission of light by interstellar grains, *Astrophys. J.* **158** (1969) 433.
- [193] E. M. Purcell, Suprathermal rotation of interstellar grains, *Astrophys. J.* **231** (1979) 404.

- [194] C. L. Reichardt *et al.*, A measurement of secondary cosmic microwave background anisotropies with two years of South Pole Telescope Observations, *Astrophys. J.* **755** (2012) 70, arXiv:astro-ph/1111.0932.
- [195] Y. Rephaeli, Comptonization of the cosmic microwave background: The Sunyaev-Zeldovich effect, *Ann. Rev. Astron. Astrophys.* **33** (1995) 541.
- [196] A. G. Riess *et al.*, Observational evidence from supernovae for an accelerating universe and a cosmological constant, *Astron. J.* **116** (1998) 1009, arXiv:astro-ph/9805201.
- [197] V. Rubakov, M. Sazhin and A. Veryaskin, Graviton creation in the inflationary universe and the grand unification scale, *Phys. Lett. B* **115** (1982) 189.
- [198] J. A. Rubiño-Martín, C. H. López-Caraballo, R. Génova-Santos and R. Rebolo, Observations of the polarization of the anomalous microwave emission: A review, *Advances in Astronomy*, 2012, 351836 (2012).
- [199] J. Ruhl *et al.*, The south pole telescope, *Proc. SPIE* **5498** (2004) 11, arXiv:astro-ph/0411122.
- [200] R. K. Sachs and A. M. Wolfe, Perturbations of a cosmological model and angular variations of the microwave background, *Astrophys. J.* **147** (1967) 73.
- [201] D. Samtleben, S. Staggs and B. Winstein, The cosmic microwave background for pedestrians: A review for particle and nuclear physicists, *Ann. Rev. Nucl. Part. Sci.* **57** (2007) 245, arXiv:0803.0834 [astro-ph].
- [202] S. Seager, D. Sasselov and D. Scott, A new calculation of the recombination epoch, *Astrophys. J.* **523** (1999) L1, arXiv:astro-ph/9909275.
- [203] S. Seager, D. Sasselov and D. Scott, How exactly did the universe become neutral? *Astrophys. J. Suppl.* **128** (2000) 407, arXiv:astro-ph/9912182.
- [204] K. Sellgren, The near-infrared continuum emission of visual reflection nebulae, *Astrophys. J.* **277** (1984) 623.
- [205] U. Seljak, A two-fluid approximation for calculating the cosmic microwave background anisotropies, *Astrophys. J.* **435** (1994) L87.
- [206] U. Seljak and M. Zaldarriaga, A line-of-sight integration approach to cosmic microwave background anisotropies, *Astrophys. J.* **469** (1996) 437, arXiv:astro-ph/9603033.
- [207] J. Silk, Cosmic black-body radiation and galaxy formation, *Astrophys. J.* **151** (1968) 459.
- [208] J. Silk and J. Chluba, Next steps for cosmology, *Science* **344** (2014) 586.
- [209] K. M. Smith, O. Zahn and O. Doré, Detection of gravitational lensing in the cosmic microwave background, *Phys. Rev. D* **76** (2007) 043510, arXiv:astro-ph/0705.3980.
- [210] G. Smoot *et al.*, COBE differential microwave radiometers: Instrument design and implementation, *Astrophys. J.* **360** (1990) 685S.

- [211] G. F. Smoot *et al.*, Structure in the COBE differential microwave radiometer first-year maps, *Astrophys. J.* **396** (1992) L1.
- [212] L. Sorbo, Parity violation in the cosmic microwave background from a pseudoscalar inflaton, *J. Cosmol. Astropart. Phys.* **1106** (2011) 003, arXiv:astro-ph/1101.1525.
- [213] L. Spitzer Jr. and T. A. McGlynn, Disorientation of interstellar grains in suprathermal rotation, *Ap. J.* **231** (1979) 417.
- [214] L. Spitzer, Jr. and J. W. Tukey, A theory of interstellar polarization, *Astrophys. J.* **114** (1951) 187S.
- [215] R. A. Sunyaev and Y. B. Zeldovich, Small-scale fluctuations of relic radiation, *Astrophys. Space Sci.* **7** (1970) 3.
- [216] A. Starobinsky, Spectrum of relict gravitational radiation and the early state of the universe, *JETP. Lett.* **30** (1979) 682.
- [217] A. Starobinsky, Cosmic background anisotropy induced by isotropic flat-spectrum gravitational wave perturbations, *Sov. Astron. Lett.* **11** (1985) 133.
- [218] A. A. Starobinsky, Dynamics of phase transition in the new inflationary universe scenario and generation of perturbations, *Phys. Lett. B* **117** (1982) 175.
- [219] A. Stuart and K. Ord, *Kendall's Advanced Theory of Statistics, Classical Inference and Relationship*, Vol. 2 (Oxford University Press, New York, 1991).
- [220] E. R. Switzer and C. M. Hirata, Primordial helium recombination. I. Feedback, line transfer, and continuum opacity, *Phys. Rev. D* **77** (2008) 083006, arXiv:astro-ph/0702143.
- [221] A. Taylor, K. Grainge, M. Jones, G. Pooley, R. Saunders and E. Waldram, The radio source counts at 15 GHz and their implications for cm-wave CMB imaging, *Mon. Not. R. Astron. Soc.* **327** (2001) L1, arXiv:astro-ph/0102497.
- [222] N. Turok (ed.), *Critical Dialogues in Cosmology* (World Scientific Publishing, Singapore, 1997).
- [223] A. van Engelen *et al.*, A measurement of gravitational lensing of the microwave background using south pole telescope data, *Astrophys. J.* **756** (2012) 142, arXiv:1202.0546.
- [224] P. Vielva, E. Martínez-González, M. Cruz, R. B. Barreiro and M. Tucci, Cosmic microwave background polarization as a probe of the anomalous nature of the cold spot, *Mon. Not. R. Astron. Soc.* **410** (2011) 33.
- [225] P. Vielva, E. Martínez-González, R. B. Barreiro, J. L. Sanz and L. Cayón, Detection of non-Gaussianity in the Wilkinson microwave anisotropy probe first-year data using spherical wavelets, *Astrophys. J.* **609** (2004) 22.
- [226] A. Vilenkin and E. P. S. Shellard, *Cosmic Strings and Other Topological Defects* (Cambridge University Press, Cambridge, 1994).

- [227] Wald, *General Relativity* (University of Chicago Press, Chicago, 1984).
- [228] T. P. Walker, G. Steigman, H.-S. Kang, D. M. Schramm and K. A. Olive, Primordial nucleosynthesis redux, *Astrophys. J.* **376** (1991) 51.
- [229] R. A. Watson *et al.*, Detection of anomalous microwave emission in the perseus molecular cloud with the COSMOSOMAS experiment, *Astrophys. J.* **624** (2005) L89, arXiv:astro-ph/0503714.
- [230] S. Weinberg, *Gravitation and Cosmology: Principles and Applications of the General Theory of Relativity* (J. Wiley & Sons, New York, 1972).
- [231] J. C. Weingartner and B. T. Draine, Radiative torques on interstellar grains. III. dynamics with thermal relaxation, *Astrophys. J.* **589** (2003) 289.
- [232] R. Williamson *et al.*, A Sunyaev-Zel'dovich-selected sample of the most massive galaxy clusters in the 2500 deg² south pole telescope survey, *Astrophys. J.* **738** (2011) 139, arXiv:astro-ph/1101.1290.
- [233] M. White and W. Hu, The Sachs-Wolfe effects, *Astron. Astrophys.* **321** (1997) 8, arXiv:astro-ph/9609105.
- [234] E. T. Whittaker, *A Treatise on the Analytical Dynamics of Particles and Rigid Bodies* (Cambridge University Press, Cambridge, 1917).
- [235] WMAP Collab. (C. L. Bennett *et al.*), First year Wilkinson microwave anisotropy probe (WMAP) observations: Preliminary maps and basic results, *Astrophys. J. Suppl.* **148** (2003) 1.
- [236] WMAP Collab. (G. Hinshaw *et al.*), First year Wilkinson microwave anisotropy probe (WMAP) observations: Data processing methods and systematic error limits, *Astrophys. J. Suppl.* **148** (2003) 63.
- [237] WMAP Collab. (D. N. Spergel *et al.*), First year Wilkinson microwave anisotropy probe (WMAP) observations: Determination of cosmological parameters, *Astrophys. J. Suppl.* **148** (2003) 175.
- [238] WMAP Collab. (C. L. Bennett *et al.*), First year Wilkinson microwave anisotropy probe (WMAP) observations: Foreground emission, *Astrophys. J. Suppl.* **148** (2003) 97.
- [239] WMAP Collab. (H. V. Peiris *et al.*), First year Wilkinson microwave anisotropy probe (WMAP) observations: Implications for inflation, *Astrophys. J. Suppl.* **148** (2003) 213.
- [240] WMAP Collab. (L. Page *et al.*), First year Wilkinson microwave anisotropy probe (WMAP) observations: Interpretation of the TT and TE angular power spectrum peaks, *Astrophys. J. Suppl.* **148** (2003) 233.
- [241] WMAP Collab. (A. Kogut *et al.*), First year Wilkinson microwave anisotropy probe (WMAP) observations: Temperature-polarization correlation, *Astrophys. J. Suppl.* **148** (2003) 161.

- [242] WMAP Collab. (E. Komatsu *et al.*), First year Wilkinson microwave anisotropy probe (WMAP) observations: Tests of Gaussianity, *Astrophys. J. Suppl.* **148** (2003) 119.
- [243] WMAP Collab. (G. Hinshaw *et al.*), First year Wilkinson microwave anisotropy probe (WMAP) observations: The angular power spectrum, *Astrophys. J. Suppl.* **148** (2003) 135.
- [244] WMAP Collab. (A. Kogut *et al.*), Three-year Wilkinson microwave anisotropy probe (WMAP) observations: Foreground polarization, *Astrophys. J. Suppl.* **665** (2007) 355.
- [245] WMAP Collab. (G. Hinshaw *et al.*), Three-year Wilkinson microwave anisotropy probe (WMAP) observations: Temperature analysis, *Astrophys. J. Suppl.* **170** (2007) 288.
- [246] WMAP Collab. (L. Page *et al.*), Three-year Wilkinson microwave anisotropy probe (WMAP) observations: Polarization analysis, *Astrophys. J. Suppl.* **170** (2007) 335.
- [247] WMAP Collab. (D. N. Spergel *et al.*), Three-year Wilkinson microwave anisotropy probe (WMAP) observations: Implications for cosmology, *Astrophys. J. Suppl.* **170** (2007) 377.
- [248] WMAP Collab. (J. Dunkley *et al.*), Five-year Wilkinson microwave anisotropy probe (WMAP) observations: Bayesian estimation of CMB polarization maps, *Astrophys. J. Suppl.* **701** (2009) 1804.
- [249] WMAP Collab. (G. Hinshaw *et al.*), Five-year Wilkinson microwave anisotropy probe (WMAP) observations: Data processing, sky maps, and basic results, *Astrophys. J. Suppl.* **180** (2009) 225.
- [250] WMAP Collab. (B. Gold *et al.*), Five-year Wilkinson microwave anisotropy probe (WMAP) observations: Galactic foreground emission, *Astrophys. J. Suppl.* **180** (2009) 265.
- [251] WMAP Collab. (M. Nolta *et al.*), Five-year Wilkinson microwave anisotropy probe (WMAP) observations: Angular power spectra, *Astrophys. J. Suppl.* **180** (2009) 296.
- [252] WMAP Collab. (J. Dunkley *et al.*), Five-year Wilkinson microwave anisotropy probe (WMAP) observations: Likelihoods and parameters from WMAP Data, *Astrophys. J. Suppl.* **180** (2009) 306.
- [253] WMAP Collab. (E. Komatsu *et al.*), Five-year Wilkinson microwave anisotropy probe (WMAP) observations: Cosmological interpretation, *Astrophys. J. Suppl.* **180** (2009) 330.
- [254] WMAP Collab. (N. Jarosik *et al.*), Seven-year Wilkinson microwave anisotropy probe (WMAP) observations: Sky maps, systematic errors, and basic results, *Astrophys. J. Suppl.* **192** (2011) 14J.
- [255] WMAP Collab. (B. Gold *et al.*), Seven-year Wilkinson microwave anisotropy probe (WMAP) observations: Galactic foreground emission, *Astrophys. J. Suppl.* **192** (2011) 15G.

- [256] WMAP Collab. (D. Larson *et al.*), Seven-year Wilkinson microwave anisotropy probe (WMAP) observations: Power spectra and WMAP-derived parameters, *Astrophys. J. Suppl.* **192** (2011) 16L.
- [257] WMAP Collab. (C. Bennett *et al.*), Seven-year Wilkinson microwave anisotropy probe (WMAP) observations: Are there cosmic microwave background anomalies? *Astrophys. J. Suppl.* **192** (2011) 17.
- [258] WMAP Collab. (E. Komatsu *et al.*), Seven-year Wilkinson microwave anisotropy probe (WMAP) observations: Cosmological interpretation, *Astrophys. J. Suppl.* **192** (2011) 18K.
- [259] WMAP Collab. (C. L. Bennett *et al.*), Nine-year Wilkinson microwave anisotropy probe (WMAP) observations: Final maps and results, *Astrophys. J. Suppl.* **208** (2013) 20B.
- [260] WMAP Collab. (G. F. Hinshaw *et al.*), Nine-year Wilkinson microwave anisotropy probe (WMAP) observations: Cosmology results, *Astrophys. J. Suppl.* **208** (2013) 19H.
- [261] K. Yamamoto, M. Sasaki and T. Tanaka, Large angle CMB anisotropy in an open universe in the one-bubble inflationary scenario, *Astrophys. J.* **455** (1995) 412, arXiv:astro-ph/9501109.
- [262] O. Zahn, M. Zaldarriaga, L. Hernquist and M. McQuinn, The influence of nonuniform reionization on the CMB, *Astrophys. J.* **630** (2005) 657, arXiv:astro-ph/0503166.
- [263] M. Zaldarriaga and U. Seljak, All-sky analysis of polarization in the microwave background, *Phys. Rev. D* **55** (1997) 1830, arXiv:astro-ph/9609170.